Dissertation

submitted to the

Combined Faculty of Mathematics, Engineering and Natural Sciences

of Heidelberg University, Germany

for the degree of

Doctor of Natural Sciences

Put forward by

Glen Houston Hunter

born in: Edinburgh, United Kingdom

Oral examination: 24-07-2024

The consequence of dynamics in the interstellar medium

Referees: apl. Prof. Dr. Simon C. O. Glover

Prof. Friedrich K. Röpke

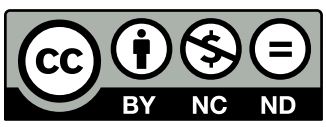

Abstract

The interstellar medium (ISM) of the Milky Way is in a constant state of motion. Between the large scale motions of galactic dynamics and the turbulence within giant molecular clouds (GMCs), the evolution of the ISM is guided by its underlying motions. The large scale dynamics perturb the diffuse warm neutral medium (WNM) of the Milky Way, starting the cascade of the formation of clouds and stars. In this thesis we make use of hydrodynamical simulations to explore the impact dynamics has on various quantities. The first part of this thesis focuses on the collisions of giant molecular clouds, exploring how star formation rates change with collisions. We verify the stabilitiy of "clumps" within our simulations and relating these properties to the alignment of the magnetic and velocity fields within our simulations. The second part of this thesis zooms out, looking at the structure of the Milky Way itself. We present a new, realistic model for the gravitational potential of the Milky Way and test out how reliable the axisymmetric assumption is when used in kinematic distance estimates.

Zusammenfassung

Das interstellare Medium (ISM) der Milchstraße befindet sich in einem ständigen Bewegungszustand. Von den großräumigen Bewegungen der galaktischen Dynamik bishin zu den Turbulenzen in den Riesenmolekülwolken (GMCs), wird die Entwicklung des ISM durch die zugrunde liegenden Bewegungen gesteuert. Die großräumige Dynamik stört das diffuse warme neutrale Medium (WNM) der Milchstraße und setzt die Kaskade der Wolken- und Sternbildung in Gang. In dieser Arbeit nutzen wir hydrodynamische Simulationen, um die Auswirkungen der Dynamik auf verschiedene Größen zu untersuchen. Der erste Teil dieser Arbeit konzentriert sich auf die Kollisionen von Riesenmolekülwolken und untersucht, wie sich die Sternentstehungsraten bei Kollisionen ändern. Wir überprüfen die Stabilität von "Klumpen" in unseren Simulationen und setzen diese Eigenschaften mit der Ausrichtung der Magnet- und Geschwindigkeitsfelder in unseren Simulationen in Beziehung. Der zweite Teil dieser Arbeit zoomt heraus und betrachtet die Struktur der Milchstraße selbst. Wir stellen ein neues, realistisches Modell für das Gravitationspotential der Milchstraße vor und testen, wie zuverlässig die Annahme von Achsensymmetrie ist, wenn sie für kinematische Entfernungsschätzungen verwendet wird.

Contents

Abstract vii

Zusammenfassung ix

Contents xi

List of Figures xv

List of Tables xxi

List of Acronyms xxiii

List of Publications xxv

1 Introduction 1

1.1 Interstellar Medium . . . 2

1.1.1 Phases of the ISM . . . 2

1.1.2 Molecular clouds . . . 4

1.1.3 Star formation . . . 8

1.2 Galactic dynamics . . . 9

1.2.1 Gravitational force . . . 9

1.2.2 Velocity curves . . . 10

1.2.3 Potential models . . . 13

1.3 About this thesis . . . 20

2 Numerical methodology 21

2.1 Arepo, moving-mesh hydrodynamics . . . 21

2.1.1 Overview of hydrodynamics . . . 21

2.1.2 Details of Arepo . . . 25

2.2 Agama, gravitational dynamics library . . . 27

2.2.1 Treatment of gravity in simulations . . . 27

2.2.2 Constructing potentials with Agama . . . 29
2.2.3 Interfacing Agama into Arepo . . . 32

3 Star formation induced by cloud-cloud collisions 35
3.1 Introduction . . . 36
3.2 Methodology . . . 39
3.2.1 Numerical magnetohydrodynamics . . . 39
3.2.2 Chemical network . . . 40
3.2.3 Star formation . . . 40
3.2.4 Initial conditions . . . 42
3.3 Results . . . 44
3.3.1 Star formation rate . . . 44
3.3.2 Impact on the virial parameter . . . 50
3.3.3 Flow alignment to magnetic field . . . 57
3.4 Discussion . . . 61
3.4.1 Comparison with W17 . . . 61
3.4.2 Do cloud collisions trigger star formation? . . . 66
3.5 Conclusions . . . 67

4 Reliability of kinematic distances 69
4.1 Introduction . . . 70
4.2 Galactic potential . . . 72
4.2.1 Components of the potential . . . 72
4.2.2 Comparison with observations . . . 79
4.3 Numerical simulations . . . 82
4.3.1 Numerical hydrodynamics . . . 83
4.3.2 External Galactic potential . . . 84
4.3.3 Initial conditions . . . 85
4.4 Results . . . 86
4.4.1 The gas response . . . 86
4.4.2 Kinematic distance estimates . . . 89
4.4.3 Location of kinematic distance errors . . . 95
4.4.4 Relation to the velocity deviation . . . 98
4.5 Discussion . . . 100
4.5.1 Implications . . . 100
4.5.2 Caveats . . . 104
4.6 Conclusions . . . 106

5 Conclusion and future plans **109**

A Additional information for Chapter 3 **113**

A.1 Chemical network 113

A.2 Post-collision magnetic field 120

B Additional information for Chapter 4 **123**

B.1 Spiral arm strength 123

B.2 Parameter study 123

Bibliography **129**

Acknowledgements **147**

List of Figures

1.1 Circular-velocity curve of the Milky Way from different tracers. In grey is the rotation curve from Sofue et al. (2009), obtained from H I (Burton & Gordon, 1978; Fich et al., 1989) and CO (Clemens, 1985) tangential velocities, CO and H II regions (Blitz et al., 1982; Fich et al., 1989) and carbon star kinematics (Demers & Battinelli, 2007). In red and blue are the circular velocities obtained from maser parallaxes (Reid et al., 2014) and parallaxes of Classical Cepheids with *Gaia* (Mróz et al., 2019) respectively. (Adapted from Mróz et al., 2019, .) 11

1.2 The density profile of the dark matter halo discussed in section 1.2.3. In black are the halo potentials discussed by the double power law profile (Eqn. 1.24) with ρ_0 and a being the normalising density and scale radius respectively. The blue lines represent the Einasto profile (Eqn. 1.26) with $\rho_0 = \rho_{-2}$ and $a = r_{-2}$ being the density and radius where the slope of the profile is equal to -2. 15

2.1 Projection of hydrodynamic blast wave using the AMR code `Athena++`. Left hand panel shows the blast wave with a uniform grid, middle panel shows it with AMR and the right hand panel shows the levels of refinement. (Figure credit: Stone et al., 2020) 23

2.2 An example of a particle distribution around a central SPH particle i. All black particles within the kernel radius kh contribute to the fluid quantities of particle i. All white particles fall out of the kernel and do not contribute. The shape of the kernel W is shown on the $x - y$ axis. (Figure credit: Liang et al., 2019) 25

2.3 The generation of a Voronoi tesselation from a Delaunay triangulation with the circumcircles and circumcentres as the red circles and points respectively. The left plot depicts an example Delaunay triangulation with the vertices (mesh-generating points) in blue. The middle and right plots show the resulting Voronoi tesselation from the Delaunay triangulation (red dashed lines in middle plot). 26

2.4 An illustration indicating the grid that is formed with the multipole expansion (red dots) and cyldrical Fourier expansion (blue crosses) in the R, z-place. Both grids have 8 grid points in the radial direction, 5 angular point within the multipole expansion (equivalent to $l_{\max} = 8$), and 8 grid points in the z direction for the Fourier expansion. (Figure credit: Vasiliev, 2019). 32

3.1 Surface density plot of the initial positions of the clouds. 43

3.2 Column density plots of all simulations at $t = 2.40$ Myr. The green dots within the plot represent the sink particles that have formed. 45

3.3 *Top*: Evolution of the mass in sink particles as a function of time in all nine simulations. *Bottom*: Star formation rate as a function of time in all nine simulations. 46

3.4 Fraction of gas above the specified density threshold in all nine simulations, plotted as a function of time. The thresholds are indicated in the top-left corner of each panel and are $n > 10^3$ cm^{-3}, 10^4 cm^{-3}, 10^5 cm^{-3} and 10^6 cm^{-3} from *top* to *bottom*. We see that increasing the collisional velocity increases the amount of gas above the threshold for all values of the threshold, but that the effect is much stronger for the higher density thresholds. 49

3.5 Fraction of dense ($n > 10^4$ cm^{-3}) gas in all nine simulations, plotted as a function of the separation between the clouds' centre of masses 50

3.6 *Top*: Star formation rate varying with time from initial sink formation for all simulations. *Bottom*: Star formation rate normalised to $v_{\rm rel} = 0$ km s^{-1} star formation rate as a function of time from initial sink formation. 51

3.7 From the top down: The average a) thermal to gravitational energy ratio, b) magnetic to gravitational energy ratio, c) kinetic to gravitational energy ratio, and d) virial parameter for different collisional velocities $v_{\rm rel}$ at 1 Myr after first sink formation. The error bars indicate the full range of values obtained. Each density bin is indicated with the corresponding bracket annotation with the separation of the points for ease of reading. The points within a bracket are for the same density bin but are offset in the figure for clarity. 54

3.8 Same as Figure 3.7 but looking at the differences in the inclination of magnetic field 56

3.9 Weighted histogram of the velocity and magnetic field alignment for differing collisional velocities at 1 Myr after first sink formation. Each subplot represents a different density bin. The black dashed line represents the distribution we would expect if the alignment is random. . . . 58

3.10 Same as Figure 3.9 but for varying magnetic field inclination. 59

3.11 Cumulative distribution of the initial alignment of the simulations at $t = 0$ Myr. *Top*: Varying collisional velocity. *Bottom*: Varying magnetic field inclination. The dashed black lines represent where the cumulative distribution would encompass 50% of the data assuming a Gaussian distribution of alignments. Points in the top-left and bottom-right quadrants are indicative of a skewed distribution. 60

3.12 Temperature distribution of all gas cells of $n \geq 10^5 \mathrm{cm}^{-3}$ for different collisional velocities at 1 Myr after initial sink particle creation. 65

3.13 Volume-weighted temperature-density phase diagram for $v_{\rm rel} = 0 \mathrm{km\,s}^{-1}$ (left panel) and $v_{\rm rel} = 15\ \mathrm{km\,s}^{-1}$ (right panel), shown for the snapshot immediately prior to the formation of the first sink particle. The dashed vertical line is the initial density of the clouds and the dotted vertical line is the density above which we consider the gas to be dense. The impact of $v_{\rm rel}$ on the temperature distribution is small, owing to the short cooling time of the gas. 65

4.1 Circular-velocity curve produced by our model (black line). The contribution of each component of the potential represented by the coloured lines as detailed in the legend. Observation points from Eilers et al. (2019) and Mróz et al. (2019) are also included (colored markers). Left, middle and right panels feature the profile for a radius between 0 and 1 kpc, 0 and 8 kpc and 0 and 20 kpc respectively. All axis scales are linear. 73

4.2 Density distribution of the underlying gravitational potential within the midplane ($z = 0$ kpc) of the galaxy. 73

4.3 The strength of the spiral arms at solar circle, $R = 8.179$ kpc, as a function of azimuth. Shown is the strength of the spiral arms in black, as well as the f_{m_1,γ_1} and f_{m_2,γ_2} components in blue and red respectively. 78

4.4 Enclosed mass profile of our fiducial potential (black), compared to the constraints from dynamical modelling of satellite galaxies (magenta: Correa Magnus & Vasiliev 2022, green: Cautun et al. 2020) and streams (blue: Vasiliev et al. 2021, red: Koposov et al. 2023). 79

4.5 The top plot shows the surface density as a function of galactocentric radius as derived from our model (black line) with comparison to that derived from Bovy (2015). The red points are the measured values for the Milky Way from Bovy & Rix (2013). The bottom plot shows the vertical acceleration at $|z| = 400$ pc (dashed blue line) and $|z| = 1.1$ kpc (solid red line). The two colours of data points represents the vertical acceleration at different scale height with the blue points being at $|z| = 400$ pc (Widmark et al., 2022) and the red points at $|z| = 1.1$ kpc (Bovy & Rix, 2013). 81

4.6 Frequency curve as a function of Galactic radius. The solid black line is the rotational frequency curve of the potential, whereas the dashed and dot-dashed lines are rotional frequency plus or minus 0.25 and 0.5 times the epicyclic frequency, $\kappa_0(R) = \sqrt{(2\Omega/R)\mathrm{d}(R^2\Omega)/\mathrm{d}R}$. The horizontal blue and red lines are the pattern speed of the bar and the spiral arms, respectively. The vertical dashed and dot-dashed lines are the corresponding resonances for bar and spiral arms. 83

4.7 The relation between cellsize and density within our simulation. The cellsize in this case is the size of a square with the same area as the cell. 84

4.8 Longitude-velocity maps of the simulation observed from the Sun's position (placed at the origin of the overlayed coordinate system in Figure 4.9). The bar major axis is rotated by 28 degrees from the line of sight. Overlayed blue dashed lines are the spiral arm tracks of Reid et al. (2016, 2019) and McClure-Griffiths et al. (2004). The green points are the terminal velocities from H I and CO observations. *Top*: Full diagram. *Bottom*: Zoom in between $l = -60°$ & $+60°$ with the left plot only taking gas into account that lies within $R = 6$ kc from the centre and with the right one only considering gas further out. 87

4.9 The top plot is the $x-y$ density projection of our simulation at $t = 441$ Myr with the mask of overdensities from FILFINDER highlighting the spiral structure. The bottom figure is the polar decomposition of the density map of the top figure focusing on the region with Galactocentric radius $6 < R < 20$ kpc. The blue dotted lines are the positions of the spiral arms according to the second half of Equation (4.17). The green dashed lines are the spiral arms generated by the rotation of the bar, with a pitch angle of 6.5° around the outer Lindblad resonance, $R = 10.14$ kpc. The light blue lines indicate the spiral arm pattern extracted with FILFINDER. . 90

4.10 Estimated and real distance maps in the simulation. The black lines indicate the spiral arm pattern extracted with FILFINDER. The top plot shows the kinematic distance maps as estimated with Eq. (4.24). The middle plot is the map of the true distances to the gas cells. The relative error between the kinematic and true distance is shown in the bottom plot. 92

4.11 Distribution of relative kinematic distance error for different sampling annuli of true distances relative to the Sun's position. Here we represent relative errors that are ≤ -1 in orange, indicating where values are unphysical with zero or negative kinematic distance estimates. 93

4.12 The black line represents the median absolute relative kinematic distance error along the line-of-sight of a given Galactic longitude. Each plot represents a sampling annulus centred on the Sun. The blue shaded region is the median absolute deviation (MAD) of the error. The red shaded regions represent the Galactic longitudes where more than 20% of the cells along the line-of-sight have a relative kinematic distance error of 27% or more. 94

4.13 Probability distributions of the systematic kinematic distance errors within the overdensities in the bar region (blue) and the underdensities in the bar region (red). 96

4.14 Probability distributions of the systematic kinematic distance errors within the spiral arm region (blue) and the interarm regions (red). 97

4.15 Comparison of rotation curve against the average azimuthal velocity (black solid and dashed line respectively). The red and blue lines are the rotation curve from Brand & Blitz (1993) and Reid et al. (2014). . 99

4.16 The top plot illustrates LOS velocity map of the simulation. Similarly, the middle plot shows the map of the LOS velocity derived from the base axisymmetric potential. The last plot shows the difference between simulation and axisymmetric LOS velocities; top plot minus the middle plot. 101
4.17 The azimuthal profile of the difference between azimuthal and circular velocity (top) and the surface density (bottom) near solar circle, $R = 8.18$ kpc. The vertical dashed lines are the potential minima of the underlying spiral arm potential. Rotation of the system is from right to left. 102
4.18 2D probability density function of the relative error in the kinematic distance against the difference between the simulation and axisymmetric LOS velocities. The red dashed line is a power law with slope of 0.92. 103
4.19 Map of the kinematic distance error as a function of Galactic longitude and true distance. The contours are placed at $0, \pm0.1, \pm0.3, \pm0.5, \pm1, \pm1.5$ and ±2. The green lines indicate the spiral arms extracted with FILFINDER. Overplotted in orange are a selection of known sources using parallax distances as true distances (Wenger et al., 2018). 104

A.1 Maps of the magnetic field strength of the simulations carried out at $t = 2.40$ Myr. Line integral convolution (LIC) is used on the map to indicate the direction of the magnetic field in the x-y plane. 121
A.2 Same as figure A.1 but for the z component of the magnetic field . . . 122

B.1 The density maps of simulations of differing spiral arm strength at $t = 441$ Myr. The strength of the spiral arm pertibation increase from 10% to 30% stellar disk density at $R = 8.179$ kpc from top to bottom. . . . 124
B.2 Longitude velocity diagrams of our parameter study with $n = 2$ spiral arms with similar phase angle between the spiral arm potential and the bar. Left column is where we vary the pitch angle. The middle and right columns are the variation in spiral arm pattern speed and bar pattern speed respectively. 127
B.3 Same as Figure B.2 but with the $n = 4$ spiral arms subset. 128

List of Tables

3.1 Initial conditions that are altered between simulations. 44

4.1 Parameters for components 2 and 3 of the bar potential 76
4.2 Location of resonances of the non-axisymmetric components of the potential. 82
4.3 Expansion used for each component of the potential. When present, spiral arms are represented by a separate `CylSpline` potential, since they rotate with a different pattern speed than the bar. 85
4.4 Summarised values of the statistics between the different regions. Quantile difference indicates the difference between upper and lower percent quantile, for example 20% means the difference between the upper and lower 20% quantile. 98
4.5 Kinematic distances and errors of five sources. 103

A.1 List of collisional chemical reactions included in our chemical network 113
A.2 List of grain surface, cosmic ray and photochemical reactions included in our chemical network 115

B.1 Parameter values considered 126

List of Acronyms

AGAMA Action-based Galactic Modelling Architecture

AMR Adaptive Mesh Refinement

CCC Cloud-Cloud Collision

CNM Cold Neutral Medium

DM Dark Matter

GMC Giant Molecular Cloud

HIM Hot Ionised Medium

HLLD Harten-Lax-van Leer discontinuity

IRDC Infrared Dark Cloud

ISM Interstellar Medium

ISRF Interstellar Radiation Field

KD Kinematic Distance

LIC Line Integral Convolution

LMC Large Magellanic Clouds

LOS Line of Sight

LSR Local Standard of Rest

m2m Made-to-measure

MAD Median Absolute Deviation

MHD Magneto-Hydrodynamics

NFW Navarro, Frenk and White

PDF Probability Density Function

PDR Photodissociation region

SFR Star Formation Efficiency

SFR Star Formation Rate

SMC Small Magellanic Clouds

SPH Smooth Particle Hydrodynamics

WIM Warm Ionised Medium

WNM Warm Neutral Medium

List of Publications

Peer reviewed

1. **Hunter, G. H.**, Clark, P. C., Glover, S. C. O., & Klessen, R. S., "*Towards the impact of GMC collisions on the star formation rate*", 2023, MNRAS, 519, 4152

Submitted

1. **Hunter, G. H.**, Sormani, M. C., Beckmann, J. P., Vasiliev, E., Glover, S. C. O., Klessen, R. S., Soler, J. D., Brucy, N., et al., "*Testing kinematic distances under a realistic Galactic potential*" 2024, arXiv, arXiv:2403.18000

In loving memory of Thomas M. Hunter.
Thank you for nurturing my love for science.

Chapter 1

Introduction

"Life goes on and on and on. Keep moving forward as long as the road stretches ahead! Keep describing as long as the color persists! Keep shouting as long as the voice endures! We'll walk on!

—Halyosy, *Steppër*

All things within this universe are in constant motion. From the smallest atoms to the largest galaxy, everything experiences a force causing it to move. The interstellar medium (ISM) is no exception this rule. It is sculpted across all scaled by many forces: gravity causing it form elegant spiral arms and filaments in which stars are born; feedback from stars and supernovae creating large holes in which thermal energy can dissipate into the cosmos; and magnetic fields gently guiding the ISM where it needs to go.

The first indications of the ISM were observed by Nicolas-Claude Fabri de Peiresc in 1610, where with a refractor telescope he noted the diffuse nature of the Orion Nebula (M42), with the first publication by Johann Baptist Cysat of Lucerne in 1619 with comparisons to a comet seen in previous years. Since then, M42 was added to the Messier catalogue and has become a frequent source to study (Hillenbrand & Hartmann, 1998), leading to the discover of the Orion Molecular Complex (Menon, 1958; Tucker et al., 1973), connecting other existing nebulae in the region. The molecular cloud discovered would prove to be a great laboratory for exploring processes within the ISM. In this thesis we aim to explore the dynamical processes within the ISM and discuss the impact they have on both theoretical and observational quantities.

1.1 Interstellar Medium

1.1.1 Phases of the ISM

The ISM is very diverse environment, consisting gas and dust at various temperatures and density (Girichidis et al., 2020). In its simplest form, the ISM can be described as a series of phases in which the gas can exist. The first of which was a model proposed by Field (1965) where the ISM can be described as two distinct phases. Assuming atomic hydrogen (H I) as the constituent gas, the gas phase can be split into a cold, dense phase called the cold neutral medium (CNM), and a warm, diffuse phase called the warm neutral medium (WNM).

The CNM exists at temperatures of $T \sim 50{-}100$ K and number densities $n = 20{-}50$ cm^{-3}, whilst the WNM has higher temperatures of $T \sim 6000 - 10^4$K and an order magnitude lower density, $n = 0.2 - 0.5$ cm^{-3} (Wolfire et al., 2003; Girichidis et al., 2020). Under the Field model, the two phases exist in a pressure equilibrium. Gas existing with temperatures and densities between these regions are thermally unstable. If unstable towards the CNM, unstable gas will cool via collisional excitation of fine structure lines of metals, such as C II or O I, or via recombination of electrons onto dust grains (Wolfire et al., 2003). Conversely, the gas unstable towards the WNM is heated by the photoelectric effect from dust grains in the ISM, high energy photons and particles such as X-rays and cosmic rays, or by the photoionisation of carbon ($\mathrm{C} \longrightarrow \mathrm{C}^+$).

The two phase model proved to be rather restricting due to the presence of superheated gas caused by supernovae, increasing gas temperatures up to $T \sim 10^6$ K or higher. A three-phase model was developed by McKee & Ostriker (1977) to describe the warm components of the ISM. At $T \sim 10^4$ K, atomic hydrogen will ionise into H+. For ionized gas with similar densities to the WNM, a phase called the warm ionised medium (WIM) is formed when the WNM gas is ionized by photoionisation or by collisional ionisation (Draine, 2011). Energy injection by supernovae causes the gas to reach temperatures of $T \sim 10^6$ K and really diffuse, with densities of $n \sim 10^-2$ cm^{-3} forming the hot ionized medium (HIM). Here, the HIM maintains a state collisional ionisation equilibrium, where there is a balance between the collisional ionisation equilibrium and radiative cooling by recombination. At these temperatures, the cooling timescale for radiative cooling is significantly longer than that of the WIM due to how diffuse the HIM, $t_{\mathrm{cool}} \propto n^{-1}$, resulting in the persistence of the HIM.

H_2 formation and destruction

On the much colder end of the spectrum, clouds of molecular hydrogen (H_2) form with the CNM. The formation of molecular hydrogen is crucial process, not only for the formation of molecular clouds but also for subsequent star formation. The direct path way to form molecular hydrogen would be:

$$\mathrm{H} + \mathrm{H} \longrightarrow \mathrm{H_2} + \gamma$$

however, due to the low collisional time scales and low probability of emission from the collision, the reaction is not high enough to be the main mechanism for H_2 formation in the ISM (Latter & Black, 1991). Additionally, pathways involving ion-neutral reactions also have low reaction rates, with the additional likelihood of the ions, H^- and H_2^+, being lost due to photodetatchment and photodissociation respectively (Glover, 2003). Though, H_2 formation is still possible with the presence of dust in the ISM. H atoms can be adsorbed onto the surface of dust grains via van der Waals forces, providing a formation site for the atoms to form H_2 (Gould & Salpeter, 1963; Hollenbach & Salpeter, 1971). The timescale of H_2 formation with the Milky Way's ISM is:

$$t_{\mathrm{form,H_2}} \simeq \frac{1}{3 \times 10^{-17} n} \simeq 10^9 n^{-1} \text{ yr}. \tag{1.1}$$

Considering molecular gas forms at densities at $n > 10^2$ cm^{-3}, this gives arise to formation timescales of at least 10 Myr. This formation timescale can shorten to ~ 3 Myr in the presence of supersonic shocks (Glover & Mac Low, 2007a,b), whilst turbulence can also alter formation timescales (Micic et al., 2012). This indicates that the dynamics within the CNM also influence the process of H_2 formation (see Padoan et al., 2016; Hu et al., 2021).

Just as H_2 can be formed, it can be destroyed back into its atomic components. There are two main processes involved when considering the destruction of molecular gas:

- Collisional dissociation - This occurs when H_2 collides with either H_2, He or free electrons within the ISM with energies much greater than the dissociation energy of H_2 (4.5 eV). This requires the gas to be of a temperature of T$>$ 2000 K to achieve this affect. This only tends to apply in specific environments such as molecular outflows from AGN and star forming regions (e.g Flower et al., 2003).

$$\mathrm{H_2} + \mathrm{H} \longrightarrow \mathrm{H} + \mathrm{H} + \mathrm{H}$$

- Photodissociation - This can occur at much lower temperatures $T << 1000$ K. The process involves a two step process called spontaneous radiative dissociation.

The process begins with a H_2 molecule absorbs a UV photon of energy between 11.1 eV and 13.6 eV, exciting one of the electrons to a higher energy states ($B\ ^1\Sigma_g$ or $C\ ^1\Pi_u$). The electron then radiatively decays to a ground state. This results in either a vibrationally excited H_2 molecule (85% of reactions) or complete dissociation of the molecule (15% of reactions) (Stecher & Williams, 1967; van Dishoeck & Black, 1988).

$$H_2 + \gamma \longrightarrow H + H$$

The photodissociation process is more relevant for the context of molecular clouds due to the lower temperatures and higher densities present. Due to the narrow energy band needed for photodissociation, the process is subject to self-shielding, resulting in more H_2 being destroyed at lower column densities (Draine & Bertoldi, 1996). The column density at which molecular hydrogen is fully self-shielded is given by:

$$N \simeq 10^{20} G_0 n^{-1}\ \mathrm{cm}^{-2} \tag{1.2}$$

where G_0 is the radiation field in Habing units (Habing, 1968). This effect becomes important once column densities exceed $N \sim 10^{14}\ \mathrm{cm}^{-2}$ (Draine & Bertoldi, 1996).

1.1.2 Molecular clouds

Giant molecular clouds (GMCs) are the host for star forming environments within galaxies, forming the densest parts of the ISM. These clouds tend to exist at temperatures between 10 and 100K with number densities n$>$ 100 cm^{-3} (Girichidis et al., 2020). The boundary of these objects are marked by the transition between atomic and molecular gas due to the level self-shielding present, as discussed previously.

Observing clouds

In observational context, a direct observation of H_2 is not possible. This is due to the the temperatures needed for H_2 to emit being higher than the temperature of GMCs ($T \sim 500$ K for excitement of the first rotation level of H_2). A tracer therefore needs to be used to used to trace H_2. CO is the next abundant tracer with a small dipole moment that is easily excited, with the first transition at $T = 5.52$ K. A known factor can be used to convert between the column densities of the two molecules:

$$X_{\mathrm{CO}} = \frac{N_{\mathrm{H_2}}}{I_{\mathrm{CO}}} \tag{1.3}$$

where I_{CO} is the intensity of the CO emission (Bolatto et al., 2013). This factor is generally assumed to be a constant but simulations and observations have shown that

this can vary (Tielens & Hollenbach, 1985; Wolfire et al., 2010; Kohno & Sofue, 2024). The extent of a GMC is often defined by the extent of CO emission however, like H_2, CO is susceptible to photodissociation due to the interstellar radiation field (ISRF). The self-shielding effect for CO are not strong in comparison H_2 due to the lower column densities of CO present. Therefore, the derived size of the GMC is smaller in comparison to the actual extent of H_2 (Smith et al., 2014). Alternatives to CO emission include dust extinction measurements due to the dust being needed in H_2 formation (e.g Lombardi et al., 2014; Green et al., 2019), and C^+ being used as a tracer for CO dark due to its presence in the CO formation and destruction process (Glover & Smith, 2016).

GMC formation

After the formation of H_2, further accumulation of molecular gas is needed to form a molecular cloud and reach the column densities required for self-shielding of H_2. The formation of molecular clouds is an ongoing topic of research with many theories for their formation being proposed. Here, we highlight three mechanisms which can be split into two groups, "bottom-up" GMC formation and "top-down" GMC formation (Chevance et al., 2020).

The bottom-up approach is the approach of where smaller clouds form first and combine to form larger clouds. The first method providing this model is the coagulation model by Oort (1954) in where smaller atomic clouds, formed by thermal instabilities, undergo cloud-cloud collisions forming a larger cloud in the process (Tasker & Tan, 2009) At some point, the column densities within the cloud are high enough to enable self-shielding, allowing the transition from atomic to molecular gas and becoming molecular cloud. The cloud can then continue to accrete matter via collisions reaching much larger masses until the accretion is halted by the onset of star formation (Klessen & Glover, 2016).

The alternate bottom-up approach is via colliding flows. In this model, flows of warm atomic hydrogen collide together, becoming thermally unstable and rapidly cooling. At some point a cloud forms at the intersection, reaching densities high enough for self-shielding to occur and form molecular hydrogen (Heitsch et al., 2006; Inoue & Inutsuka, 2012).

Both these bottom-up approaches provide the necessary quantity of low-mass clouds but struggle to reproduce the GMC Mass function at the high-mass end $M > 10^6$ $M_\odot$.

The top-down approach attempts to account for the high-mass end of the GMC mass function (Chevance et al., 2020). The ISM itself can be prone to the gravitational instabilities within the disk of galaxies (Dobbs et al., 2014). Self-gravitating fragmen-

tation can occur in environments with higher surface densities in comparison to the average for the disk, such as spiral arms. These instabilities can produce clouds with large masses (upwards of 10^6 $M_\odot$), however the low mass end can only be formed once stars are formed and stellar feedback disrupts the larger cloud.

GMC structure

GMCs tend to have be on the order 10s-100s pc in size containing masses between 10^2 $M_\odot$ in smaller clouds, to 10^7 $M_\odot$ in the largest of clouds (Blitz, 1993; Oka et al., 2001; Schulz, 2012; Roman-Duval et al., 2010).

Observations have found filamentery structure present within these clouds with large clumps forming at the intersections of these filaments (e.g Hanawa et al., 1993; Kainulainen et al., 2017, for Orion A). Kinematic studies of GMC found that they are highly turbulent (Reynold's numbers 10^8), with flows being highly supersonic ($\mathcal{M} > 10$) (Heyer & Dame, 2015). Larson (1981) noted that the velocity dispersion of these turbulent clouds follow a power law relation with respect to the size of the cloud in question, $\sigma \propto L^{0.34}$, linking to his earlier work regarding a similar power law scaling for turbulence in the rest of the ISM (Larson, 1979). The turbulence present within a cloud can be quantified with a power spectrum or second order structure function as follows:

$$\sigma^2_\Delta(\tau) =< |v(r) - v(r+\tau)|^2 > \tag{1.4}$$

where τ is the displacement from position r. σ^2_Δ is often proportional to $\tau^{\beta-2}$ where β is some power. For isotropic and incompressible Kolmogorov turbulence, $\beta = \frac{11}{3}$ in 3D or $\beta = \frac{8}{3}$. When analysing kinematic data of GMC, observers find that the structure function of GMCs follows a power law, however β can vary between ~ 2 and ~ 3.1 suggesting some degree of compressiblity within the clouds.(Stutzki et al., 1998; Heyer & Brunt, 2004; Schneider et al., 2011; Monaci et al., 2023).

Due to the filamentary structure of clouds, most of the matter present in GMCs exists within dense "clumps". Probability density functions (PDF) of the density of observed clouds follow a log-normal distribution, with a power law tail towards high densities (e.g Schneider et al., 2013). The log-normal distribution is consistent with a turbulent medium as seen from simulations of turbulent boxes (e.g Federrath, 2015) whilst the power law tail is attributed to the gravitational collapse of clumps (Klessen, 2000).

The collapse of these clumps puts into question the stability of GMCs and how they are supported against gravitational collapse. There are two theories propose an answer to this:

- Gravoturbulent support - Turbulence within GMC counteracts the global collapse of the cloud, placing it in virial equilibrium. However, the turbulence causes overdensities to form and, when dense enough to contain a Jeans mass M_J of material, undergo gravitational collapse (Klessen, 2000; Mac Low & Klessen, 2004). The virial parameter is defined as:

$$\alpha_{\rm vir} \equiv \frac{3\sigma_v^2 R_{\rm GMC}}{5GM_{\rm GMC}} \tag{1.5}$$

  where σ_v is the velocity dispersion of the cloud, and $M_{\rm GMC}$ and $R_{\rm GMC}$ are the mass and size of the GMC respectively (Bertoldi & McKee, 1992). A value of $\alpha_{\rm vir} \lesssim 2$ indicates self-gravitation, with most clouds of $M > 10^5$ $M_\odot$ having $\alpha_{\rm vir} \sim 1$. Despite this, the turbulence present plus other physics such as magnetic fields can keep the prevent of the collapse of the overall clouds (Kauffmann et al., 2013).

- Hierarchical collapse - In this model (Vázquez-Semadeni et al., 2019), the turbulence present is not sufficient to support the GMC over long time scales due to the continued accretion of matter onto the cloud from the surrounding diffuse medium. This combined with the high density and cold temperatures of the cloud allow for the GMC to quickly exceed its Jeans mass. The resulting infall of the cloud induces further, more chaotic, turbulence into the cloud creating more gravtionally collapsing clumps in the process. The timescales in which these clumps collapse at are significantly shorter than that of the cloud average (Krause et al., 2020) resulting a nested body of collapsing matter, where with each collapse's matter is accreting onto the next, smaller collapsing region.

Cloud lifetimes

The inevitable collapse of a GMC will eventually result in the cloud being either converted into stars or the cloud being dispersed by the stellar feedback from the newly formed stars (Rahner et al., 2017, 2019; Jeffreson & Kruijssen, 2018). Only a few percent of the mass of a GMC will be converted into stars (Krumholz & Tan, 2007; Leroy et al., 2017; Krumholz et al., 2019).

Surveys of GMCs in external galaxies as well as clouds in the Milky Way estimate the lifetimes of these clouds to be ~ 10 Myr (Murray, 2011; Kruijssen et al., 2019; Zabel et al., 2020). If the collapse of a GMC was only opposed by the thermal pressure, the cloud will collapse on timescale similar to the freefall timescale:

$$t_{ff} = \sqrt{\frac{3\pi}{32G\rho}} \sim 3 \text{ Myr} \left(\frac{n}{10^2 \text{ cm}^{-3}}\right)^{-1/2}. \tag{1.6}$$

For typical densities of GMCs, $t_{ff} \sim 3$ Myr (Girichidis et al., 2020) which is almost an order of magnitude lower than the lifetimes of GMCs estimated from observations. This suggests there is some level of additional support provided within the cloud that slows down the collapse of the GMC, such as turbulence and magnetic fields, with turbulence being the biggest support against collapse (Krumholz & Tan, 2007; Crutcher et al., 2010; Klessen & Glover, 2016).

The depletion of molecular gas within the ISM of a galaxy happens on a much a longer timescale than the lifetimes of GMCs. The depletion timescale, defined as the molecular gas mass of a galaxy divided by the star formation rate (SFR), is on the order of a few Gyrs (Bigiel et al., 2008; Leroy et al., 2008). This indicates that the existence of GMCs are a short lived phase of the ISM, only converting a small fraction of its gas mass into stars (based on star formations effeciencies, Chevance et al., 2020) before being dissipated by the stars forming within.

1.1.3 Star formation

The turbulent structure of GMCs allow for the formation of clumps which exist at densities and temperatures higher and colder than the cloud average, respectively. At such high densities, the Jean's length of a given gas clump is significantly smaller than that of the cloud itself. A cloud is referred to as Jeans unstable if a perturbation to hydrostatic equilibrium of the cloud results in gravitational collapse (Jeans, 1902). By balancing thermal energy against gravitational energy, the characteristic Jeans length $\lambda_{\rm J}$ is obtained (for a spherical cloud):

$$\lambda_{\rm J} = \left(\frac{\pi c_s^2}{G\rho}\right)^{1/2} \sim 2.2 \text{ pc} \left(\frac{c_s}{0.2 \text{ kms}^{-1}}\right)\left(\frac{n}{10^2 \text{ cm}^{-3}}\right)^{-1/2} \tag{1.7}$$

and the Jeans mass $M_{\rm J}$:

$$M_{\rm J} = \frac{4\pi}{3}\rho\left(\frac{\lambda_{\rm J}}{2}\right)^3 \sim 34 \text{ M}_\odot \left(\frac{c_s}{0.2 \text{ kms}^{-1}}\right)^3\left(\frac{n}{10^2 \text{ cm}^{-3}}\right)^{-1/2} \tag{1.8}$$

where c_s is the gas sound speed, ρ and n are the cloud's mass and number density respectively. These create a criterion where if the cloud is smaller than its Jeans length, $R < \lambda_{\rm J}$, or equivalently if the mass of inside of a Jean length exceeds that of the Jeans mass, $M > M_{\rm J}$, the cloud is unstable and will undergo gravitational collapse (Bodenheimer, 2011).

For densities and temperatures of clumps, $n \sim 10^5$ cm^{-3} and T 10K, the given resulting Jeans lengths and masses are on the order of ~ 6 pc and ~ 1 M$_\odot$ respectively (Krause et al., 2020). This indicates that only a few solar masses of material is needed

to undergo gravitational collapse and form stars. The freefall timescale t_{ff} is significantly shorter for clumps than GMC, with $t_{ff} \sim 0.1$ Myr (Hoyle, 1953). As such, the collapsing GMC is likely to fragment into smaller collapsing clumps, only stopping once the gas no longer behaves isothermally.

When looking at the star formation rate of the Milky Way with respect to the freefall time of the gas clouds within the Galaxy, there is a clear difference between the observed Galactic SFR and the SFR implied by freefall, with a difference on the order 2 magnitudes in difference, $\mathrm{SFR_{MW}}$ 1 $\mathrm{M_\odot\ yr^{-1}}$ vs $\mathrm{SFR_{ff}} \sim 200\ \mathrm{M_\odot\ yr^{-1}}$ (McKee & Williams, 1997; Chomiuk & Povich, 2011; Leroy et al., 2012). This implies that for the Milky Way, the star formation efficiency (SFE) is on the order 1%. Defining the SFE, ϵ as the ratio between the gas mass turned into stars M_* and total matter in the GMC M_{GMC},

$$\epsilon = \frac{M_*}{M_* + M_{\mathrm{GMC}}}. \tag{1.9}$$

In GMCs within the Milky Way and nearby galaxies, the ϵ varies between 0.3% and 3% at at GMC scales (Krumholz & Tan, 2007; Leroy et al., 2017; Krumholz et al., 2019), and increases to 3% - 6% within dense subregions within the cloud. The low SFEs can be explained by "fast and inefficient star formation" (Chevance et al., 2020). Due to short timescales needed to form stars $t \sim 1$ Myr (Palla & Stahler, 1999; Elmegreen, 2007; Hartmann et al., 2012), the onset of feedback from the newly formed stars occurs on timescales smaller than that of freefall time of the GMC causing the GMC to disperse before more stars can form (Kruijssen et al., 2019; Chevance et al., 2022).

1.2 Galactic dynamics

The ISM of a galaxy is shaped by the mutual gravitational attraction between the gas, existing stars and the underlying dark matter, along with motions induced by supernovae, stellar feedback and magnetic fields. To understand the impact this has on the processes within the ISM discussed previously, a understanding of the sources of motion needs to be established. Here we discuss the role of galactic dynamics within the galactic ISM.

1.2.1 Gravitational force

At the largest scales, gravitational force is the most dominant force in shaping the ISM. Each object within the galaxy experiences a gravitational attraction under Newton's

inverse square law of gravity. The force between two objects is given by

$$\mathbf{F}_{21} = \frac{Gm_1m_2}{|\mathbf{x}_2 - \mathbf{x}_1|^3}(\mathbf{x}_2 - \mathbf{x}_1) \tag{1.10}$$

where G is the gravitational constant, m_1 andm_2 are the masses of the two objects and $\mathbf{x}_1$ and $\mathbf{x}_2$ are the vector positions of the two objects. Since a galaxy contains on the order of 100 billions stars alone, the contributing force of each object $\delta\mathbf{F}$ can be summed together:

$$\mathbf{F}(\mathbf{x}) = \sum \delta\mathbf{F} = Gm \sum \frac{\mathbf{x}' - \mathbf{x}}{|\mathbf{x}' - \mathbf{x}|^3}\delta m(\mathbf{x}'). \tag{1.11}$$

Each mass element δm can be described as a volume with constant density, $\delta m(\mathbf{x}) = \rho(\mathbf{x})d\mathbf{x}^3$. Putting this back into equation 1.11:

$$\mathbf{F}(\mathbf{x}) = Gm \int \frac{\mathbf{x}' - \mathbf{x}}{|\mathbf{x}' - \mathbf{x}|^3}\rho(\mathbf{x}')d^3\mathbf{x}' \tag{1.12}$$

giving a description of the gravitational force as function of the mass density of the galaxy, removing the discretisation of individual stars. (Binney & Tremaine, 2008).

The gravitational potential Φ is defined as the work done W per unit mass needed to take an object from a position infinity to $\mathbf{x}$. This gives:

$$\Phi(\mathbf{x}) = \frac{W}{m} = \frac{1}{m}\int_{\infty}^{\mathbf{x}} \mathbf{F}(\mathbf{x}_\prime) \cdot d^3\mathbf{x}_\prime = -G \int \frac{\rho(\mathbf{x}')}{|\mathbf{x}' - \mathbf{x}|}d^3\mathbf{x}' \tag{1.13}$$

creating a relation between the potential of the galaxy and its density profile. By considering the gravitational flux through a unit sphere and applying the divergence theorem, we obtain Poisson's equation:

$$\nabla^2\Phi = 4\pi G\rho, \tag{1.14}$$

a differential equation form of equation 1.13. This equation provides the basis for calculating potential of a galaxy based on its mass density; a parameter which can be modelled from observations (Bovy & Rix, 2013; McMillan, 2017; Nitschai et al., 2021).

1.2.2 Velocity curves

The core parameter these models need to match is the circular velocity curve of the galaxy, $v_c(R)$. The circular velocity is defined as the velocity at which a particle needs to remain in a circular orbit at a given radius R.

$$v_c^2 = r|\mathbf{F}(r)| = r\frac{d\Phi}{dr} = \frac{GM(R)}{r} \tag{1.15}$$

Assuming circular motion within a galaxy, the circular velocity curve can be approximated by the rotation curve of the galaxy. There are multiple methods to obtain

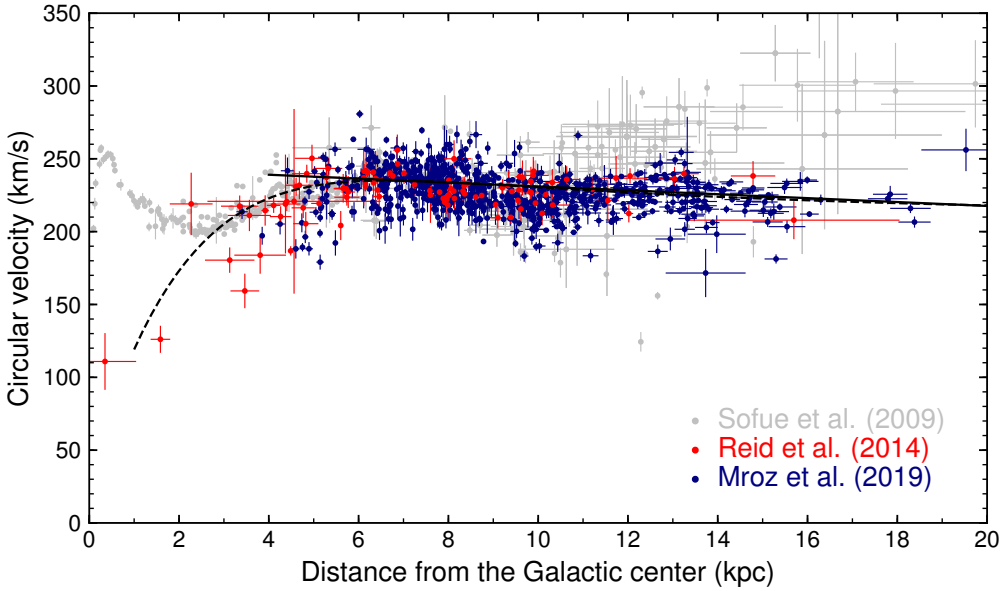

Figure 1.1. Circular-velocity curve of the Milky Way from different tracers. In grey is the rotation curve from Sofue et al. (2009), obtained from H I (Burton & Gordon, 1978; Fich et al., 1989) and CO (Clemens, 1985) tangential velocities, CO and H II regions (Blitz et al., 1982; Fich et al., 1989) and carbon star kinematics (Demers & Battinelli, 2007). In red and blue are the circular velocities obtained from maser parallaxes (Reid et al., 2014) and parallaxes of Classical Cepheids with *Gaia* (Mróz et al., 2019) respectively. (Adapted from Mróz et al., 2019, .)

rotation curves depending if one is looking at the Milky Way or at nearby galaxies. For nearby galaxies, the main method is to measure the spectral Doppler shifts of gas tracers such as H I (Roberts & Whitehurst, 1975; Walter et al., 2008; de Blok et al., 2008), H II and optical (Williams et al., 2021; Emsellem et al., 2022), and molecular lines such as CO (Lang et al., 2020). The line-of-sight velocity $v_{\rm LOS}$ gives only a component of the total circular velocity of a galaxy if the galaxy is not edge on, where $v_{\rm LOS} = v_c \sin(i)$ and i is the inclination angle. In the case of a (near) face-on galaxy, $i \sim 0°$, the rotation curve is not obtainable. This approach eventually lead to the discovery of the Tully-Fisher relation, a power law relation which relates the luminosity of a galaxy to its circular velocity (Tully & Fisher, 1977; Sakai et al., 2000).

Within the Milky Way, slightly different approaches need to be taken since we lie within the Galaxy. The closer proximity of the gas within the Milky Way and higher resolution of the gas kinematics allows for gas to exist with different line-of-sight velocities along a given galactic longitude l. This, combined with uncertainties involved in determining distances to gas clouds, makes it difficult for a rotation curve to be easily

established using the average $v_{\rm LOS}$ used for other galaxies. A work around is to assume the maximum velocity along a given line-of-sight, known as the terminal velocity $v_{\rm term}$, exists at the tangent point; the point where a circle of radius $R_0 \sin(l)$ is tangential to a straight line going starting from the Sun at radius R_0 in the direction of l. This is traced by the maximum $|v_{\rm lsr}(l)|$ in the longitude-velocity lv diagrams. Assuming complete circular motions the circular velocity curve can be obtained by:

$$v_c(R) = |v_{\rm term}(l)| + v_0 |\sin(l)| \tag{1.16}$$

where v_0 is the circular velocity of the Galaxy at solar position R_0. This approach works well within the inner parts of the galaxy, constraining the velocity curve for $R < R_0$. Like with external galaxies, this method uses gas kinematic data in H I (Burton & Gordon, 1978; Fich et al., 1989; McClure-Griffiths & Dickey, 2007) and CO (Clemens, 1985).

The rotation curve can also be obtained from stellar and maser kinematics. The distance to the objects is determined either via parallax approaches for maser sources (used in Reid et al., 2014) and luminous red giant stars stars (by Eilers et al., 2019), or the period-luminosity relation for Cepheid variable stars (used by Mróz et al., 2019). The constrained distance allows for the calculation of the tangential velocity with respect to the sky via proper motion estimates. The heliocentric line-of-sight velocity of the object v_h is constrained from spectrographic data of stars (Majewski et al., 2017) or spectral lines such as methanol and CO for maser sources (Reid et al., 2014). The kinematic data is transformed into the reference frame of the local standard of rest (LSR):

$$v_{\rm LSR} = v_h + U_\odot \cos(b)\cos(l) + V_\odot \cos(b)\sin(l) + W_\odot \sin(b) \tag{1.17}$$

where $(U_\odot, V_\odot, W_\odot)$ is the velocity components of the Sun with respect to the LSR. With the proper motion and $v_{\rm LSR}$, further modelling with methods, such as Jean's modelling (Binney & Tremaine, 2008) and maximising likelihood functions, the rotation curve for the Milky Way can be constrained from 4 kpc up to 200 kpc from the Galactic centre (Bhattacharjee et al., 2014).

The rotation curve of the Milky Way and different galaxies resulted in one of the most controversial discoveries being made. When comparing the mass estimates implied from the rotation curve of galaxies to that from luminosity profiles, there is a large difference between the two (Bosma, 1978; Rubin et al., 1980; Begeman et al., 1991). The expected rotation curve based on the luminosity profiles would have decreased with galactic radius, however it remained fairly constant. This provided the foundations for the work on dark matter and paved the way for cosmological simulations (Ostriker & Peebles, 1973; Ostriker et al., 1974).

Resonances

Stars within a potential, whilst on average follow a circular orbit, do experience a level of radial oscillation. This arises when a star experiences any motion outwith the azimuthal direction. The orbital path makes a rosette shaped, referred to as loop orbits (Binney & Tremaine, 2008). For a given star with a given angular momentum and energy, the orbit can be decomposed into two components: a small circular orbit with a diameter equal to the extent of the radial oscillation, and a large circular orbit around the galaxy at a radius R_g, where R_g is the guiding centre and is defined by the radius at which the centre of the smaller orbit is located. The frequency of the smaller orbit, and by extension the radial oscillation, is called the epicyclic frequency and is defined as:

$$\kappa^2(R_g) = \left(R\frac{d\Omega^2}{dR} + 4\Omega^2\right)\Big|_{R_g} \tag{1.18}$$

where $\Omega = v_c/R$ is the angular velocity of a star within a potential.

If we consider a $m-$fold perturbation rotating with a pattern speed Ω_p in an axisymmetric potential, the resonances are defined as:

$$m(\Omega_p - \Omega) = n\kappa. \tag{1.19}$$

Co-rotation occurs when $n = 0$ and is the resonance at which a star rotates with same angular velocity as the perturbation itself. $n = \pm 1$ gives rise to the Lindblad resonances where positive n defines the inner Lindblad resonance, the point where a star overtakes the perturbation and interacts with the perturbation at a frequency equal to the epicyclic frequency, κ. Conversely, negative n defines the outer Lindblad resonance, the point where the star is slower than perturbation but still experiences the perturbation at a frequency equal to the epicyclic frequency.

These resonances are crucial in the formation of non-axisymmetric structure within galaxies due to being the points at which energy is exchanged between the stars and gas, and the underlying galactic potential (Binney & Tremaine, 2008; Sellwood, 2011).

1.2.3 Potential models

The underlying potential of a galaxy can contain a few components, such as bars, disks and dark matter halos. Each component covers different scales and can have different shaped depending on their density profile. By treating the matter inside galaxies as a collisionless particle system, any component in a galaxy that is in a steady state must suffice the collisionless Boltzmann equation (Binney & Tremaine, 2008):

$$\frac{\partial f}{\partial t} + \sum_{i=0}^{3} v_i \frac{\partial f}{\partial x_i} - \frac{\partial \Phi}{\partial x_i}\frac{\partial f}{\partial v_i} = 0 \tag{1.20}$$

where $f(\mathbf{x}, \mathbf{v}, t)$ is the distribution function of the matter in a galaxy in 6-dimensional phase space $(\mathbf{x}, \mathbf{v})$ at a given time t. By integrating the distribution function in velocity space, we obtain the spatial density of matter in the galaxy $\nu(\mathbf{x})$ which is equivalent to a mass density ρ (for modelling dark matter halos) or stellar number density n. By multiplying the collsional Boltzmann equation with powers of v (Eqn. 1.20), the Jeans equations are obtained:

$$\frac{\partial \nu}{\partial t} + \sum_{i=1}^{3} \frac{\partial(\nu \overline{v_i})}{\partial x_i} = 0 \tag{1.21}$$

$$\frac{\partial(\nu \overline{v_j})}{\partial t} + \sum_{i=1}^{3} \frac{\partial(\nu \overline{v_i v_j})}{\partial x_i} + \nu \frac{\partial \Phi}{\partial x_j} = 0 \tag{1.22}$$

$$\nu \frac{\partial(\overline{v_j})}{\partial t} + \sum_{i=1}^{3} \nu \overline{v_i} \frac{\partial(\overline{v_j})}{\partial x_i} = -\nu \frac{\partial \Phi}{\partial x_j} - \sum_{i=1}^{3} \frac{\partial(\nu \sigma_{ij}^2)}{\partial x_i} \tag{1.23}$$

Equation 1.21 is the continuity equation and equations 1.22 & 1.23 are the force equations with the latter being a re-write of the former to make analogies to the Eular's equation of motion for fluid flow. Here, $\overline{v_i}$ is the mean velocity or first moment of the distribution function, $\overline{v_i v_j}$ is the second moment, and $\sigma_{ij}^2 = \overline{v_i v_j} - \overline{v_i v_j}$ is the velocity dispersion tensor.

These equations plus Poisson's equation (Eqn. 1.14) provide the framework for Jeans modelling in which many potentials have been developed and parameterised to describe the potentials of galaxies. Most notable are the dark matter halos of galaxies inferred from observations and simulations.

Dark Matter Halos

To describe the flat rotation curves observed caused by dark matter, various density profiles for the dark matter halo were proposed in the later half of the the 20th century. The first of these models was by Jaffe (1983), proposing $\rho \propto r^{-2}(r + r_s)^{-2}$ where r_s is a scale length to fit of light profiles of Virgo cluster elliptical galaxies. This was dubbed as as an improvement and, at the time, was "better than existing models", such as the light profile of de Vaucouleurs (1948). This started the spherical double power law family of spherical potentials which have the general form of:

$$\rho(r) = \frac{\rho_0}{(r/a)^{\alpha}(1 + r/a)^{\beta - \alpha}} \tag{1.24}$$

where ρ_0 is the normalising density, a is the scale length and α and β are the power laws of the profile. Most dark matter halos can be described with $1 < \alpha < 1.5$ and $\beta \simeq 1.5$ (Binney & Tremaine, 2008). Some specific values of α and β have unique names and provide analytical solutions to Poisson's equation.

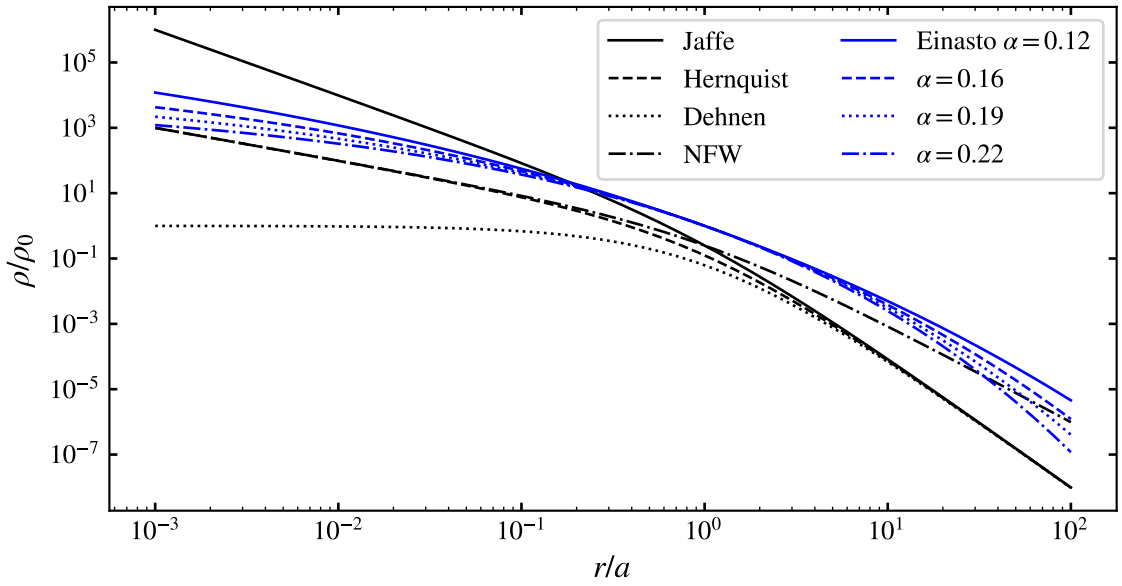

Figure 1.2. The density profile of the dark matter halo discussed in section 1.2.3. In black are the halo potentials discussed by the double power law profile (Eqn. 1.24) with ρ_0 and a being the normalising density and scale radius respectively. The blue lines represent the Einasto profile (Eqn. 1.26) with $\rho_0 = \rho_{-2}$ and $a = r_{-2}$ being the density and radius where the slope of the profile is equal to -2.

- Jaffe - $\alpha = 2$, $\beta = 4$: The original double power law relation from Jaffe (1983).
- Hernquist - $\alpha = 1$, $\beta = 4$: A developed alternative to the Jaffe model by Hernquist (1990) based on the mass profiles and dynamics of elliptical galaxies.
- Dehnen - $\beta = 4$: A family of potential-density pairs with free choice of α between values 0 and 3 presented by Dehnen (1993). The base density profile is given by:

$$\rho = \frac{(3-\alpha)M}{4\pi} \frac{a}{r^{\alpha}(r+a)^{4-\alpha}} \tag{1.25}$$

  where M is the mass of the halo in question.
- Navarro, Frenk and White (NFW) - $\alpha = 1$, $\beta = 3$: A profile developed from cosmological simulations with N-body dynamics and smoothed particle hydrodynamics by Navarro et al. (1995).

These profiles are very similar in shape with only the steepness of their slopes changing (see figure 1.2). Each profile provides a fit to a sample of galaxy halos and with the free parameters of (Eqn. 1.24), most spherically shaped galactic halos can be modelled.

An alternative to the double power law spherical model for halos is the Einasto (1969) profile. This profile is an exponential profile with power law function inside the

exponent:

$$\rho(r) = \rho_{-2} \exp\left[\frac{-2}{\alpha}\left\{\left(\frac{r}{r_{-2}}\right)^{\alpha} - 1\right\}\right] \tag{1.26}$$

where ρ_{-2} and r_{-2} is the density and radius respectively where $\rho(r) \propto r^{-2}$. The profile is similar in shape to the others discussed in this section but has the advantages of only one free parameter, α, and takes on different shapes depending on the value. The values of α can vary between 0.12 and 0.25 based on halo concentrations in cosmological simulations (Gao et al., 2008).

This profile has shown to fit density profiles of dark matter in halos in simulations (Navarro et al., 2004) and has proven to be a better fit to rotation curves of galaxies (Chemin et al., 2011). Of recent years, the Einasto has been adapted to model the contraction of dark matter halos (Cautun et al., 2020; Correa Magnus & Vasiliev, 2022; Wang et al., 2022).

Disks

The modelling of stellar disks within galaxies follows on naturally from the modelling of elliptical galaxies and by extension dark matter halos. The de Vaucouleurs profile for elliptical galaxies is a generalisation for the Sérsic profile to described stellar light profiles of galaxies with Sérsic index n=4 (Sérsic, 1963). The relation is given by:

$$I(R) = I_0 \exp\left(-kR^{1/n}\right) \tag{1.27}$$

where I is the intensity observed and k is a constant. When looking at galaxies with disks, it was found that the intensity follows an exponential decay $I(R) \propto e^{-kR}$, equivalent an Sérsic index of $n = 1$ (de Vaucouleurs, 1959). Since the light intensity of a galaxy is proportional to its stellar density, it would imply the the stellar disk of a galaxy follows a similar relation; $\rho(R) \propto e^{-kR}$.

The first models relating this property to galactic dynamics was by Freeman (1970) where, using the light profiles of 36 disk galaxies, derived an expression for the rotation curve from the idea of exponential disk. The disk density can be approximated in some cases by a razor-thin disk:

$$\rho(R, z) = \Sigma(R)\delta(z) \tag{1.28}$$

where Σ is the surface density and $\delta(z)$ is a Dirac delta function. This results in a potential of:

$$\Phi(R, z) = -2\pi G e^{-k|z|} J_0(kR) \tag{1.29}$$

where k is some constant and J_0 is the Bessel function of first kind and 0th order. Whilst this approximation works, in reality galaxies are 3 dimensional objects with some thickness in their disks.

In the context of the Milky Way, Gilmore & Reid (1983) showed that the thickness of the Galactic disk follows two exponential profiles, one associated with young stellar population, referred to as the *thin disk*, and the older stellar population, referred to as the *thick disk* and is described by:

$$\rho(R,z)_d = \Sigma_0 e^{-R/R_d}\left(\frac{\alpha_0}{2z_0}e^{-|z|/z_0} + \frac{\alpha_1}{2z_1}e^{-|z|/z1}\right) \tag{1.30}$$

where R_d is the disk scale length, z_0 and z_1 are the scales heights of the thin and thick disks, and α_0 and α_1 are constants such that $\alpha_0+\alpha_1 = 1$. This has been shown to be quite an effective potential to describe the stellar disk of the Milky Way from observation of stars across the galaxy (Jurić et al., 2008; Bovy & Rix, 2013; Widmark et al., 2022).

For the gas disk, a steeper profile is needed in the vertical direction due to how the gas is concentrated in the midplane. McMillan (2017) proposed the use of a sech^2 profile for the thickness of the gas disk based on the 3D H I maps of the Milky Way from Kalberla & Dedes (2008). Modifying the disk potential of Dehnen & Binney (1998) to reflect the sech^2 profile, we get:

$$\rho(R,z)_d = \frac{\Sigma_d}{z_d}\exp\left(-\frac{R}{R_d} - \frac{Rm}{R}\right)\mathrm{sech}^2(z/2z_d) \tag{1.31}$$

where is R_d is the gas disk scale length, z_d is the gas disk scale height and R_m is a term to enforce a decrease in the gas density towards the galactic centre to reflect the lower gas density present with $R < 4$ kpc (Dame et al., 1987). This additional component to the Galactic potential contributed by the gas disk helps explain the vertical motions observed in stars at larger heights above the disk (McMillan, 2017).

Whilst these thicker disks provide realistic density profiles for galactic disks, the potential Φ cannot be obtained analytically via Poisson's equation. Instead, numerical methods are required to calculate the potential, details of which will be discussed in chapter 2.

Bars and perturbations

So far the potentials we have discussed have been are either spherically symmetrical or axisymmetric around the z-axis. However, observations have shown numerous galaxies break these symmetries with up to 45% of galaxies containing a bar (Aguerri et al., 2009), and $\sim 60\%$ of galaxies in the local universe are either irregular or spiral shaped in nature (Loveday, 1996).

The bars of galaxies are an elongated shaped region at the centre of some galaxies where the stars are typically intermediately aged or older ($t_{\mathrm{age}} > 2$ Myr) (Neumann et al., 2020). The formation of bars within galaxies is relatively unknown process however two processes have been proposed:

- Orbit trapping - stars in highly elliptical, eccentric orbits aligning their orbits within the centres of galaxies, resulting box orbits within galactic centres (Lynden-Bell, 1979; Polyachenko & Shukhman, 2015, 2020).

- Standing cavity wave - instabilities in the galactic disk cause a cavity to open between the galactic centre and the co-rotation radius creating a standing wave in the region. This generates swing amplification causing a positive feedback loop, increasing the density of stars within the bar. Eventually an inner Lindblad resonance forms, halting the feedback loop and stabilising the bar (Toomre, 1981; Sellwood & Evans, 2001).

In either case of formation mechanism, cosmological simulations have shown a galaxy has increased likelihood of having a bar with increasing stellar to dark matter mass ratio in the centre of galaxies (Rosas-Guevara et al., 2020; López et al., 2024).

The elongated ellipsoid shape of a bar typical has an axis ratio of 3:1 (Athanassoula et al., 1990) and being notably thicker than the disk itself. This allows for the bar potential to be modelled as a triaxial shaped distribution, allowing for the use of "squashed" spherical power-law distributions, such as the one in Binney et al. (1991) where:

$$\rho(a) = \rho_0 \left(\frac{a}{a_0} \right)^{-\alpha} \tag{1.32}$$

where $a = \sqrt{x^2 + (y^2 + z^2)/q_m^2}$. The shaping parameter q_m is what turn the spherical power law distribution into an elongated, triaxial one, where $q_m = 1$ returns a spherical distribution. This works for more simplistic models, however observations of both the Milky Way's bar (Wegg & Gerhard, 2013; Wegg et al., 2015), and external galaxies (Kuijken & Dubinski, 1995; Merrifield & Kuijken, 1999; Chung & Bureau, 2004) as well as simulations (Combes & Sanders, 1981; Athanassoula, 2005) show that bars can take on a boxy-peanut/X-shaped profile. Modelling these profiles are difficult in nature but made-to-measure models of the Milky Way's by Portail et al. (2017) and analytical analogues (Wegg et al., 2015; Coleman et al., 2020; Sormani et al., 2022b) have provide dynamicists multiple profiles to explore bar potentials of galaxies.

The other type of perturbation that is often explored and modelled are the spiral arms of galaxies. Grand design spiral galaxies, whilst only making up $\sim 10\%$ of galaxies, act as a great laboratory for spiral arm perturbations. Typically they contain an even number of spiral arms which is equivalent to a m-order perturbation where $m = 2, 4, 6 \ldots$. The spiral arms in these galaxies are believed to form from either the rotation of their bars (Buta et al., 2009) or from interactions with companion galaxies, such in the case for M51 (Dobbs et al., 2010; Tress et al., 2020a, 2021).

For flocculent galaxies, the spiral arms are less regular and are believed to be a result of instabilities within the disks of these galaxies. The mechanism behind these instabilities is not fully known though two theories are proposed for the mechanism. Density wave theory is one mechanism developed by Lin & Shu (1964) describes the spiral arm perturbation as quasi-steady state perturbation in which a standing wave is formed between the Lindblad resonances, amplifying the structure between forming a long lasting overdensity in the both the gas and stellar distributions, similar to that of bar formation. This theory requires a dynamically cold outer disk, and hot inner disk which is very a specific set of conditions which is not always achieved. The alternative is perturbations caused by overdensities, small mergers, and grooves in the phase space of galaxies, all of which can create spiral patterns (Goldreich & Lynden-Bell, 1965; Toomre, 1990; De Rijcke & Voulis, 2016), however these perturbations would decay quickly.

The spiral arms in these galaxies tend to follow a logarithmic spiral pattern where for a given spiral arm $\phi = 1/k \ln(R/a)$ where k and a are constants. Turning this into shaping function for an $m-$order perturbation within an axisymmetric disk:

$$f(R) = \frac{m}{\tan(i)} \ln \frac{R}{R_a} \tag{1.33}$$

where i is the pitch angle of the spiral shape and R_a is the radius where the spiral crosses the $x-axis$. Considering a rotating spiral arm model, the potential can be decomposed into two parts $\Phi = \Phi_0 + \Phi_1$ where Φ_0 are the axisymmetric terms of the potential and Φ_1 is the spiral perturbation. Following density wave theory, spiral arms would rotate through a galaxy with a fixed pattern speed Ω_s. Relaying this to the potential gives:

$$\Phi_1(R, \phi, t) = \Phi_a(R) e^{i(m\phi - \Omega_s t - f(R)} \tag{1.34}$$

where Φ_a is some axisymmetric potential and $f(R)$ is the shaping function, like the logarithmic spiral. Different spiral arm profiles have been explored over the years, some of these include the sinusoidal spiral arm modal of Cox & Gómez (2002) and Gaussian profiled spiral arms (Junqueira et al., 2013; Li et al., 2022). The shaping function has been explored as well, with multiple papers by Reid et al. mapping masers to the spiral arms of the Milky Way (Reid et al., 2014, 2016, 2019) and mapping to stellar density maps from Gaia (Eilers et al., 2020).

All the potentials discussed in this section provide the base work to our model of the Galactic potential, details of which are discussed in 4.

1.3 About this thesis

In this thesis we aim to explore how the dynamics of the ISM impact on both direct and derived quantities. Within this chapter we have had a brief overview of the processes involved within GMCs as well as the larger scale galactic dynamics. We continue our overview by discussing the numerical techniques used as part of this thesis in chapter 2.

It is shown in both simulations and many observation the cloud-cloud collisions are regular occurrence within galaxies (Tasker & Tan, 2009; Dobbs et al., 2015; Fukui et al., 2021). In chapter 3 we look into how the collisions of GMCs impact subsequent star formation within said clouds. We perform a suite of MHD simulations to allow for the comparison between star formation rates, virial state of clumps/cores within the clouds and the resulting alignment between magnetic and velocity fields. Our parameter space covers a range of collisional velocity, initial magnetic field inclinations and effective resolution within the simulations.

Assumptions made about the dynamics of gas within the Milky Way can lead to large deviations from true values. This is the topic of chapter 4 where we explore how reliable the assumption circular motion within the Galaxy is for kinematic distance estimate. We present a new analytic model for the gravitational model for the Milky Way making use of existing models to describe the centre of the Galaxy, as well as using constraints from observations to parameterise our analytic models. Making use of 2D isothermal hydrodynamics simulations, we simulate the gas of the Milky Way; gradually introducing non-axisymmetric components of our potential (such as the bar and spiral arms) to induce radial motions into the gas. From there we place an observer within the simulation to calculate distance to the gas cells within the simulation via the kinematic distance method. We generate longitude-error maps from the data to give observers constrains on where kinematic distances are reliable within the Galaxy.

Lastly we conclude the thesis with an overview of our findings in chapter 5, with additional discussion on future works being developed from these results.

Chapter 2

Numerical methodology

"I have learned so much since then, years have gone by. My mistakes have become experience points. I wonder if I have evolved like you?"

—PinocchioP, *The Pokémon inside my heart*

Within this thesis, we have made use of the numerical hydrodynamics code Arepo in order simulate the environments within the Galactic ISM (Springel, 2010a). In addition, Arepo was integrated with Action-based Galaxy Modelling Architecture (Agama) for the Galactic scale dynamics introduced in chapter 4 (Vasiliev, 2019). In this chapter, we go into the base physics behind these codes and provide an insight into how these codes operate. We further discuss details on how the two codes are interfaced together.

2.1 Arepo, moving-mesh hydrodynamics

2.1.1 Overview of hydrodynamics

Most processes in the ISM involve the dynamics of atomic and molecular gas. As such, the gas is best described as fluid following the conservation laws of hydrodynamics. Here, a choice of reference frame needs to be made in order to describe the system; a Eularian frame of reference in which an observer is positioned at a specific point within the system as it evolves, or a Lagrangian frame of reference where the observer moves with the flow of the fluid.

In the Eularian reference frame, the conservation laws for an ideal, inviscid adiabatic fluid are as described as follows:

- Conservation of mass

$$\frac{\partial \rho}{\partial t} - \nabla \cdot (\rho \mathbf{v}) = 0 \tag{2.1}$$

where ρ is the density of the fluid and $\mathbf{v}$ is the flow velocity of fluid.

- Conservation of momentum

$$\rho\Big(\frac{\partial \mathbf{v}}{\partial t} - (\mathbf{v}\cdot\nabla)\mathbf{v}\Big) = -\nabla P + \rho\mathbf{F} \tag{2.2}$$

where P is the fluid pressure and $\mathbf{F}$ is any external forces acting on the system, such as gravity or momentum injection from supernovae.

- Conservation of energy

$$\frac{\partial \epsilon}{\partial t} + \mathbf{v}\cdot\nabla\epsilon = -P\nabla\cdot\mathbf{v} + L \tag{2.3}$$

where ϵ is the energy density of the system and L are all the additional heating and cooling terms that can arise in the system, such as time-dependent chemistry and feedback from stars. The energy density is defined in its base form as the total energy contributions from thermal and kinetic energy:

$$\epsilon = e_{\rm th} + \frac{|\mathbf{v}|^2}{2}. \tag{2.4}$$

The thermal energy of the system, $e_{\rm th}$, is obtained from the ideal gas law:

$$P = (\gamma - 1)\rho e_{\rm th} \tag{2.5}$$

where γ is the adiabatic index of the gas, typically with $\gamma = \frac{5}{3}$ for an monoatomic gas.

In order to obtain the Lagrangian form of these equations, the comoving derivative needs to be used:

$$\frac{\mathrm{D}}{\mathrm{D}t} = \frac{\partial}{\partial t} - \mathbf{v}\cdot\nabla. \tag{2.6}$$

Applying this to the hydrodynamic equations (Eqn. 2.1-2.3) we can obtain the corresponding equations in the Lagrangian frame. These are:

$$\frac{\mathrm{D}\rho}{\mathrm{D}t} = -\rho\nabla\cdot\mathbf{v}, \tag{2.7}$$

$$\rho\frac{\mathrm{D}\mathbf{v}}{\mathrm{D}t} = -\nabla P + \rho\mathbf{F}, \tag{2.8}$$

and

$$\frac{\mathrm{D}\epsilon}{\mathrm{D}t} = -P\nabla\cdot\mathbf{v} + L. \tag{2.9}$$

These equations assume the gas is inviscid and not magnetised. These equations can be modified to account for viscosity or the presence magnetic fields within the gas (see 3.2.1 for details on magneto-hydrodyanmics, MHD). Addtionally, these equation only

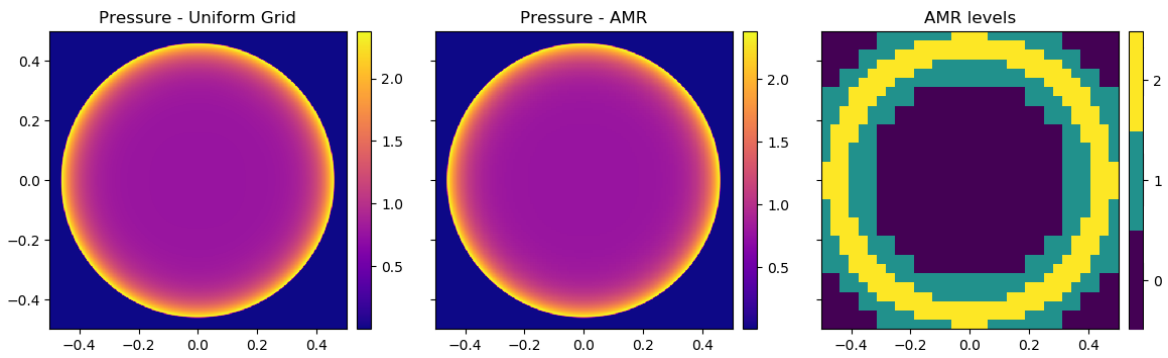

Figure 2.1. Projection of hydrodynamic blast wave using the AMR code `Athena++`. Left hand panel shows the blast wave with a uniform grid, middle panel shows it with AMR and the right hand panel shows the levels of refinement. (Figure credit: Stone et al., 2020)

hold if there are no discontinuities in the system, otherwise the integral form of these equations must be used to obtain any results.

These equations, whilst can describe a lot of systems, can only be solved in analytically in a select few systems, such as a steady-state, incompressible flow, resulting in the need for numerical approaches to solve these equations. Many hydrodynamical codes have been developed to simulate these systems and usually fall into one of two types; grid/mesh codes and smooth particles dynamics (SPH) codes.

Grid/mesh codes

Grid codes follow the Eularien approach to hydrodynamics by constructing a fixed grid or mesh where the hydrodynamical quantities of the gas are stored in each grid cell, subdividing and discretizating the simulation domain. The codes then update the quantities in each cell with each timestep by treating each cell interface as a local Riemann problem; treating each interface as a discontinuity and numerically solving the fluxes across them.

Some codes allow for the further discretization of the cells called refinement. This process splits the cells into 2^n subcells based on certain criterion, where n is the number of dimensions of the system. Density thresholds are a typical criterion for refinement, however location, velocity thresholds and other criterion can also be used to activate refinement. Conversely, grid cells can merge together in a process called derefinement. Codes that are able to refine and derefine during the simulation are referred to as adaptive mesh refinement (AMR) codes. Examples of these codes include `Ramses` (Teyssier, 2002) and `Athena++` (Stone et al., 2020). An example of blast wave in `Athena++` can be found in figure 2.1 where the levels of refinement used can be seen.

AMR codes have the advantage of being able to resolve shocks and discontinuities due to the nature of using Riemann solvers for solving across cell faces. Additionally, obtaining projections and slices of the system are easier to obtain due to the presence of the grid. However due to the finite resolution and sqaure/cubic nature of the grid, artifacts in the system can arise. These can propagate through the system producing results that may be unphysical.

Smooth particle hydrodynamics

Smooth particle hydrodyanmics (SPH) is a Lagrangian approach to solving the hydrodynamical equations in which hydrodynamical quantities are mapped to particles, first developed for astronomical simulations by Lucy (1977) and Gingold & Monaghan (1977). The approach makes use of a kernel summation interpolant in which a given quantity F is smoothed and mapped onto a particle with:

$$F_s(\mathbf{r}) = \int F(\mathbf{r}')W(\mathbf{r}-\mathbf{r}', h)\mathrm{d}\mathbf{r}' \tag{2.10}$$

where F_s is the smoothed quantity and W is a the kernel in which the given quantity is smoothed across a length h (smoothing length) with $\int W(\mathbf{r})\mathrm{d}\mathbf{r} = 1$. The kernel used is typically some kind of Gaussian or Gaussian-like profile, for example a cubic spline approximation where $W(r,h) = w(\frac{r}{2h})$:

$$w_{3\mathrm{D}}(q) = \frac{8}{\pi}\begin{cases} 1-6q^2+6^3, & 0 \leq q \leq \frac{1}{2} \\ 2(1-q)^3, & \frac{1}{2} < q \leq 1 \\ 0. & q > 1 \end{cases} \tag{2.11}$$

An example of the smoothing kernel can be seen figure 2.2.

Descritising equation 2.10 for N particles in a system and treating $\Delta\mathbf{r}_i \sim \frac{m_i}{\rho_i}$ given that each particle has a mass and density associated with it, we obtain:

$$F_s(\mathbf{r}_i) \simeq \sum_{j=1}^{N} \frac{m_j}{\rho_j} F_j W(\mathbf{r}_i - \mathbf{r}_j, h). \tag{2.12}$$

This provides the basis for converting the Lagrangian equations of hydrodynamics for a SPH system. After the particles have the quantities needed for the simulation, the simulation is evolved in a manner similar to N-body simulations where the acceleration on each particle is calculated, the velocity is advanced by a timestep according to the acceleration, and finally the particle moves position due to it updated velocity.

SPH, due to its simplicity, easily conserves mass, momentum, energy and entropy really well. Additionally, SPH is Galilean invarient. The resolution of the system follows the density of system by construction, where more particles are present in denser

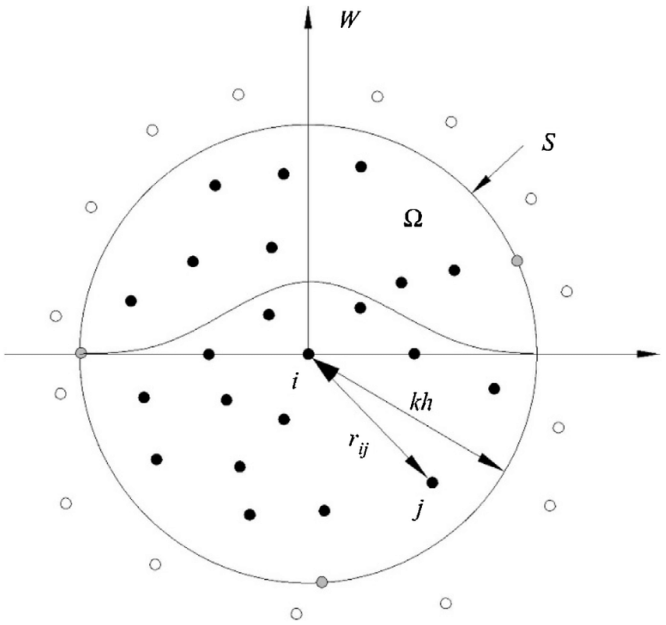

Figure 2.2. An example of a particle distribution around a central SPH particle i. All black particles within the kernel radius kh contribute to the fluid quantities of particle i. All white particles fall out of the kernel and do not contribute. The shape of the kernel W is shown on the $x - y$ axis. (Figure credit: Liang et al., 2019)

regions of the simulation. This allows for density contrasts to be resolved well. In an astronomical setting, SPH codes can be coupled to N-body codes easier to further incorporate gravitational forces experienced in astronomical simulations.

Where SPH struggles is resolving shocks, in which in a shocked system increases in entropy. An artificial viscosity needs to be added in the momentum and energy conservation equations in order to allow for the increase in entropy. This additional viscosity causes much higher dissipation within the system, additional entropy in systems that conserve entropy (e.g. sheer flows) and has no physical motivation for its existence. The particle nature of SPH means that the particles can "jiggle" due to repulsion present by pressure gradients in the simulation. This adds a level of noise that is not present in grid based codes.

Many SPH codes have been developed for astrophysical contexts such as `Gadget` (Springel, 2005a; Springel et al., 2021), `GIZMO` (Hopkins, 2015) and `Gasoline` (Wadsley et al., 2004, 2017).

2.1.2 Details of AREPO

A third type of hydrodynamical code comes in the form of moving-mesh codes. Moving-mesh codes are mix of the two previous methods; descritising a simulation domain into

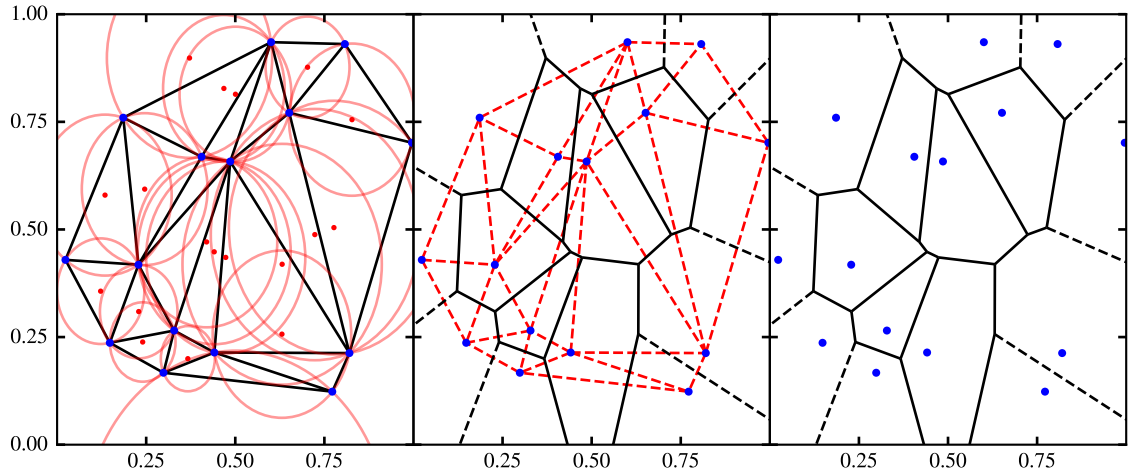

Figure 2.3. The generation of a Voronoi tesselation from a Delaunay triangulation with the circumcircles and circumcentres as the red circles and points respectively. The left plot depicts an example Delaunay triangulation with the vertices (mesh-generating points) in blue. The middle and right plots show the resulting Voronoi tesselation from the Delaunay triangulation (red dashed lines in middle plot).

cells like an a grid code and allows them to move with the flow of gas in a manner similar to SPH codes. We make use of such a code called AREPO in this thesis. AREPO is a cosmological MHD code which uses a Voronoi tesselation as the mesh for the simulation (Springel, 2010a; Pakmor et al., 2011; Weinberger et al., 2020). The advantage of using a moving-mesh code is that it allows for Galilean invariant system that is still able to treat shocks without the need of artificial viscosity.

The initial conditions of an AREPO provide the structure for the initial tesselation. Similar to SPH, a set of particles are assigned with fluid quantities and are used as the mesh-generating points for the Voronoi tesselation. This involves constructing a Delaunay triangulation, a type of mesh that consists of only triangles where the mesh-generating points are located at the vertices of the triangles. The circumcircle of a given triangle within the triangulation does not contain additional mesh generation points. The vertices of the Voronoi tesselation lie at the centre of the circumcircles and connecting the vertices results in the Voronoi tesselation (see figure 2.3).

Once the tesselation is established, the simulation evolves as follows. For each timestep Δt:

1. The fluid quantities of each cell are computed based on the conserved quantities of the hydrodynamic equations; density from conservation of mass, velocity from conservation of momentum, and pressure from conservation of energy.

2. The gradients of each fluid quantity are computed and velocities are assigned to

each mesh-generating point based on the gradients.

3. The fluid quantities are evolved by treating each Voronoi cell interface as a Riemann problem by computing fluxes through the interfaces, similar to AMR codes.

4. Finally, the mesh-generating points move accordingly with their velocity for the timestep.

The cell sizes are adaptive by nature in which they can get smaller as mesh-generating points get closer, however further refinement and derefinement based on the mass of the cell or by other criterion is possible. For refinement, a new mesh generating point is inserted beside the existing one inside the cell. The Voronoi cell is then split in half and the conserved quantities for each cell are calculated based on the volume of the new refined cells. Similarly, derefinement is achieved by removing the mesh-generating point and having the surrounding cells receiving the conserved quantities from the derefined cell.

Many other forms of physics can be included into AREPO such as self-gravity, external potentials, chemistry, supernova and stellar feedback. These all allow for the exploration of many types of systems. These includes cosmological boxes with `Illustris` (Vogelsberger et al., 2014) and `IllustrisTNG` (Pillepich et al., 2018; Springel et al., 2018) suit of simulations, individual galaxies (Smith et al., 2014; Tress et al., 2020a; Whitworth et al., 2023), clouds and star forming regions (Clark et al., 2019; Jones et al., 2023), and evolving supernovae (Pakmor et al., 2013; Pais et al., 2018).

2.2 AGAMA, gravitational dynamics library

2.2.1 Treatment of gravity in simulations

Gravity is one of the most important forces that all objects within the universe experience. In the context of astrophysics, the gravitational force is a crucial force in defining the motions of astronomical objects. It is necessary that the treatment of gravity is correct within simulations.

The most accurate way of obtaining the gravitational forces acting on an object is with direct N-body summation, in which the forces acting on the object are calculated with respect to all other objects within the simulation. The force acting on a given object i in a system of N objects is given by:

$$\mathbf{F}_i = \sum_{\substack{j=1 \\ j\neq i}}^{N} \frac{G m_i m_j (\mathbf{r}_j - \mathbf{r}_i)}{|\mathbf{r}_j - \mathbf{r}_i|^3}, \tag{2.13}$$

where m_i and r_i are the mass and vector positions respectively, and G is the gravitational constant. Two-body ($N = 2$) systems can easily be computed analytically, whilst systems with more bodies require simplifications and/or numerical methods to solve. One such simplification is the restricted three-body problem in which one of the particles in a $N = 3$ system is considered as massless and orbits around the system. This can be used to determine the orbit of stars located on the outskirts of a stellar system (Szebehely, 1967; Henon, 1997; Valtonen & Karttunen, 2006).

The direct summation approach presented in Equation 2.13 can be very computationally intensive when $N > 10^3$ particles due to the $\mathcal{O}(N^2)$ calculation that is required to compute the forces on all the particles. Approaches have been introduced to ease computation to $\mathcal{O}(N)$ or $\mathcal{O}(N \ln N)$.

- Tree code, $\mathcal{O}(N \ln N)$ - A method developed by Barnes & Hut (1986) in which the simulation domain is split into an octree (quadtree in 2D); nested regions of 2x2x2 cubes (2x2 squares) creating a tree-like structure with a single particle being potentially at the bottom. The force each particle experience is a combination of direct N-body force of all particles within the same region and treating regions further away as a single particle with the total mass of that region as its mass and centre-of-mass as its position.

- Particle mesh, $\mathcal{O}(N_{\mathrm{grid}} \ln N_{\mathrm{grid}})$ & $\mathcal{O}(N_{\mathrm{particles}})$ - This method takes the particle distribution of the system and maps it into a density grid using a window function, similar manner to SPH, where:

$$\rho_{\mathrm{grid},i} = \frac{1}{h^3} \sum_{j=1}^{N} m_{\mathrm{part},j} W(\mathbf{x}_{\mathrm{part},j} - \mathbf{x}_{\mathrm{grid},i}) \tag{2.14}$$

  where grid and part refer to the grid cell and particle respectively, and h is the length of a grid cell. W is a window function in which maps the mass to a number of cells depending on the form of W; this can be either n^3 cells nearest to the particle where $n = 1, 2$ or 3. Making use of Poisson's equation (Eqn. 1.14) and integrating, the gravitational potential can be described as a convolution between the density and the Green's function, g:

$$\Phi(\mathbf{x}) = -\int \frac{G\rho(\mathbf{x}')}{|\mathbf{x}' - \mathbf{x}|} \mathrm{d}\mathbf{x}' = \int g(\mathbf{x}' - \mathbf{x}) \rho(\mathbf{x}') \mathrm{d}\mathbf{x}' = g * \rho. \tag{2.15}$$

  The Fourier transform of a convolution is the product of the Fourier transforms of each function in the convolution. Using this property, the gravitational potential in Fourier space can be calculated by using the density Fourier transform:

$$\tilde{\Phi}(\mathbf{k}) = -\frac{4\pi G}{\mathbf{k}^2} \tilde{\rho}(\mathbf{k}). \tag{2.16}$$

The forces then acting on each particle can the be calculated by Fourier transforming the Fourier potential $\tilde{\Phi}$ and differentiating the resulting potential.

AREPO makes use of both approaches when computing self-gravity within the system. When both approaches are used in a simulation, tree code is used for short range range interactions whilst the particle mesh approach is used for long range interactions (Springel, 2010a; Weinberger et al., 2020).

In systems where the gravitational potential remains rather constant, or can be approximated by an analytic expression, the potential can be precomputed prior to the simulation running. This requires significantly less computation, making the calculation of the acceleration an $\mathcal{O}(N)$ calculation instead. In chapter 4 we implement this technique for the Milky Way potential making use of the gravitaional dynamics library AGAMA.

2.2.2 Constructing potentials with AGAMA

AGAMA, action based galaxy modeling architecture, is a galaxy dynamics and modelling library in C++ and Python developed by Vasiliev (2019). The code provides a toolbox to explore the dynamics and potentials of galaxies making use of multiple methods to do so.

The primary method in the code is the calculation of potentials. AGAMA provides many of the standard potentials used in galactic dynamics as discussed in 1.2, such as Plummer, NFW and Dehnen potentials. A complete list of available potential profiles can be found in the AGAMA documentation (Vasiliev, 2018). Additionally, a user-defined density or potential function describing the potential can be used. The "potential factory" framework of the code allows the user to define a potential, return an C++/Python class object which can be used to obtain quantities of the potential such as local density, potential and forces, enclosed and total masses, and orbital periods of test particles.

The potential is generated in one of three ways: analytic solution, multipole expansion (`Multipole`) or cylindrical Fourier expansion (`CylSpline`). The analytic solution is the simplest approach and quickest to compute of the methods, making use of the previously described list of standard potentials, however this only applies to potentials with both a analytic form for both the density profile *and* potential profile. If there is only a density profile or there is no analytic function, one of the expansions are required.

Multipole expansion

The multipole expansion approach to calculate the potential is recommended for systems that are spheroidal in shape (e.g an Einasto (1969) potential for dark matter halos).

The multipole expansion approach is a standard method to evaluating the potential (Binney & Tremaine, 2008, Chapter 2.4). This allows for the potential at a given point to be expressed as a summation of spherical harmonics:

$$\rho(r,\theta,\phi) = \sum_{l=0}^{\infty}\sum_{m=-l}^{+l} \rho_{l,m}(r) Y_l^m(\theta,\phi) \tag{2.17}$$

and

$$\Phi(r,\theta,\phi) = \sum_{l=0}^{\infty}\sum_{m=-l}^{+l} \Phi_{l,m}(r) Y_l^m(\theta,\phi) \tag{2.18}$$

where $\rho_{l,m}$ and $\Phi_{l,m}$ are the expansion coefficient of the density and potential functions respectively and Y_l^m are the spherical harmonics. The spherical harmonics used here are product of the normalised associated Legendre polynomials, $\tilde{P}_l^m(x)$ with $x = \cos(\theta)$ and trigonometric functions of $m\phi$:

$$Y_l^m(\theta,\phi) = \sqrt{4\pi}\tilde{P}_l^m(\cos\theta)\ \mathrm{trig}m\phi, \tag{2.19}$$

$$\mathrm{trig}m\phi = \begin{cases} 0, & m = 0 \\ \sqrt{2}\cos m\phi, & m > 0 \\ \sqrt{2}\sin|m|\phi & m < 1 \end{cases}.$$

The coefficients of the expansions, $f_l^m = \{\rho_{l,m}, \Phi_{l,m}\}$, can be found by exploiting the orthogonality of the spherical harmonics; multiplying each side of equation 2.17 & 2.18 by the complex conjugate and integrating over all solid angles:

$$f_{l,m}(r) = \int_0^{\pi}\int_0^{2\pi} f(r,\theta,\phi) Y_l^m(\theta,\phi) A_{l,m} d\phi d\theta \tag{2.20}$$

where f is either the density or potential function, ρ or Φ, and $A_{l,m}$ is a normalising coefficient. Each coefficient is a function of radius r and is computed on a logarithmic radial grid spanning the domain of the potential. Poisson's equation can be used to obtain the potential coefficients $\Phi_{l,m}$ from the density coefficients by integrating in r as the ϕ and θ dependence were eliminated in the previous step. This is achieved by:

$$\Phi_{l,m} = -\frac{4\pi G}{2l+1}\left[r^{-1-1}\int_0^r \rho_{l,m}(r') r'^{l+2} dr' + r^l \int_r^{\infty} \rho_{l,m}(r') r'^{1-l} dr'\right]. \tag{2.21}$$

Typically these kinds of expansions require the maximum l to be between 4 and 8 for most spherical shaped systems, and with certain symmetries the coefficients can automatically be set to 0 saving computational time. However this becomes more computationally expensive with highly flattened systems, requiring much higher maximum of l (for example, $l = 0..36$ in Holley-Bockelmann et al., 2005). A different approach is then required to save computation as the spherical harmonic approach due to the scaling of $\mathcal{O}(n_{\mathrm{grid}} \times 2l^2)$. AGAMA provides this with either the disk ansatz approach of Kuijken & Dubinski (1995) (not used in this thesis) or with cylindrical Fourier expansions in R and z.

CylSpline - cylindrical Fourier expansion

The Fourier expansion approach to calculating the potential is an alternative to the multipole expansion when the potential is flattened, for example disk and bar potentials. For a given function $f(R, z, \phi)$ where f can be either density ρ or potential Φ, its Fourier expansion in cylindrical coordinates is:

$$f(R, z, \phi) = \sum_{m=0}^{\infty} f_m(R, z) \exp(im\phi) \tag{2.22}$$

where f_m is the Fourier expansion coefficient of order m. Since the expansion occurs in the azimuthal angle ϕ, the expansion allows for more detailed variation of potential in z direction needed for modelling flat-shaped potentials. The coefficients $f_m(R, z)$ are computed by Fourier transforming $f(R, z, \phi)$ in azimuth. The coefficients are evaluated in a double logarithmic grid in R and z with quintic spline interpolation used to compute points in between, similar to the of the radial grid of the multipole expansion. The elimination of the azimuthal dependence makes solving Poisson's equation easier, allowing for the computation of the potential coefficients $\Phi_m(R, z)$ from the density coefficients $\rho_m(R, z)$:

$$\Phi_m(R, z) = -G \int_{-\infty}^{\infty} \int_{0}^{\infty} \rho_m(R', z') \Xi_m(R, z, R', z') dR' dz'. \tag{2.23}$$

Here Ξ_m is the Green's function in cylindrical coordinates. Within AGAMA, this is evaluated as:

$$\Xi_m = \begin{cases} \frac{1}{\pi\sqrt{RR'}} Q_{m-1/2}\left(\frac{R^2+R'^2+(z-z')^2}{2RR'}\right), & \text{if } R > 0, R' > 0 \\ \frac{1}{\sqrt{R^2+R'^2+(z-z')^2}}, & \text{if } R = 0 \text{ or } R' = 0, \text{ and } m = 0, \\ 0, & \text{otherwise} \end{cases} \tag{2.24}$$

where Q is the Legendre function of the second kind.

With the need of a second dimension needed to compute coefficients, Fourier expansion method is computationally more expensive than the multipole expansion, $\mathcal{O}(n_{\text{grid},r} \times n_{\text{grid},z} \times m)$. However, the ability to resolve variations in the potential in the z direction can be crucial in some disk and bar models due to the exponential nature of their height (for example, the disks in McMillan, 2017). A clear example of how the grids are sampled with multipole expansion and cylindrical Fourier expansion can be seen figure 2.4.

AGAMA allows for the combination of different potentials to form a composite potential. These composites can contain all 3 descriptions of calculating a potential, useful for including the various components needed for a complete galactic potential. We make use of these composite potentials in chapter 4 to establish the potential of simulation.

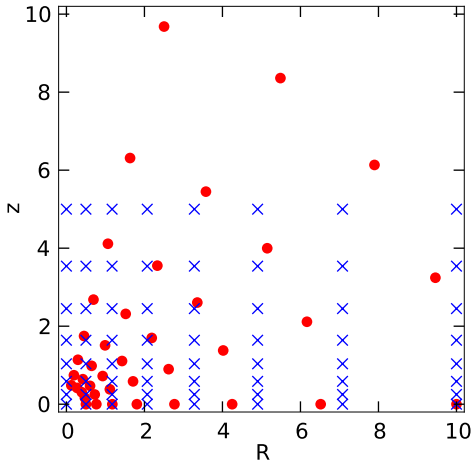

Figure 2.4. An illustration indicating the grid that is formed with the multipole expansion (red dots) and cyldrical Fourier expansion (blue crosses) in the R, z-place. Both grids have 8 grid points in the radial direction, 5 angular point within the multipole expansion (equivalent to $l_{\max} = 8$), and 8 grid points in the z direction for the Fourier expansion. (Figure credit: Vasiliev, 2019).

2.2.3 Interfacing AGAMA into AREPO

In order to explore the dynamics of a Milky Way-like Galaxy in chapter 4, an interface was developed between AGAMA and AREPO. The interface interacts with the `EXTERNALGRAVITY` framework of AREPO to adjust the acceleration the gas experiences. The two steps involved are as follows:

1. At the beginning of the simulation, load the potential. The potential is read from files that contain either the parameters to go into the analytical functions in AGAMA via the "potential factory", or loads the complete grid of expansion coefficients. This returns an Agama potential object, containing the composite potential needed for the simulation.

2. When AREPO makes a call to the `EXTERNALGRAVITY` framework to update the acceleration, a call to the potential object produced in the previous step is made. This returns the value of the potential Φ and the acceleration $\mathbf{a} = -\nabla\Phi$ at the position of the gas cell. These values are updated and the simulation is advance by the corresponding timestep Δt. This step is repeated for each cell and timestep as needed.

This interface is adaptable to any potential provided the corresponding parameter and/or expansion coefficient file exists, allowing for simulations of different types of galaxies to be explored. The code to the interface can be found at the GitHub repository

for AGAMA[1].

[1] https://github.com/GalacticDynamics-Oxford/Agama

Chapter 3

Star formation induced by cloud-cloud collisions

"Find a reason to sing. If I were to sing with you, I wouldn't feel alone for the first time."

—Halyosy, *Connecting*

This work presented in this chapter is based on the paper Hunter et al. (2023) which has been published in the Monthly Notices of the Royal Astronomical Society (MNRAS) in 2023. I am the first author of the paper and conducted all the simulation and data analysis present within the paper and this chapter. The paper was primarily written by myself with feedback and insight from co-authors and referees. Specifically, Simon Glover provided text on how the chemical network present within the simulations is constructed, details of which can be found in appendix A.1.

Abstract

Collisions between giant molecular clouds (GMCs) are one of the pathways for massive star formation, due to the high densities created. However the enhancement of the star formation rate (SFR) is not well constrained. In this study we perform a parameter study of cloud-cloud collisions, and investigate how the resulting SFR depends on the details of set-up. Our parameter study explores variations in: collision speed; magnetic field inclination (with respect to the collisional axis); and resolution, as defined by the number of cells per Jeans length. In all our collision simulations we find a factor of 2-3 increase in the SFR compared to our no collision simulation, with star formation beginning sooner with a) high collisional velocities, b) parallel orientation between the magnetic field and collision axis, c) and lower resolution. The mean virial parameter of high density (and thus possible star-forming) gas increases with collisional velocity,

but has little variation with magnetic field inclination. The alignment of the velocity and magnetic field remains uniform in low density environments but becomes more perpendicular with increasing density, indicating the compression of the magnetic field by collapsing gas. Comparing the trends in the SFR with other GMC collision studies, we find good agreement with studies that account for the gravitational boundedness of the gas in their star formation algorithm, but not with those that simply form stars above a prescribed density threshold. This suggests that the latter approach should be used with caution when modelling star formation on resolved cloud scales.

3.1 Introduction

Giant molecular clouds (GMCs) are large regions of gravitationally bound gas that exist within galaxies. These clouds typically span 1–100 pc in size and contain on the order $\sim 10^4$–$10^6 M_\odot$ of molecular gas, giving them typical hydrogen densities of $\sim$100 cm^{-3} (Blitz, 1993; Roman-Duval et al., 2010). GMCs have temperatures of $\sim 10 - 30$ K, a factor of 2-10 times lower than the temperature of the surrounding Cold Neutral Medium (CNM) component of the interstellar medium (ISM). Due to their low temperatures and molecular nature, the main observational tracers of GMC properties are dust continuum emission and molecular line emission (from e.g. CO/HCN/N_2H^+), which are used to observe GMCs within the Milky Way as well as in nearby galaxies (Fukui et al., 1999; Dame et al., 2001; André et al., 2010; Leroy et al., 2021).

Embedded within these GMCs are cooler dense clumps, the more massive of which are often observed as Infrared Dark Cloud (IRDCs). These clumps are accepted to be the precursor to star formation (Tan et al., 2014) due to their temperatures of 10-20 K (Chira et al., 2013) and higher number densities of $n_{H_2} = 10^4 - 10^6 \mathrm{cm}^{-3}$ (Motte et al., 2018). Each clump will likely form a cluster of stars due to further fragmentation and their relatively large mass reservoir (10^2–$10^5 M_\odot$) (Motte et al., 2018). Despite many observations of these clumps, the process by which these clumps form is not fully understood. Some theoretical models have been proposed that explain how a GMC can fragment and further collapse; such as turbulence (Krumholz & McKee, 2005a), stellar and supernova feedback (Wareing et al., 2017) and converging gas flows, i.e collisions (Scoville et al., 1986; Wu et al., 2017).

Numerical simulations of galactic disks have shown that GMC collisions are a recurring event due to the quasi-2D geometry of the distribution of dense molecular gas in most disk galaxies along with the differential rotation created by the gravitational potential of the galaxy (Tasker & Tan, 2009). Estimates of the mean time between collisions range from $\sim$ 20% (Dobbs et al., 2015) to $\sim$ 50% (Sun et al., in prep.) of the

orbital period of the clouds around the centre of the galaxy. Although this is a factor of a few longer than recent observational estimates of cloud lifetimes – between 10-30 Myr (Chevance et al., 2020) – it nevertheless implies that GMC collisions should be relatively common events. This is supported by the many observations of cloud collisions found within the Milky Way; for instance, Fukui et al. (2021) identify ∼50 GMCs that are candidates to be the product of cloud-cloud collisions (CCCs). However, collisions are not limited to the disks of galaxies. Cloud collisions have been observed in the Small and Large Magellanic Clouds (SMC and LMC) (Fukui et al., 2019; Tokuda et al., 2019; Neelamkodan et al., 2021) and theorised to occur with extreme collisional velocities in the centre of the Milky Way (Sormani et al., 2019). In the case of the SMC and LMC, these clouds collide as a result of large scale HI flows caused by the tidal interactions of these satellite galaxies (Fukui et al., 2017). As for the centre of the galaxy, Sormani et al. (2019) argues the gas flow caused by the galactic bar crashes into the Central Molecular Zone, a ring of molecular gas surrounding the Milky Way nucleus, providing the ideal conditions for clouds to collide.

A variety of GMC collision simulations have been performed to explore various topics: such as observational signature of collisons (e.g. Haworth et al., 2015); triggering of high-mass star formation (e.g. Takahira et al., 2014; Balfour et al., 2015); and enhancement of the star formation rate, in both non-identical GMC collisions (e.g. Habe & Ohta, 1992) and identical GMC collsions (e.g. Wu et al., 2017; Liow & Dobbs, 2020; Tanvir & Dale, 2020). Habe & Ohta (1992) and Takahira et al. (2014) show that the collision of a smaller cloud with a larger cloud creates a cavity and compression layer in which densities are reached that are high enough for high-mass stars to form. This is consistent with observations, for example of the Gum 11 cloud in the Carina Nebula Complex by Fujita et al. (2021), where CO observations indicate the presence of colliding clouds with a cavity, and with a massive star, HD92206, in close proximity to the compressed layer.

However, while there is general agreement that cloud-cloud collisions should enhance star formation, there is little agreement on *how much* the star formation rate is increased by a cloud-cloud collision. Recent simulations by Tanvir & Dale (2020) and Liow & Dobbs (2020) find that the star formation rate increases by a factor of two or less for collisions with relative velocities $v_{\rm rel} \leq 20\,{\rm km\,s^{-1}}$, typical of the majority of mergers that we expect to occur in a Milky-Way type spiral galaxy (Skarbinski et al., 2022). On the other hand, Wu et al. (2017) find an order of magnitude increase in the star formation rate for a collision with a relative velocity of $10\,{\rm km\,s^{-1}}$. The cause of the substantial discrepancy between the Wu et al. (2017) results and the results of the other cloud collision simulations is unclear, as the simulations differ in both their numerical

approach[1] and their initial conditions. In particular, Wu et al. (2017) include a magnetic field in many of their simulations, while the other studies consider only the purely hydrodynamical case.[2] It is therefore not clear whether the difference in outcomes of these studies is a consequence of the different initial conditions adopted, or instead is a consequence of the choice of numerical approach.

In this chapter, we attempt to improve our understanding of the effect of collisions on the star-formation rate in magnetised clouds by performing a series of simulations of cloud collisions with different relative velocities and magnetic field orientations using a state-of-the-art MHD code – the AREPO moving-mesh code (Springel, 2010b) – and a sophisticated treatment of the microphysics of the gas (see Clark et al. 2019 and our Appendix A.1) and the formation of stars (see Wollenberg et al. 2020 and Section 3.2.3). Importantly, for our fiducial case, we adopt the same initial conditions as in Wu et al. (2017; hereafter, W17), allowing us to directly assess whether the large boost in the star formation rate that they find in their study is due to their choice of initial conditions or to their numerical approach.

The structure of our paper as follows. In Section 3.2 we discuss the numerical approach taken, the initial conditions used for each simulation and how the star formation is implemented. In Section 3.3 we present our results from the simulation, with a focus on the structure of the GMC, the star formation rate and the virial parameter of the cloud. We conclude with a comparison of our results to other literature results in Section 3.4 and a summary of our findings in Section 3.5.

[1] Liow & Dobbs (2020) and Tanvir & Dale (2020) use smoothed particle hydrodynamics (SPH) and model star formation with sink particles, while Wu et al. (2017) use an Eulerian grid code and model star formation with star particles. Both SPH studies adopt an isothermal equation of state, whereas Wu et al. (2017) employ a more realistic treatment of the heating and cooling that can occur during the collision, based on the microphysics of the interstellar medium.

[2] Other potentially important differences include the choice of initial cloud mass and relative velocity. Tanvir & Dale (2020) consider an initial relative velocity of $10\,\mathrm{km\,s^{-1}}$, as in W17, but simulate much smaller clouds, with masses of only $10^4\,\mathrm{M_\odot}$, compared to $\sim 10^5\,\mathrm{M_\odot}$ in W17. Liow & Dobbs (2020) carry out simulations for a wide range of cloud masses, including one that is within a few percent of the W17 value, but only consider relative velocities $v_{\rm rel} \geq 20\,\mathrm{km\,s^{-1}}$, significantly higher than the case studied in W17.

3.2 Methodology

3.2.1 Numerical magnetohydrodynamics

We make use of the AREPO moving mesh code to simulate the gas dynamics and star formation of colliding GMCs (Springel, 2010b). The code solves the equations of magnetohydrodynamics (MHD) (Pakmor & Springel, 2013),

$$\frac{\partial \rho}{\partial t} + \nabla \cdot (\rho \mathbf{v}) = 0\,, \tag{3.1}$$

$$\frac{\partial \rho \mathbf{v}}{\partial t} + \nabla \cdot (\rho \mathbf{v} \otimes \mathbf{v} + p_{\rm tot} \mathbb{1} + \mathbf{B} \otimes \mathbf{B}) = -\rho \nabla \Phi\,, \tag{3.2}$$

$$\frac{\partial \rho e}{\partial t} + \nabla \cdot [\mathbf{v}(\rho e + p_{\rm tot}) - \mathbf{B}(\mathbf{v} \cdot \mathbf{B})] = \dot{Q} + \rho \frac{\partial \Phi}{\partial t}\,, \tag{3.3}$$

$$\frac{\partial \mathbf{B}}{\partial t} + \nabla \cdot (\mathbf{B} \otimes \mathbf{v} - \mathbf{v} \otimes \mathbf{B}) = 0\,, \tag{3.4}$$

where ρ, $\mathbf{v}$ and $\mathbf{B}$ are the density, velocity and magnetic field strength of a given cell. Here, $\mathbb{1}$ is the identity matrix. The total pressure is the sum of the thermal and magnetic pressures, $p_{\rm tot} = p_{\rm gas} + \frac{1}{2}|\mathbf{B}|^2$. The total energy per unit mass is $e = e_{\rm th} + \frac{1}{2}\mathbf{v}^2 + \Phi + \frac{1}{2\rho}|\mathbf{B}|^2$, where $e_{\rm th}$ is the thermal energy per unit mass. An adiabatic equation of state is adopted where $p_{\rm gas} = (\gamma - 1)\rho e_{\rm th}$ with $\gamma = 5/3$. Heating and cooling of the gas due to chemical changes and radiative processes is accounted for with the term $\dot{Q}$, which is discussed in more detail in Section 3.2.2.

The equations are solved on a tessellated Voronoi mesh in which the mesh generating points are able to follow the gas flow using a Harten-Lax-van Leer discontinuity (HLLD) solver. This allows AREPO to act as a quasi-Lagrangian MHD code. The Voronoi mesh is adaptive: cells can be refined or de-refined by adding or removing mesh-generating points, respectively. The divergence-free constraint on the magnetic field, $\nabla \cdot \mathbf{B} = 0$, is enforced by the using the MHD solver provided in AREPO (Pakmor & Springel, 2013). Here, additional source terms are added to Equations 3.2-3.4 following the scheme introduced by Powell et al. (1999) combined with a hyperbolic Dedner cleaning (Dedner et al., 2002). This minimizes any effect that a diverging magnetic field may create.

The gravitational term is due to the self-gravitation of the gas and any sink particles present within the system (see below). AREPO solves Poisson's equation,

$$\nabla^2 \Phi = 4\pi \mathrm{G} \rho\,, \tag{3.5}$$

via a tree-based algorithm similar to the one used in the GADGET-2 code (Springel, 2005b), where G is the gravitational constant. The algorithm treats each cell as if the

mass is at a point in the centre of the cell with a degree of gravity softening. The softening length for the gas is adaptive and is given as $\varepsilon_{\rm gas} = 2r_{\rm cell}$, where the $r_{\rm cell}$ is the radius of a sphere with the same volume as the Voronoi cell. The minimum softening length for both the gas and sink particles is 40.02 AU. Further information on sink particles will be discussed in Section 3.2.3.

3.2.2 Chemical network

For our simulations we make use of a modified version of the chemical network developed by Gong et al. (2017), which itself is an improved version of prior networks developed by Nelson & Langer (1999) and Glover & Clark (2012). It includes a simplified treatment of the chemistry of H, C, and O and allows us to follow the evolution of the abundances of the main low temperature gas coolants (CO, C, O, and C^+) with high accuracy, but low computational cost. A comprehensive description of the network can be found in Gong et al. (2017), and full details of the modifications we have made to it are described in Appendix A.1. Radiative heating and cooling of the gas are modelled using a detailed atomic and molecular cooling function, most recently described in Clark et al. (2019).

To treat the effects of H_2, C and CO self-shielding as well as shielding by dust, we make use of the Treecol algorithm (Clark et al., 2012). It uses information stored in the gravitational tree structure to compute a 4π steradian map of the column densities of each of these species plus dust around each Voronoi cell. These maps are then used to determine how the interstellar radiation field (ISRF) reaching the cell is attenuated by self-shielding and dust absorption.

In all of our simulations, we adopt elemental carbon and oxygen abundances given by Sembach et al. (2000). Following Draine (1978), we set the strength of the interstellar radiation field (ISRF) to $G_0 = 1.7$ in Habing (1968) units. Finally, we adopt a value of $\zeta_{\rm H} = 3 \times 10^{-17}$ s^{-1} for the cosmic ray ionisation rate of atomic hydrogen.

3.2.3 Star formation

To simulate star formation, we make use of sink particles (henceforth sinks) to represent forming star clusters (Bate et al., 1995; Federrath et al., 2010). We follow the sink creation protocol outlined in Wollenberg et al. (2020). To summarise, the following conditions must be satisfied in order for a sink to be created:

a) The cell must have a density greater than a threshold density $\rho_{\rm c} = 1.991 \times 10^{-16}$ g cm^{-3}. This threshold has been motivated by the work of Jones et al. (2023), who

demonstrate that only collapsing – and thus actively star-forming – gas can reach such densities in such a set-up. Prole et al. (2022) show that provided that the sink particles form within the collapsing regime, the star formation rate is insensitive to the exact choice of the threshold density. Note that while we could insert sink particles at lower densities, this reduces the efficiency of the algorithm, as it needs to check more candidates for sink creation. Also, this would increase the chance of converting gas to sinks, that while *currently* bound, may be subsequently disrupted via further interactions with the large-scale flows.

b) The gas flow within the accretion radius of the sink ($r_{\rm acc} = 187$ AU, corresponding to the Jeans length at the threshold density for a temperature of 10 K) must be converging. We ensure this by requiring convergence of both the velocity field ($\nabla \cdot \mathbf{v} < 0$) and the acceleration field ($\nabla \cdot \mathbf{a} < 0$).

c) The sink-forming region must be situated within a local minimum of the gravitational potential.

d) The cell must not lie within a distance $r < r_{\rm acc}$ of an existing sink particle.

e) The region within $r_{\rm acc}$ must be gravitationally bound, i.e $|E_{\rm grav}| > 2(E_{\rm therm} + E_{\rm kin})$ where $E_{\rm grav}$ is the gravitational energy, and $E_{\rm therm}$ and $E_{\rm kin}$ are the thermal and kinetic energies, respectfully.

If all of these criteria are met, the gas cell is converted into a sink that inherits its mass and momentum. This sink is able to interact gravitationally with the surrounding environment and is also able to accrete further gas onto itself. Any Voronoi cells with $\rho > \rho_{\rm c}$ within a distance $r < r_{\rm acc}$ of a sink are potentially eligible for accretion. However, gas is only accreted from the cell if it is gravitationally bound to the sink. Provided this is the case, enough gas is removed from the cell to reduce its density to $\rho_{\rm c}$, although the total amount removed at each time-step is capped at 90% of the cell's initial mass, for reasons of numerical stability. Following the accretion, any properties of the cell that depend on its mass are updated. It should be noted that the sinks formed do not contribute to the magnetic field of the system (i.e $|B_{\rm sink}| = 0$). Given the size of our sink particles, and the density at which they are introduced, it is clear that they cannot be interpreted as individual stars, but rather as small-N protostellar systems. Also, given that there is no feedback from the young stars in our cloud, any star formation efficiencies reported in this chapter should be considered as upper limits – our sink particles record the mass that is capable of going into stars (i.e., trapped in potential wells), in accordance with the above star formation model.

3.2.4 Initial conditions

In this chapter we adopt the initial conditions provided in W17, which were motivated by observations of GMCs. The simulations are initialised within a (128 pc)^3 domain of molecular gas with a mean molecular weight $\mu = 2.33$ and a helium to hydrogen fraction of 0.1. Two spherical clouds of radius $R_{\rm GMC} = 20$ pc are placed into the domain with their centres separated by $(x, y, z) = (2R_{\rm GMC}, b, 0)$ where $b = 0.5R_{\rm GMC}$ (see Figure 3.1). Each cloud is initialised with a mass of $M_{\rm GMC} = 9.3 \times 10^4$ M$_\odot$ and an initial temperature of 15 K by randomly distributing 2 million mesh generating points uniformly which constructs our initial cells, achieving an initial mass resolution of 0.0465 M$_\odot$. This results in a hydrogen nucleon density of $n = 80.2$ cm^{-3} within the clouds where $n = \frac{\rho}{(1+4A_{\rm He})m_{\rm p}}$ with $A_{\rm He} = 0.1$ being the helium to hydrogen fraction and $m_{\rm p}$ being the mass of a proton. Surrounding the clouds is a region of warmer molecular gas with $n = 7.14$ cm^{-3} and a temperature of T=150 K. The clouds are not initially in thermal pressure equilibrium with the surrounding material. However, with an initial thermal to gravitational energy ratio of$E_{\rm therm}/E_{\rm grav} = 0.0066$, the clouds are significantly gravitationally bound against thermal pressure, and hence any loss of mass into the low density surrounding medium is small.

A uniform magnetic field of $|B| = 10$ μG in magnitude is set across the whole domain of the simulation. This results in an Alfvén velocity of $v_{\rm A} = 2.06$ km s^{-1} for each cloud and a mass-to-flux ratio that is 6 times greater than the critical value for both clouds (Glassgold & Langer, 1974), making them magnetically supercritical. The angle θ is the magnetic field inclination from the x-axis in the x-y plane and is varied between simulations to investigate whether the orientation of the magnetic field affects the star formation rate. (see Table 3.1).

We give the two clouds initial velocities of $v = +v_{\rm rel}/2$ and $v = -v_{\rm rel}/2$ for the clouds starting at negative and positive x, respectively, so that they will later collide at a relative velocity $v = v_{\rm rel}$. We carry out simulations with a range of different $v_{\rm rel}$, so that we can investigate how different collision strengths impact the star formation rate. We also include one case where $v_{\rm rel} = 0$ km s^{-1} (simulation 2), to allow us to investigate what happens in the absence of a collision.[3] Full details of the velocities used can be found in Table 3.1. Along with the collisional velocity, a turbulent velocity field is also applied to each cloud. The turbulence applied is purely solenoidal and has a 3D velocity dispersion of $\sigma = 3.46$ km s^{-1}. This follows a scaling law of $P(k) \propto k^{-4}$.

[3]Note that even in this case, the clouds will eventually collide due to their mutual gravitational attraction. However, this will occur on a timescale > 10 Myr, much longer than the period simulated here.

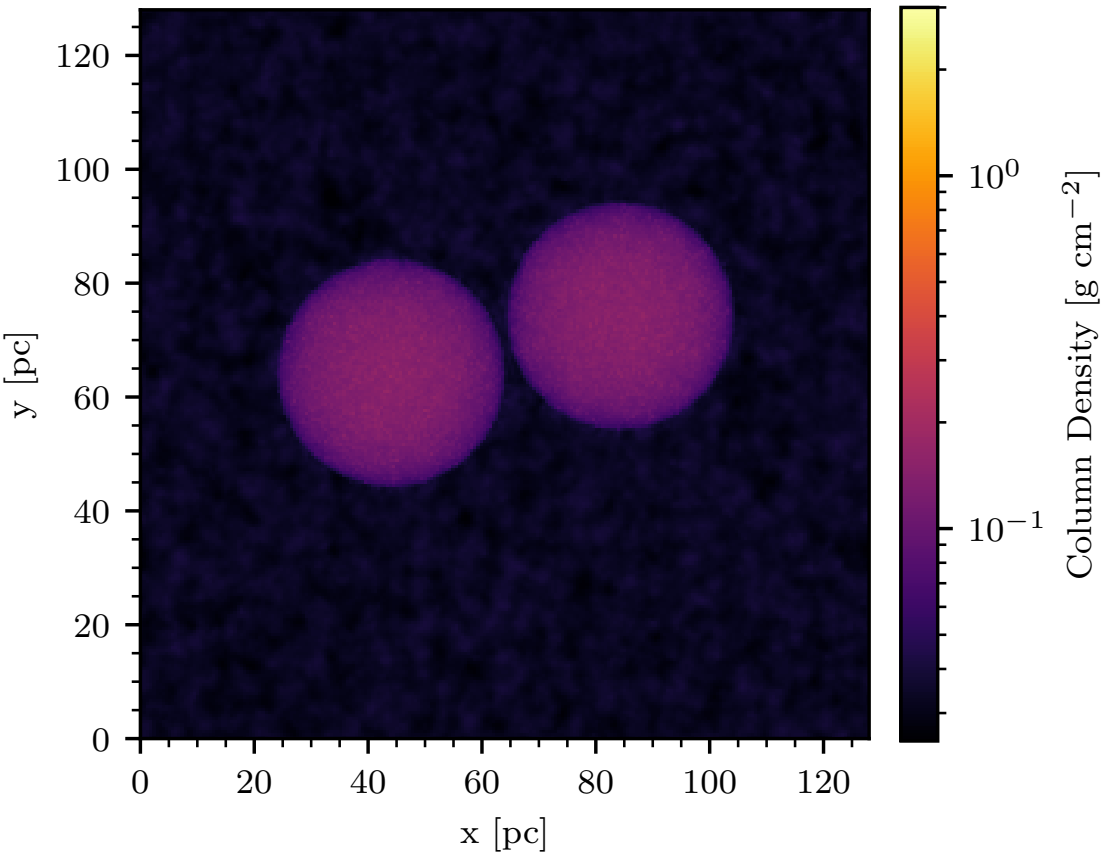

Figure 3.1. Surface density plot of the initial positions of the clouds.

Table 3.1. Initial conditions that are altered between simulations.

Simulation	θ (°)	$v_{\rm rel}$ (km s^{-1})	Cells per Jeans length
1	60	10	8
2	60	0	8
3	60	5	8
4	60	15	8
5	0	10	8
6	30	10	8
7	90	10	8
8	60	10	4
9	60	10	16

For the velocity field within each cloud the turbulence induced is both supersonic and super-Alfvénic, where $\mathcal{M} = \sigma/c_{\rm s} = 11.6$ and $\mathcal{M}_{\rm A} = \sigma/v_{\rm A} = 1.68$ respectively. The turbulence induced allows for each cloud to be in virial equilibrium, with the kinematic to gravitational energy ratio for each cloud being $E_{\rm kin}/E_{\rm grav} = 0.499$.

We also investigate the effect of varying the number of cells per local Jeans length (hereafter referred to as the Jeans refinement parameter, JR). To do this we adopt Jeans refinement as our main cell refinement criterion in AREPO. Cells are refined by adding additional mesh generating points whenever $D > \lambda_{\rm J}/{\rm JR}$, where D is the effective diameter of the cell (i.e. the diameter of a sphere with the same volume as the mesh cell). We adopt ${\rm JR} = 8$ as our default value for the Jeans parameter, but also investigate the behaviour of runs with ${\rm JR} = 4$ and ${\rm JR} = 16$, as detailed in Table 3.1.

We run the simulations as far as practical to establish a trend in the star formation history. The end time varies due to the adaptive timestep of the simulation, between 3 and 4 Myr. In the presence of close interacting objects, such as binaries, the timestep reduces significantly thus slowing the simulations progression.

3.3 Results

3.3.1 Star formation rate

Each simulation results in a different star formation history. For an example, in Figure 3.2 it can be seen that the systems evolve differently, creating unique structures. As a result, varying numbers of sink particles form in the simulations, as shown by the

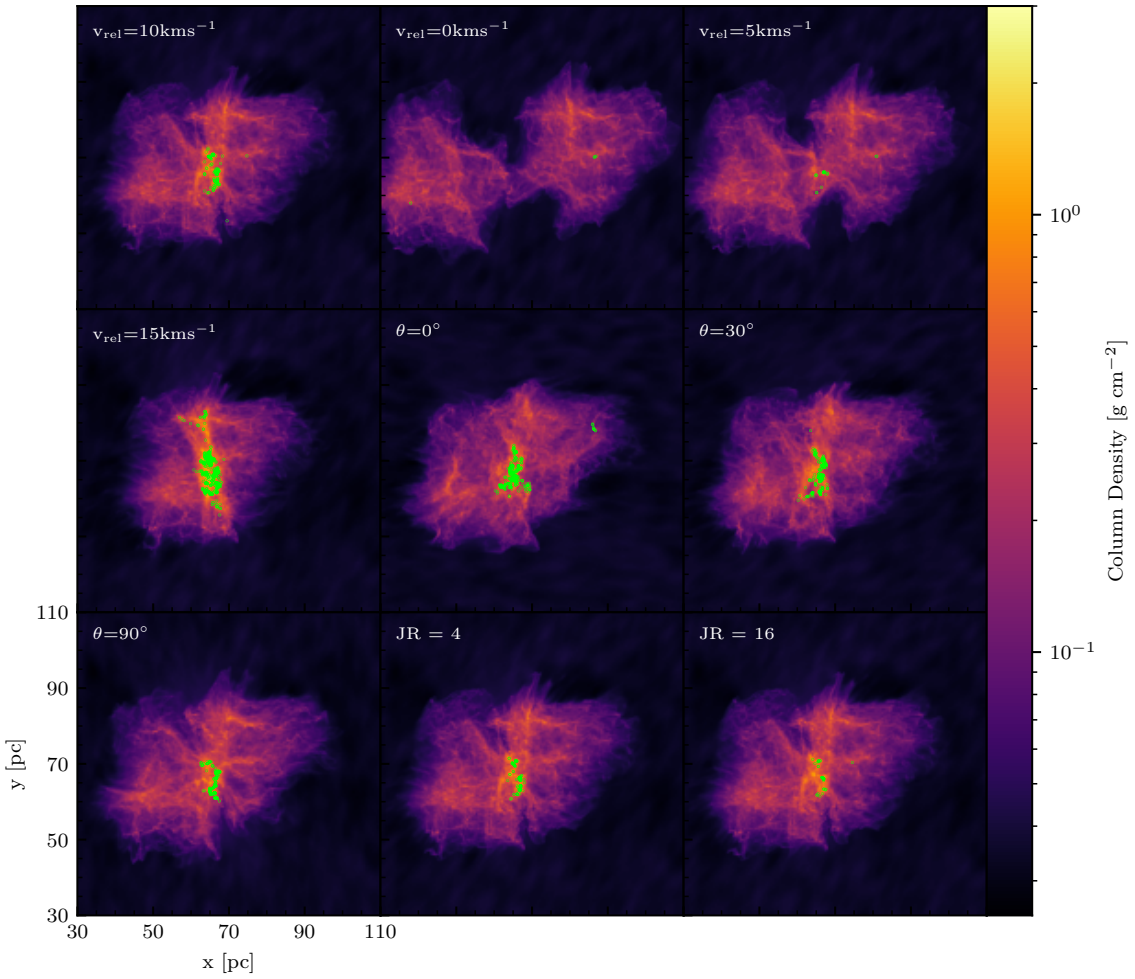

Figure 3.2. Column density plots of all simulations at $t = 2.40$ Myr. The green dots within the plot represent the sink particles that have formed.

green dots in Figure 3.2. To investigate this difference quantitatively, we look at the star formation rate of each of the simulations.

The star formation rate is calculated as:

$$\dot{M}_{\rm SFR} = \frac{\Delta M}{\Delta t} \tag{3.6}$$

where ΔM is the difference in the mass of the sinks between the start and end of a time step of length Δt. These are calculated for each output snapshot available in all nine simulations. The results from these calculations are presented in Figure 3.3 along with the total mass that has gone into star particles.

Figure 3.3 shows that there is a clear difference in the time taken for stars to begin forming in the different runs, with a spread in onset times of ~ 0.7 Myr between the most extreme cases. Looking in more detail at the results from the individual runs, we see that changing the collisional velocity has the greatest impact on the time required for star formation to begin. Stars start to form sooner in simulations with high collisional

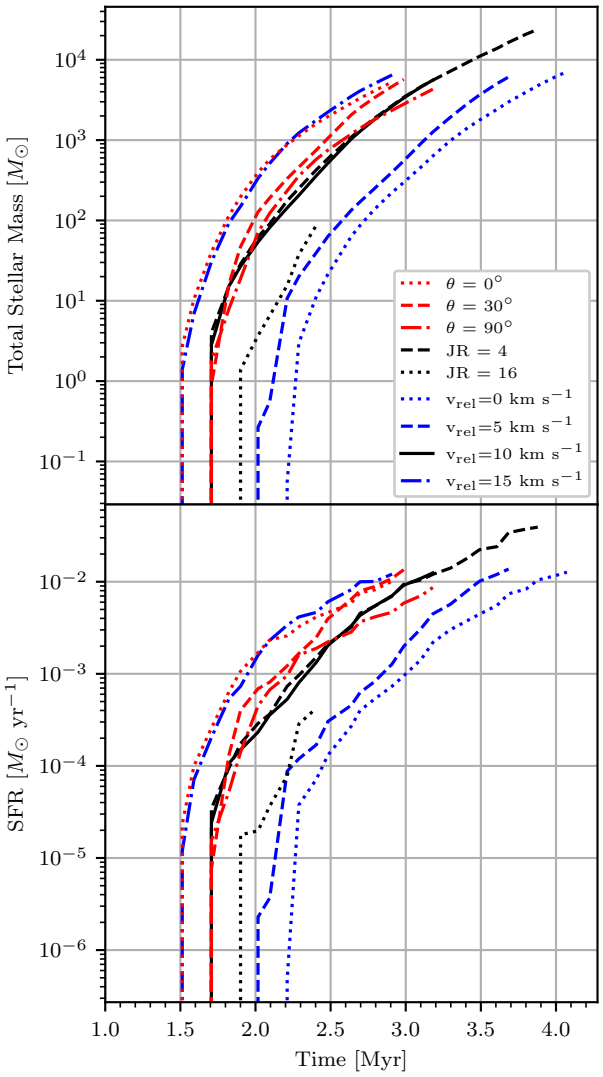

Figure 3.3. *Top*: Evolution of the mass in sink particles as a function of time in all nine simulations. *Bottom*: Star formation rate as a function of time in all nine simulations.

velocity than in simulations with low or zero collisional velocity. This behaviour is likely due both to the time it takes for large-scale shocks to form in the colliding clouds, and also to the density enhancement produced by these shocks. Faster collisions produce stronger shocks and hence larger density enhancements.[4] Therefore, higher density star-forming regions with shorter free-fall times are formed with increased collision velocity.

The orientation of the magnetic field has a smaller effect on the time required for star formation to begin. We see a clear difference in behaviour between the case with the magnetic field orientated parallel to the collisional axis, which forms stars after ~ 1.5 Myr, and the runs with other magnetic field orientations, in which the onset of star formation is delayed by ~ 0.25 Myr. The earlier star formation observed when the magnetic field is parallel to the collisional axis is a result of the magnetic field not hindering the compression of the gas along the x-axis. This allows the shocked gas to reach the densities required for the first sinks to be created more rapidly compared to the other magnetic field orientations (see also Appendix A.2). This delayed behaviour agrees well with that of the strong B_y simulation of Dobbs & Wurster (2021).

Finally, regarding the Jeans refinement variation, a higher resolution tends to delay the onset of star formation. This is likely due to the more highly resolved turbulent velocity field resulting in more disruption of the star-forming gas. This results in the gas being unable to be fully bound, delaying star formation. However, it should be noted that the difference of the onset of star formation between the $JR = 8$ and $JR = 16$ cases is small, of the order of ~ 0.2 Myr, which is about the free-fall time of a dense core.

It is also informative to look at how the dense gas fraction – defined here as the fraction of the gas above a density of 10^4 cm^{-3} with common observational definitions (e.g. Lada et al., 2010) – varies as a function of time in the different simulations. We illustrate this in the bottom three panels of Figure 3.4 and as expected, dense gas is produced more rapidly as we increase the collision velocity, confirming our suspicion that the differences we observe in the timing of the onset of star formation are largely due to the differing amount of time it takes to compress the gas. Changing the orientation of the magnetic field also changes the dense gas fraction, with an appreciably higher fraction produced when the magnetic field is aligned with the axis of the collision. It is also apparent that there is an offset of around 0.5–1.0 Myr between the time taken to produce dense gas at $10^4\,\mathrm{cm}^{-3}$ and the onset of star formation. The offset reduces when

[4] Recall that for an isothermal shock, the strength of the density enhancement scales as the square of the Mach number. Although our model GMCs are not isothermal, the equilibrium temperature of the molecular gas varies only weakly with temperature, and so the isothermal result remains a useful guide.

we consider higher density gas fractions. This offset is easily understood as a consequence of our definition of "dense" gas, and the fact that the density threshold for sink particle creation is significantly higher than the value we use in our definition of dense gas. At $n = 10^4\,\mathrm{cm}^{-3}$, the gravitational free-fall time of the gas is ~ 0.5 Myr, and so we would expect gas close to this density to require around this long to collapse to stellar densities (in reality) or the sink creation density (in the simulations).[5] The offset we see between the appearance of "dense" gas and the formation of stars therefore corresponds to the one to two free-fall times required for gas at this density to collapse sufficiently to form stars.[6]

From Figure 3.4 we observe significant variation of the gas fractions at early timesteps prior to the steady evolution of the gas density. Most of these variations are transient features in which denser gas forms due to the collision but is dispersed due to pressure gradients briefly forming. For the two lower density thresholds, we also see that there is a small fraction of gas above the threshold present at the beginning of the simulation. This results from the uneven distribution of mesh points within the initial conditions, which results in a certain amount of scatter in the starting densities of the cells.

The role of the collisions in driving the increase in the dense gas fraction and bringing about the onset of star formation can also be seen clearly if we examine how the dense gas fraction varies as a function of cloud separation, defined as the distance between the centres of mass of the two clouds. We see that most of the simulated clouds follow very similar tracks in this diagram, with substantial quantities of dense gas becoming apparent only once the cloud separation is less than $\sim$ 25 pc, i.e. once the collision is significantly advanced. The two exceptions are the clouds with $v_{\mathrm{rel}} = 0$ and 5 km s^{-1}, which start to develop dense gas while at clearly larger separations, particularly in the $v_{\mathrm{rel}} = 0\,\mathrm{km\,s}^{-1}$ run. These two runs are also the ones that produce the lowest dense gas fractions at any given time and that form the least number of stars. Our results are therefore consistent with the idea that in these runs, star formation is driven primarily by the collapse of the individual clouds, with the interaction between them playing little role, while in the simulations with higher v_{rel}, the collision between the clouds plays a much more substantial role in influencing the star formation rate.

[5] Note that in a pure free-fall collapse, the time taken to collapse from 10^4 cm^{-3} to our sink creation density of $\sim 10^8$ cm^{-3} is two orders of magnitude longer than the time taken from collapse from $\sim 10^8$ cm^{-3} to stellar densities.

[6] In the absence of pressure, we would expect the gas to collapse within a single free-fall time. In reality, however, the non-negligible magnetic pressure and kinematics of the gas inevitably delays the collapse (See Sect. 3.3.2). Finally, even once we account for this offset, it is clear that not all of the dense gas that forms in the simulations goes on to form stars. Instead, the star formation efficiency in gas of this density is typically only a few tens of percent.

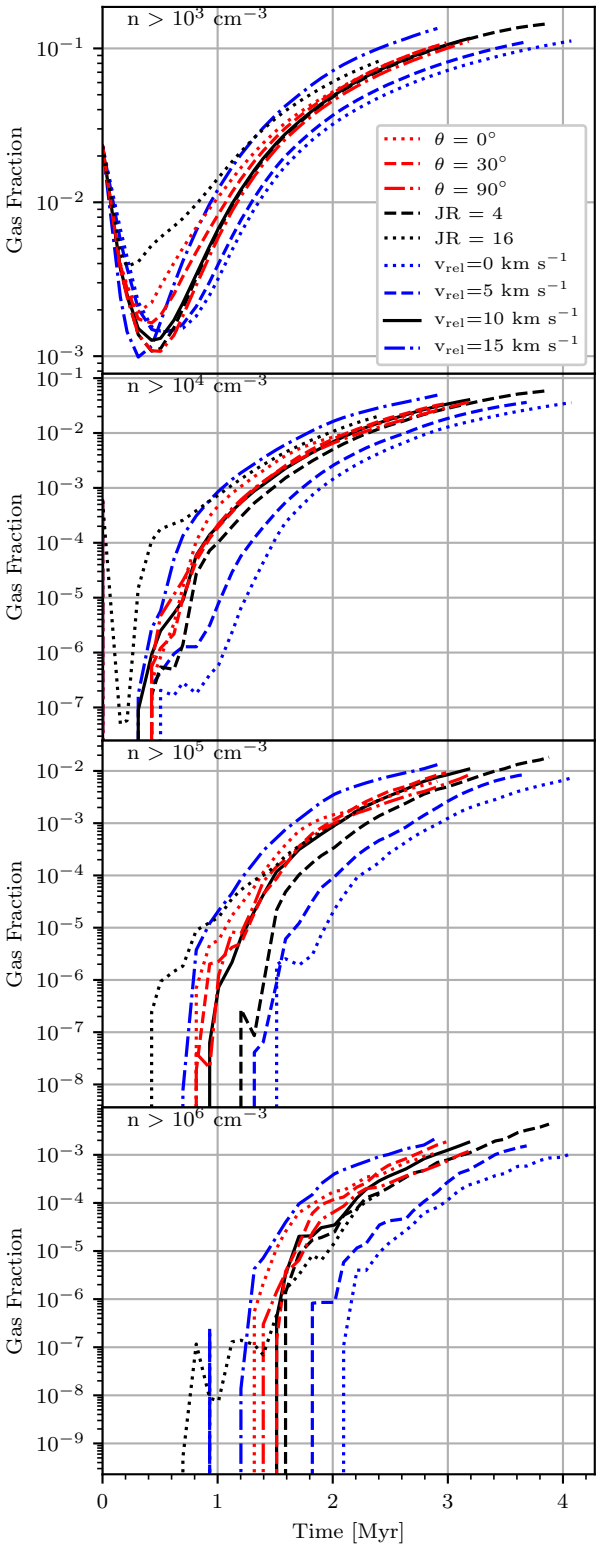

Figure 3.4. Fraction of gas above the specified density threshold in all nine simulations, plotted as a function of time. The thresholds are indicated in the top-left corner of each panel and are $n > 10^3\,\mathrm{cm}^{-3}$, $10^4\,\mathrm{cm}^{-3}$, $10^5\,\mathrm{cm}^{-3}$ and $10^6\,\mathrm{cm}^{-3}$ from *top* to *bottom*. We see that increasing the collisional velocity increases the amount of gas above the threshold for all values of the threshold, but that the effect is much stronger for the higher density thresholds.

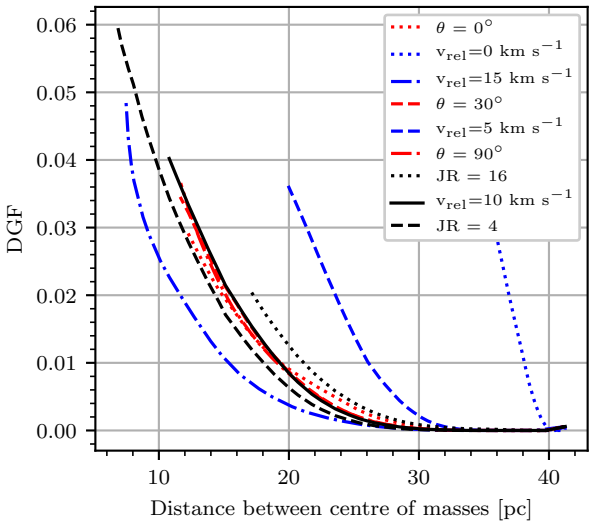

Figure 3.5. Fraction of dense ($n > 10^4$ cm^{-3}) gas in all nine simulations, plotted as a function of the separation between the clouds' centre of masses

.

Figure 3.6 shows that the star formation rate in each simulation follows a similar trend from the point when sinks first form. For a brief period after the first sinks form, the SFR in the runs with $v_{\rm rel} > 0$ km s^{-1} is as much as an order of magnitude larger than in the run with $v_{\rm rel} = 0$ km s^{-1}, in which the clouds do not collide. However, the difference between the runs quickly decreases, and for the majority of the time covered by our simulations, the SFR in the cloud collision runs is only a factor of 2–3 larger than in the zero velocity run. This behaviour agrees well with the enhancement in the star formation rate found by Liow & Dobbs (2020) and Tanvir & Dale (2020) for collision velocities below 20 km s^{-1}. However, it is substantially smaller than the order of magnitude increase found by W17 despite the similarity between our initial conditions and theirs. To help us better understand the origin of this difference in results, we look in the next section at the virial parameter of the clouds and clumps formed in the simulations.

3.3.2 Impact on the virial parameter

In the previous section, we showed that although the cloud collision increases the star formation rate of our colliding clouds compared to the case with no collision, the magnitude of the increase is much smaller than the order of magnitude found by W17. This difference in outcome from their simulations cannot be a consequence of the initial conditions, as we use the same initial conditions as in their study, and hence must be a consequence of the difference in numerical approaches. As we discuss in more

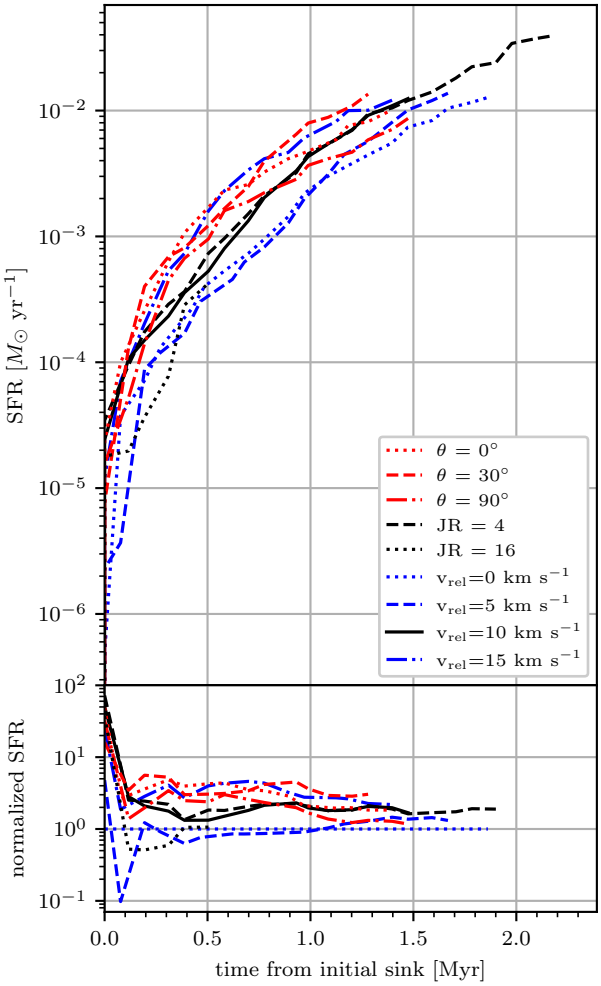

Figure 3.6. *Top*: Star formation rate varying with time from initial sink formation for all simulations. *Bottom*: Star formation rate normalised to $v_{\rm rel} = 0$ km s^{-1} star formation rate as a function of time from initial sink formation.

detail in Section 3.4, one of the main differences between our two studies is the algorithm we use to identify star-forming gas. W17 form stars stochastically in gas above a fixed density threshold, with no consideration given to whether or not the gas is gravitationally bound, whereas we use a sink particle based approach in which stars form only in regions that are verifiably bound and collapsing. To understand whether this algorithmic difference can explain the difference in outcome, we explore how the virial parameter of the gas varies on different scales within our set of simulations.

The virial parameter η provides an insight into how bound the star-forming region is by comparing the gravitational energy against all other energy contributions. We adapt the definition provided in Bertelli Motta et al. (2016) to include magnetic energy as a factor which counteracts gravitational collapse (Eqn. 3.7).

$$\eta = \frac{2(E_{\rm kin} + E_{\rm therm} + E_{\rm mag})}{|E_{\rm grav}|} \tag{3.7}$$

We chose to include the magnetic energy in this calculation as the gas we are considering has a density below the sink formation threshold and does not exist near sinks. It should be noted that the magnetic energy is not accounted for in the energy check of the sink creation protocol.[7]

In order to make the comparison between the simulations we perform this analysis on the snapshots that are $\sim$1 Myr after the formation of the first sink particle in each simulation. Note that this corresponds to a different physical time in each simulation, but should allow us to compare the clouds when they are at a similar stage in their evolution.

The regions used to determine the virial ratio are chosen by using the local minima of the potential. These are identified as part of the flux calculations within the MHD code and are stored within the outputs. After identification, we then compute the Jeans length for the gas located at the potential minimum. For the purposes of this analysis, we want to avoid potential minima that have already formed stars, so that we can measure the virial ratio accurately without worrying about the confounding effect of the sink particles.[8] We therefore remove from consideration any minima that are located within two Jeans lengths of a sink particle. We next select all gas cells lying within a single Jeans length of the identified minimum and compute the total gravitational, kinetic, magnetic and thermal energies of this set of gas cells. The gravitational energy, $E_{\rm grav}$, is calculated

[7] In cases where the magnetic energy is high enough in the sink formation region to prevent collapse, we would also expect it to halt the infall of the gas, i.e. independent of the energy check, the region will fail condition (b) of the sink creation protocol and hence will not be converted into a sink.

[8] As sink particles selectively remove the most bound gas, the virial ratio in the remaining gas will inevitably be higher than it would be in the same region if the sink were not present.

via a direct N-body approach,

$$E_{\rm grav} = -\sum_{i=1}^{N}\sum_{j=i+1}^{N}\frac{Gm_i m_j}{\Delta r_{ij}} \tag{3.8}$$

where m_i and m_j are the masses of the ith and jth cells, respectively, Δr_{ij} is the separation between the cells and N is the total number of cells within the selected region. The kinetic, magnetic and thermal energies, $E_{\rm kin}$, $E_{\rm mag}$ and $E_{\rm therm}$, are calculated as follows:

$$E_{\rm kin} = \frac{1}{2}\sum_{i=1}^{N} m_i v_i^2 \,, \tag{3.9}$$

$$E_{\rm mag} = \frac{1}{8\pi}\sum_{i} |B_i|^2 \Delta V_i \,, \tag{3.10}$$

$$E_{\rm therm} = \sum_{i} m_i e_{{\rm th}_i} \,, \tag{3.11}$$

where m_i is the mass of cell i, v_i is the velocity of the cell relative to the potential minimum considered, $|B_i|$ is the magnetic field strength of the cell, $\Delta V_i = m_i/\rho_i$ is the approximate cell volume where ρ_i is the cell density, and $e_{{\rm th}_i}$ is the thermal energy per unit mass of the cell.

The number densities associated with the local minima of the potential cover a wide range of values. For the purpose of this analysis we focus on a range of associated hydrogen nuclei number densities from $n = 100$ cm^{-3} to 10^6 cm^{-3}. Our motivation for adopting a lower limit of 100 cm^{-3} is to ensure that are selecting regions associated with the cloud and not the surrounding inter-cloud medium. The upper limit is chosen to match the density threshold for star formation used in W17. We split the data into four bins of 1 dex in density starting at 10^2-10^3 cm^{-3}.

In Figure 3.7, we show the ratio of each of the different components of the energy (thermal, magnetic, kinetic) to the gravitational energy as well as the averaged virial parameter for the hydrogen nuclei number density n bin considered for varying collisional velocity. The error bars indicate the full range of values of each parameter in each bin, i.e. the range from the minimum to the maximum value of the parameter.

Upon first inspection we note that the virial parameter is considerably greater than 1 in almost all of the regions we consider. This would imply that they are not gravitationally bound and thus unable to form stars at this point as a result. While this is likely true for some regions, particularly in our lower density bins, it should also be noted that we are considering only a single Jeans length from the potential minimum, and therefore we would expect to recover $\eta \sim 1$ for this region even if the kinetic and magnetic energies were zero.[9] Since these components are not zero, it is unsurprising

[9]We do not recover exactly one because the density and temperature are not constant within the selected region.

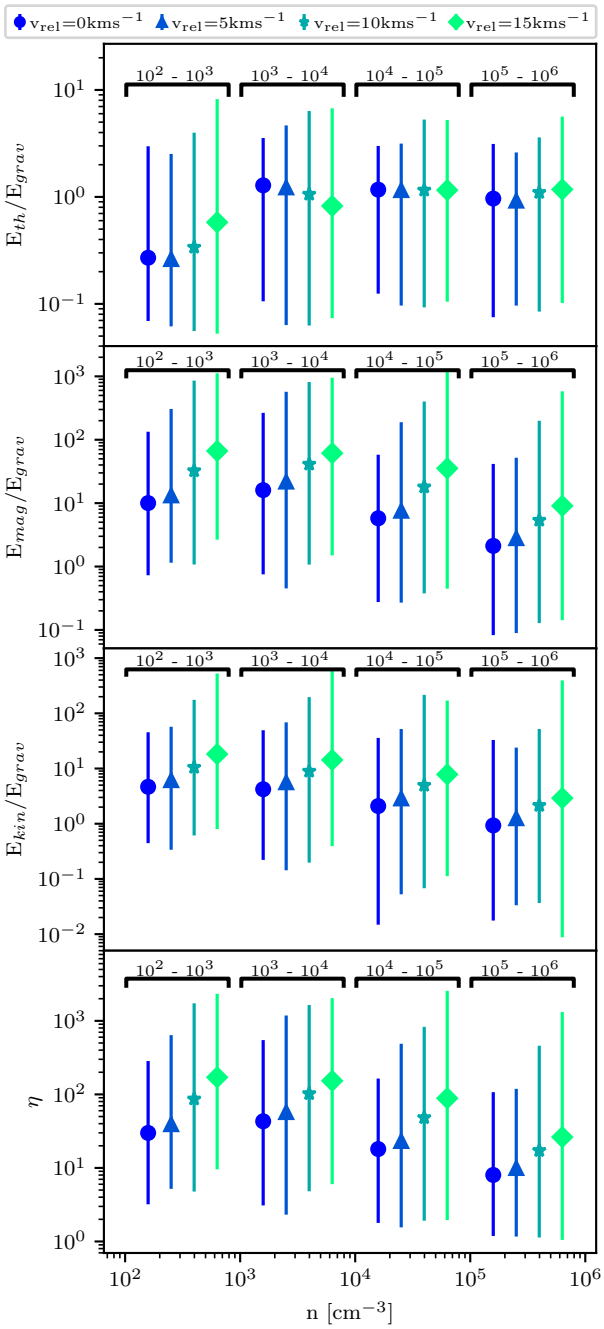

Figure 3.7. From the top down: The average a) thermal to gravitational energy ratio, b) magnetic to gravitational energy ratio, c) kinetic to gravitational energy ratio, and d) virial parameter for different collisional velocities v_{rel} at 1 Myr after first sink formation. The error bars indicate the full range of values obtained. Each density bin is indicated with the corresponding bracket annotation with the separation of the points for ease of reading. The points within a bracket are for the same density bin but are offset in the figure for clarity.

that we recover $\eta \gg 1$ for most of these regions, even the ones that will later form stars. In practice, all that this means is that the radius of the region that will ultimately collapse is greater than a single Jeans length, owing to the additional support provided by the turbulent motions and the magnetic field. Nevertheless, this does provide a clear demonstration of the difficulties involved in identifying star-forming regions based on the properties of individual gas cells, as is the case when applying for example a simple density threshold, since ultimately the answer to the question of whether or not this gas will collapse and form stars depends not only on its own properties but also those of the surrounding gas cells.

For the purposes of the comparison we are making here, we look for differences in the parameters between the simulations considered, and in particular for any general trends. For the ratio of $E_{\rm therm}$ to $E_{\rm grav}$, we do not see a clear trend with collision velocity: the ratio increases with increasing $v_{\rm rel}$ in some density bins, but decreases or remains constant in other density bins. However, we observe a consistent increase in the ratios of $E_{\rm mag}$ to $E_{\rm grav}$ and $E_{\rm kin}$ to $E_{\rm grav}$ with increasing $v_{\rm rel}$ in all density bins. This is then reflected in the behaviour of the virial parameter, which also increases with increasing $v_{\rm rel}$ at all densities. This behaviour is a consequence of an increase in the turbulent motion of the dense molecular gas as the clouds collide with higher velocities. This directly increases the kinetic energy, but also results in additional tangling of the magnetic field, which increases the magnetic field strength and magnetic energy. These motions generally act against gravitational collapse and as a result fewer regions become gravitationally bound and star-forming, leading to a smaller increase in SFR than anticipated by W17.

We have repeated the same analysis for the simulations with differing initial magnetic field inclinations (Fig. 3.8). Once again, we find that the ratio of $E_{\rm therm}$ to $E_{\rm grav}$ is substantially less than one in our lowest density bin and of order unity in the other bins. In the lowest density bin, we also observe a decrease in the average value of this ratio with increasing inclination angle. A reason for this could be that the gravitational energy calculated for these densities in the $\theta = 0^\circ$ simulation is higher due to compactness. The regions considered for this density bin exist on the outer parts of the clouds and visual inspection of the density maps shows more 'flaring' at the edges for greater magnetic field inclinations than for $\theta = 0^\circ$ (see also Figures A.1 and A.2). We see no clear trend in the value of the ratio with magnetic field inclination angle in the other density bins. As for the magnetic and kinetic to gravitational energy ratios, we find the values of these ratios to be similar across the different inclinations within a given density bin. This in turn results in the virial ratio being constant across all magnetic field orientations for each density bin.

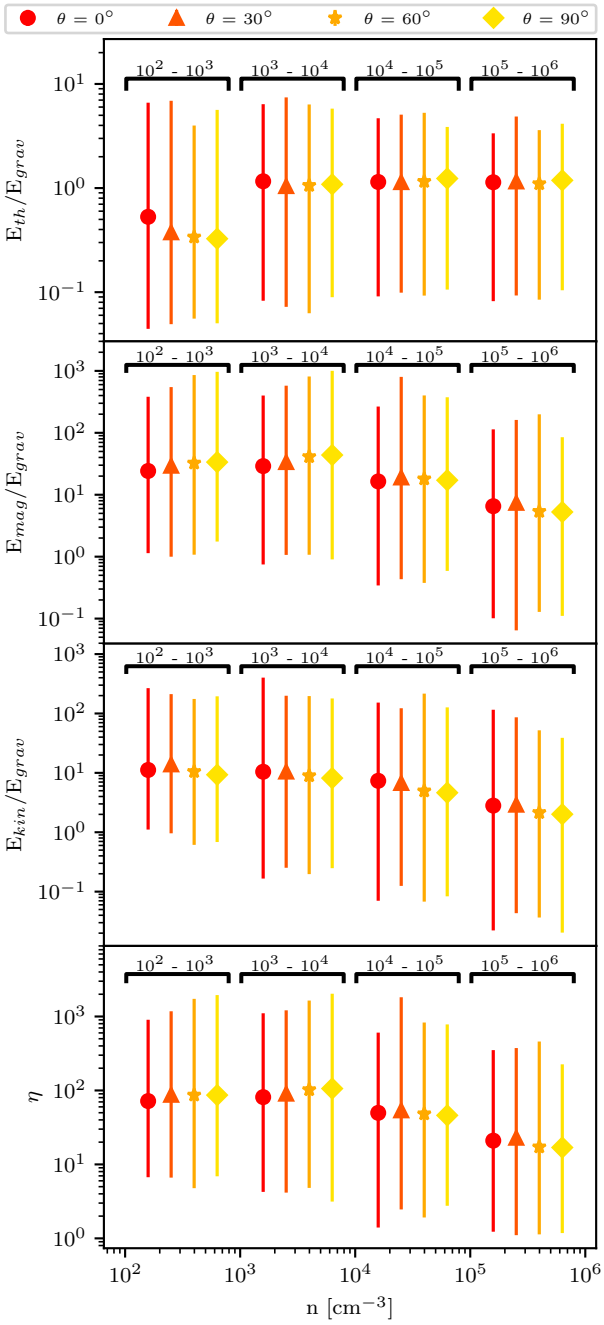

Figure 3.8. Same as Figure 3.7 but looking at the differences in the inclination of magnetic field

3.3.3 Flow alignment to magnetic field

The movement of gas within a magnetic field causes that field to be dragged, distorting the magnetic field in the process. The compression of the field lines causes the flow of gas to slow down as the magnetic field resists the flow. However, this only applies if the direction of flow is not parallel to the magnetic field. The flow remains unhindered if it is parallel to the magnetic field. Examining the alignment between the flow and the magnetic field can therefore tell us something about the degree to which the field is influencing the motion of the gas.

For this purpose, we define the alignment as the dot product of the velocity and magnetic fields normalized by the magnitude of the fields, in other words:

$$\text{Alignment} = \frac{\mathbf{v} \cdot \mathbf{B}}{|\mathbf{v}||\mathbf{B}|} \tag{3.12}$$

This yields the cosine of the angle between the magnetic field and the flow velocity for each Voronoi cell, which has values ranging from -1 to 1, with the extremes meaning the fields are parallel whilst a value of 0 means the fields are perpendicular. This corresponds to unrestricted and fully restricted flow by the magnetic fields, respectively. In Figures 3.9 & 3.10, we explore how the field alignment varies between our four density bins in runs with different relative velocities and magnetic field inclinations. In each case, the count of the points at each alignment is normalized by the total number of points within the relevant density bin. The analysis is carried out using the same snapshots as in Section 3.3.2.

In low density regions ($10^2 - 10^4$ cm^{-3}), we find a distribution of alignments similar to what we would expect for a fully random distribution (indicated in Figures 3.9 & 3.10 by the black dashed line). In the highest collision velocity runs ($v_{\rm rel} \geq 10$ km s^{-1}), there is a slight skew in the distribution of alignments that we have traced to a similar skewness in the distribution of alignments in the initial conditions (See Fig. 3.11). Similarly, in the runs with $\theta = 0°$ and $\theta = 90°$, we also see a clear imprint of the initial conditions, with a preference for parallel alignments in the run with $\theta = 0°$ and for perpendicular alignments in the run with $\theta = 90°$. Overall, there is little indication that the field plays a significant dynamical role in the low density gas.

At higher gas densities ($10^4 - 10^6$ cm^{-3}), we no longer see any clear imprint of the initial conditions. The distribution of alignments close to 0.0 becomes very similar to what we would expect for a fully random distribution. However, there is a clear deficit of alignments close to -1 and $+1$ that becomes more pronounced as the density increases. In other words, in dense gas, the gas flow is predominantly perpendicular to the field, rather than parallel to it. This behaviour is consistent with our expectations for magnetically supercritical gas: the flow of gas perpendicular to the magnetic

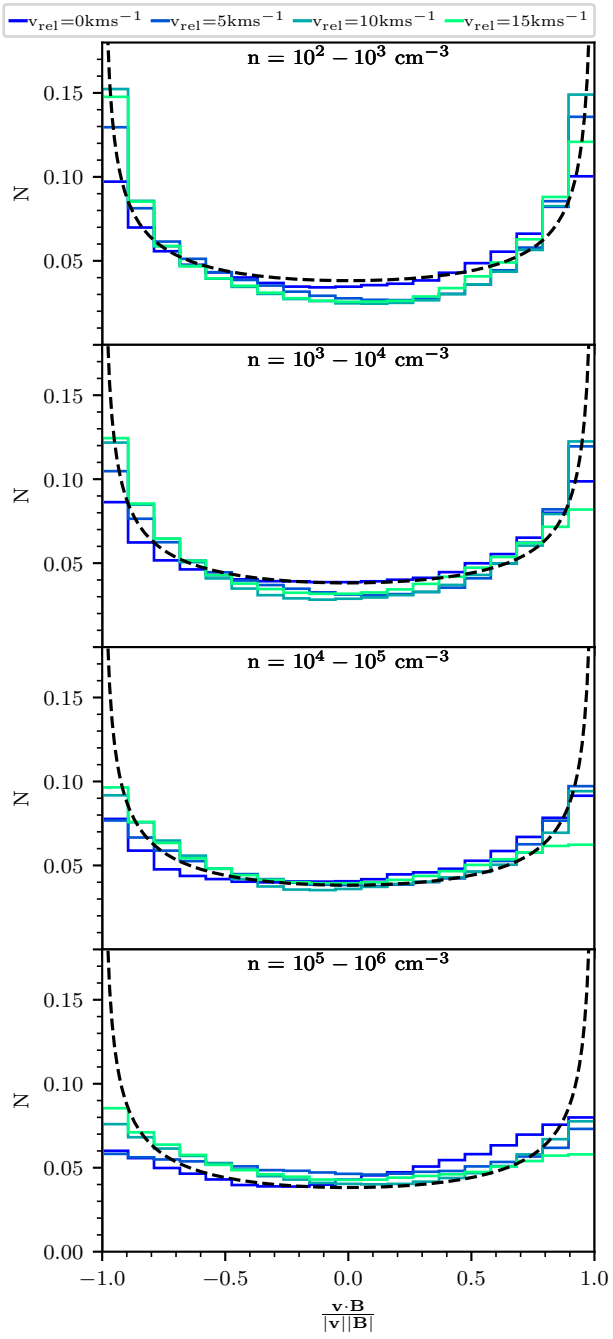

Figure 3.9. Weighted histogram of the velocity and magnetic field alignment for differing collisional velocities at 1 Myr after first sink formation. Each subplot represents a different density bin. The black dashed line represents the distribution we would expect if the alignment is random.

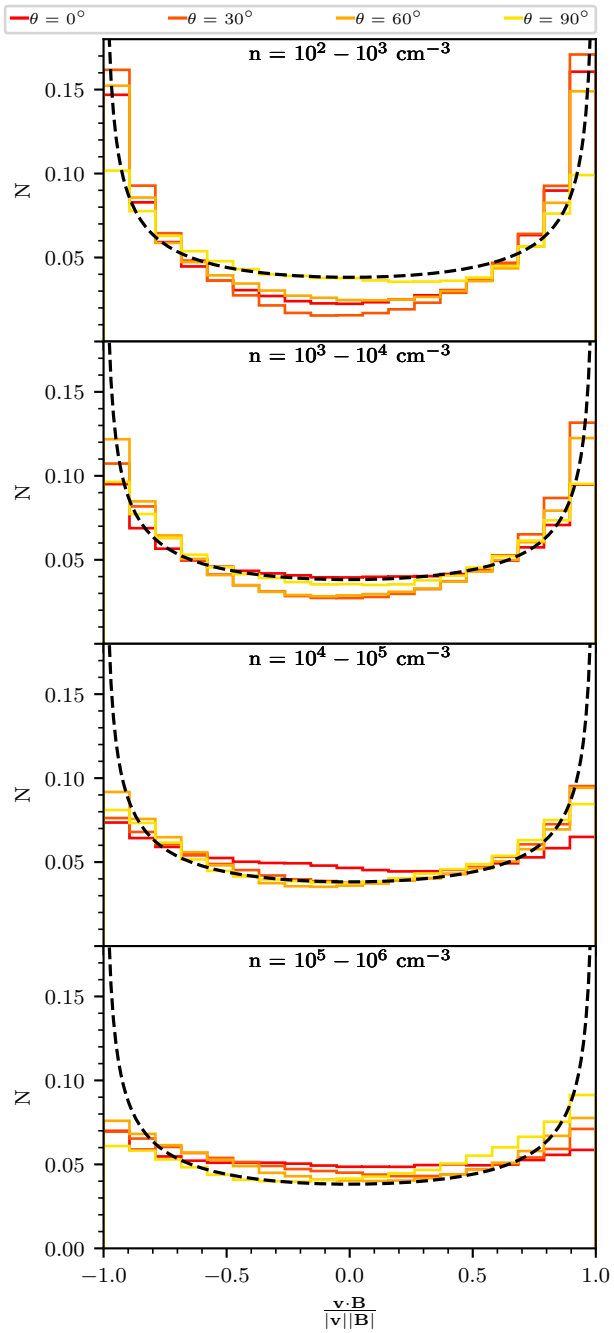

Figure 3.10. Same as Figure 3.9 but for varying magnetic field inclination.

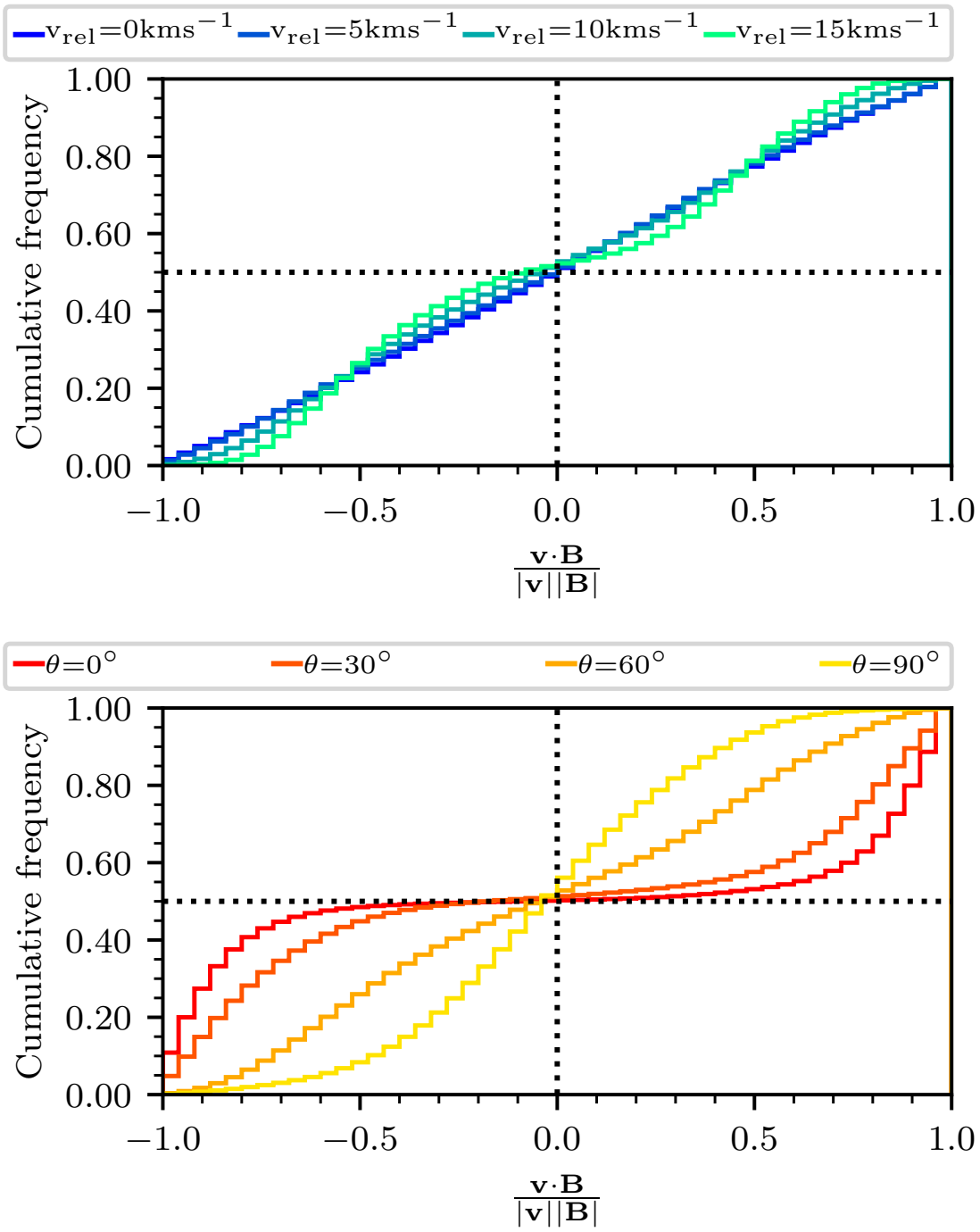

Figure 3.11. Cumulative distribution of the initial alignment of the simulations at $t = 0$ Myr. *Top*: Varying collisional velocity. *Bottom*: Varying magnetic field inclination. The dashed black lines represent where the cumulative distribution would encompass 50% of the data assuming a Gaussian distribution of alignments. Points in the top-left and bottom-right quadrants are indicative of a skewed distribution.

field compresses and strengthens the field, while the flow of gas along the field lines leaves the field strength unaltered, resulting in a field alignment that becomes increasingly perpendicular as the compression continues. This behaviour has been seen in other simulations (such as Soler & Hennebelle, 2017) and is a result of velocity field convergence, $\nabla \cdot v < 0$ (Boldyrev, 2006; Matthaeus et al., 2008).

One further important take away from these results is that in the densest gas, there are only minor differences in the field alignment between the different runs, consistent with a picture in which the small-scale behaviour of the field in dense regions is primarily determined by the local velocity field and not by the large-scale details of the collision.

3.4 Discussion

3.4.1 Comparison with W17

Our simulations demonstrate that rapid collisions between clouds lead to an earlier onset of star formation than in clouds that collide slowly or not at all. However, the way in which star formation proceeds once the process has set in is remarkably similar in all of our simulations. Note we find a persistent enhancement of a factor of 2–3 in the star formation rate in our colliding clouds compared to our $v_{\rm rel} = 0$ km s^{-1} control run. The earlier onset of star formation and the increase in the star formation rate due to the collision are similar to the results reported by W17 for the same initial conditions. Contrary to W17, we find a only a very weak dependence of the SFR on the collisional velocity, $v_{\rm rel}$.

It is worthwhile considering possible methodological reasons for this difference. Aside from our use of a different magnetohydrodynamical code (Wu et al. use Enzo, we use Arepo), our simulations differ from those of W17 in two main respects: our star formation algorithm and our treatment of chemistry and cooling.

Star formation protocol

In our simulations we make use of sink particles as our representation of stars/protostellar systems, which are able to continue accreting after forming (see Sect 3.2.3). In contrast, W17 make use of star particles that are formed stochastically with a fixed efficiency per free-fall time in gas cells on the finest level of refinement in their simulation that satisfy a suitably chosen criterion. In their "density-regulated" models, this criterion is a simple density threshold: star formation is permitted only in gas denser than $n_{\rm th} = 10^6$ cm^{-3}.

In their "magnetically-regulated" models, on the other hand, star formation is permitted only in cells that are magnetically supercritical, although their adoption of a fixed star particle mass also acts as an effective density threshold, preventing stars from forming in cells less dense than 3.55×10^5 cm^{-3} in most of their "magnetically-regulated" runs. Notably, W17 do not require the gas flow to be converging or the gas to be gravitationally bound in order for it to be eligible to form stars.

A final difference between the treatment of star formation in the two approaches is that the star particles formed in the W17 simulations have a fixed mass from the moment that they form, whereas our sink particles can continue to accrete mass as they age. W17 argue that fixing the star particle mass is a way of approximately accounting for the effects of stellar feedback, but a comparison between our runs and those of W17 shows that we actually recover much lower star formation rates, by around an order of magnitude, even without this restriction. Similar to the studies by W17, we also do not take stellar feedback into account in this set of simulations. Neglecting supernovae is justified because our computation covers a period of only a few Myr after the onset of star formation (see Figure 3.6), which is shorter than the time required for the first supernovae to occur (Kippenhahn et al., 2012). Ignoring stellar winds and radiation is also justified at early times, but is less valid once the total stellar mass exceeds a few hundred solar masses, as at this point we would expect to have formed at least a few stars massive enough to start ionising their surroundings and driving strong stellar winds. Nevertheless, the importance of these forms of feedback for gas removal depends very much on the properties of the star cluster and its parental cloud (e.g. Rahner et al., 2017; Haid et al., 2018; Rahner et al., 2019), and it is unclear how much impact they would have in our simulated clouds.

We also note that our main results do not depend on this simplification. The difference between the star formation rates in the different runs becomes apparent very early on, long before stellar feedback from massive stars could possibly play a role in the evolution of the clouds, and so even if we were to have terminated our simulations at the point that the first massive star forms in each case, we would have come to the same conclusions. Finally, the neglect of feedback from protostellar outflows likely does affect the star formation rate at all times in the simulation. However, previous numerical studies have shown that the impact of this form of feedback is always negative: it reduces the star formation rate by a factor of around 2–3 compared to models that do not account for it (see e.g. Federrath, 2015; Hu et al., 2022). Its absence from our simulations therefore cannot explain the discrepancy between our results and those of W17.

We have assumed that the impact of stellar feedback on the star formation rate is

always negative. This is a good approximation on the scales of individual star-forming clouds (Grisdale et al., 2017), but on larger scales it is possible that feedback could in some circumstances be positive, triggering the compression of gas and the onset of star formation somewhere else in the galaxy (Shore, 1981). However, exploring the effect of feedback on these scales lies far outside of the scope of this thesis.

The simplest explanation for the difference between our study and the results of W17 is the different star formation criteria applied in the two approaches. W17 motivate their adoption of a simple density or mass-to-flux ratio threshold on the grounds of the limited resolution of their simulations (smallest cell size $\Delta x = 0.125$ pc), which does not make them confident that they can resolve the small scale structure of the gas well enough to apply a more complicated criterion. Our spatial resolution is much better in gravitationally collapsing regions, thanks to the Jeans refinement criterion, with our minimum cell size becoming as small as $\sim 10^{-4}$ pc shortly before sink particle formation. We therefore do a much better job of resolving the structure of the dense gas and can easily distinguish between dense gas that is gravitationally bound and star-forming and dense gas that is not gravitationally bound. Since there is evidence that a significant fraction of the dense gas produced in the collisions is not gravitationally bound, as we have already seen in Section 3.3.2, it is therefore unsurprising that we recover much smaller star formation rates than in the W17 simulations, but that are much more in line with the results found by other studies using a sink particle based approach (Tanvir & Dale, 2020; Dobbs et al., 2020).

The sink particle studies mentioned here do differ in their sink protocols. All studies include a sink creation density threshold and require the sink-forming cell (or particle) to lie at a potential minimum. Whilst this study and Liow & Dobbs (2020) have a similar protocol (this study having a higher sink creation density threshold), Tanvir & Dale (2020) do not have either a gas convergence or a boundedness check in their sink creation protocol. Instead, they opt for further constraints on where sinks form that required that the sink-forming gas is not tidally interacting with other sinks, and that it is capable of undergoing free-fall collapse before interacting with another sink.

The lower density threshold of Liow & Dobbs (2020) could conceivably result in more sink particles forming than in our simulation, but the factor by which the SFR is enhanced should be unaffected provided the threshold density is consistent in simulations with and without collision. The same argument can be made for Tanvir & Dale (2020): we would again expect their comparison of star formation rates between colliding and non-colliding runs to be meaningful, since their protocol is consistent across the simulations.

The differences in the sink creation protocol has scope to yield significant differences

in the SFR enhancement across the studies, yet it has not. This suggests that the active accretion onto sink particles limits the enhancement in the SFR with GMC collisions in comparison to fixed mass star particles.

That all said, we stress that this remains merely our most plausible hypothesis for the difference in outcomes. To confirm this would require us to carry out simulations similar to the ones presented here but using exactly the same star formation prescription as in W17 as well as simulations with the same initial conditions as Tanvir & Dale (2020) and Liow & Dobbs (2020), a task which is outside of the scope of our current study.

It should also be noted that the use of star particles in the context of molecular cloud/GMC-scale star formation is uncommon. Previous works looking at colliding clouds or flows mostly use a sink particle based prescription for star formation (for example Tanvir & Dale 2020; Dobbs et al. 2020; Dobbs & Wurster 2021). A star particle approach is more commonly used in galaxy-scale and larger simulations where individual GMCs are at best barely resolved. On these scales the justification for a probabilistic approach to star formation is acceptable as the gravitationally-bound cores within GMCs are not resolved and the GMCs themselves are not necessarily gravitationally bound (e.g., see Dobbs et al., 2011).

Treatment of chemistry and cooling

Although we consider the difference in the star formation algorithm to be the most likely cause of the difference between our results and those of W17, it is worthwhile examining whether the difference in our chemical and thermal treatment may also play a role here. As previously mentioned, in our simulations, we use a modified version of the Gong et al. (2017) chemical network, together with the atomic and molecular cooling function described in Clark et al. (2019). On the other hand, W17 make use of the Grackle library (Smith et al., 2017). The chemical networks provided in Grackle allow one to model the non-equilibrium chemistry of hydrogen (including H_2 formation and destruction), but do not account for the chemistry of metals such as carbon or oxygen. To account for heating and cooling due to metals, Grackle uses a table-based approach: the relevant rates are interpolated from a set of tables in which the rates are given as a function of density, temperature and (optionally) metallicity. Grackle includes several sets of tables computed using the Cloudy photodissociation region (PDR) code (Ferland et al., 1998), but also allows the user to supply their own. W17 make use of this latter option, using a set of cooling tables generated by Wu et al. (2015) using the PyPDR code (Bruderer, 2019).

The impact of this difference in approach can be seen if we compare the temperature distribution of the dense gas in our simulations (shown in Figure 3.12) with the

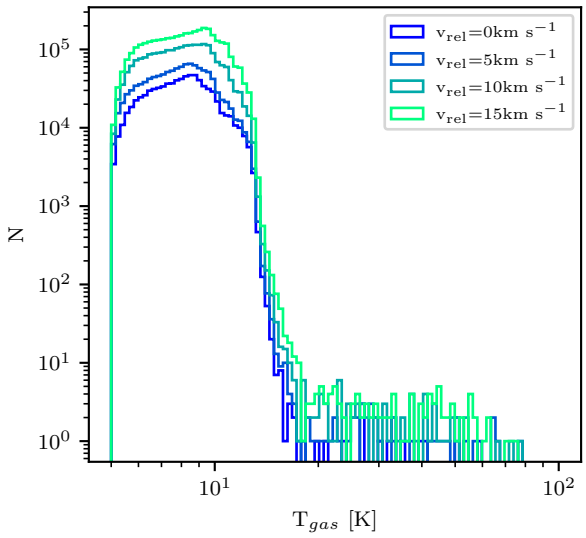

Figure 3.12. Temperature distribution of all gas cells of $n \geq 10^5 \mathrm{cm}^{-3}$ for different collisional velocities at 1 Myr after initial sink particle creation.

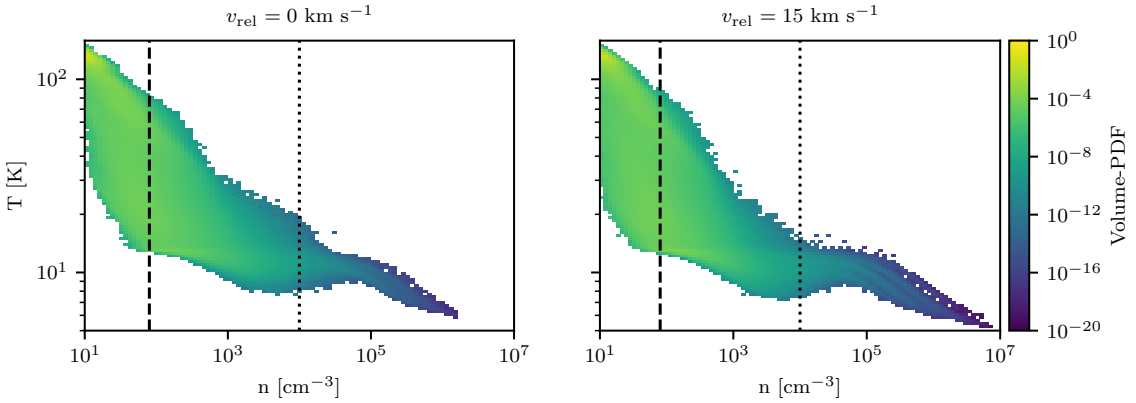

Figure 3.13. Volume-weighted temperature-density phase diagram for $v_{\mathrm{rel}} = 0\,\mathrm{km\,s^{-1}}$ (left panel) and $v_{\mathrm{rel}} = 15\,\mathrm{km\,s^{-1}}$ (right panel), shown for the snapshot immediately prior to the formation of the first sink particle. The dashed vertical line is the initial density of the clouds and the dotted vertical line is the density above which we consider the gas to be dense. The impact of v_{rel} on the temperature distribution is small, owing to the short cooling time of the gas.

temperature distribution of the star-forming gas in the W17 simulations (shown in their figure 6). We find that most of the dense gas in our simulations has a temperature in the range $5 < T < 20$ K, with a small tail in the distribution extending up to ~ 100 K. We also find that there is no clear difference in the temperature distribution of the dense gas between the colliding ($v_{\rm rel} > 0$ km s^{-1}) and the stationary ($v_{\rm rel} = 0$ km s^{-1}) clouds. On the other hand, W17 recover a somewhat broader temperature distribution, covering the range $10 < T < 40$ K in their non-colliding runs and extending up to ~ 100 K in the colliding runs. This broader temperature distribution may be a consequence of the stronger UV field adopted in their calculation – they assume $G_0 = 4$, compared to $G_0 = 1.7$ here – or may be due to some other aspect of the way in which cooling is treated in the two sets of simulations. Whatever the reason, it is clear that the difference in temperature distributions cannot explain the different star formation rates recovered in the simulations: the dense gas in our simulations is colder on average than that that in the W17 models and hence has less thermal support, meaning that it should be more likely to form dense regions and then stars, rather than less likely. Figure 3.13 demonstrates this point by showing the temperature-density distribution of the gas in the simulations with $v_{\rm rel} = 0$ km s^{-1} and $v_{\rm rel} = 15$ km s^{-1} at the snapshot just before sink formation. We see that the phase diagram is similar in both simulations, although there is more dense gas in the run with $v_{\rm rel} = 15$ km s^{-1}. If the difference between the simulations were due solely to the difference in the temperature distributions, we would expect to find a higher SFR in our simulations than in W17, which is the opposite of what we actually see.

3.4.2 Do cloud collisions trigger star formation?

There is growing observational evidence, summarized recently by Fukui et al. (2021), that the formation of massive stars is often associated with molecular clouds that show signs of having undergone a cloud-cloud collision. This suggests that collisions are generally the cause of the formation of the massive stars, i.e. that they would not have formed in the absence of the collision. Unfortunately, observational studies of this issue have an obvious drawback: they can only tell us what did happen, not what would have happened had the situation been different. Simulations, on the other hand, allow us to directly compare the outcome with or without a collision, or with different parameters for the collision, enabling us to better understand the extent to which the collision actually triggers star formation.

In the work presented here, we have insufficient dynamical range to follow the formation of individual stars, and so we cannot directly address the question of whether

the collision makes massive star formation more likely. However, we can explore the more general question of whether star formation overall is triggered by the collision between our simulated clouds. Here, the lesson of the simulations is somewhat mixed. It is clear from the fact that star formation occurs in our $v_{\rm rel} = 0$ km s^{-1} control run that the cloud collision is not required in order for the clouds to begin forming stars, i.e. the collision does not trigger star formation in the sense that the clouds would otherwise remain starless. That said, the fact that star formation begins earlier in the colliding clouds and proceeds at a slightly higher rate are both indicative of the collision having a positive effect overall on the star formation efficiency of the cloud. It is possible that this enhancement of star formation would eventually be lost if we were to simulate the clouds for a much longer period. Conversely, it is also possible that the difference in efficiency would persist, particularly if the cloud lifetime is short. Ultimately, resolving this will require simulations that follow the evolution of the clouds for much longer periods that cover the long-scale collapse of the cloud, beyond the initial collision, and that also accounts for the stellar feedback processes responsible for dispersing them. However, this is outside of the scope of our current study.

3.5 Conclusions

In this chapter we presented the results of a series of simulations of the collision of two magnetised molecular clouds with mean hydrogen nuclei number densities $n \sim 80$ cm^{-3} embedded in a warm, diffuse intercloud medium. In our simulations, we varied the relative velocity of the clouds, the inclination of the magnetic field relative to the collision axis, and the level of Jeans refinement adopted, and investigated the impact that these variations have on the resulting star formation rate. We found that that the different conditions caused star formation to occur at different times but that once star formation had begun, the subsequent evolution of the star formation rate was very similar in all of the simulations. Colliding clouds appear to form stars at a faster rate than clouds that do not collide, suggestive of some degree of triggering of star formation, but the difference in the star formation rates is around a factor of two to three, in line with the results reported by Tanvir & Dale (2020) but much smaller than the order of magnitude increase found by Wu et al. (2017).

We further investigated the virial parameter of regions of gas around potential minima in our simulations, and how these virial parameters depend on the collisional velocity between the clouds. We found that the virial parameters in the potential minima were higher for the higher collisonal velocities, especially in the high-density, post-shocked gas, with higher amounts of turbulence in the dense gas. Although the higher

collision velocity simulations are found to create more high denisty gas, our analysis demonstrates that much of this gas is not gravitationally bound, which explains why the correlation between collision velocity and star formation rate is so weak.

Software: AREPO (Springel, 2010b), NumPy (Harris et al., 2020), Matplotlib (Hunter, 2007), Astropy (Astropy Collaboration et al., 2013, 2018)

Chapter 4

Reliability of kinematic distances

> *"Even though science has come so far, I can barely help others with it. I wonder how far it is to where you are?"*
>
> —Kasamura Tota, *To those who I cherish*

This chapter contains works present in the paper Hunter et al. (2024) which has been submitted to the journal Astronomy and Astrophysics (A&A) and is currently in the reviewing process at time of writing. I am the first author of this paper and have constructed the potential presented within the paper, carried out the simulations and data analysis present, and primarily wrote the paper with feedback and suggestions from all co-authors. The third author, Jan Beckmann, carried out the initial version of the parameter study which contributes to the final version of it as presented in appendix B.2. The fourth author, Eugene Vasiliev, provided the script and data needed to produce figure 4.4.

Abstract

Obtaining reliable distance estimates to gas clouds within the Milky Way is challenging in the absence of certain tracers. The kinematic distance approach has been used as an alternative, derived from the assumption of circular trajectories around the Galactic centre. Consequently, significant errors are expected in regions where gas flow deviates from purely circular motions.

We aim to quantify the systematic errors that arise from the kinematic distance method in the presence of a Galactic potential that is non-axisymmetric. We investigate how these errors differ in certain regions of the Galaxy and how they relate to the underlying dynamics. We perform 2D isothermal hydrodynamical simulation of the

gas disk with the moving-mesh code Arepo, adding the capability of using an external potential provided by the Agama library for galactic dynamics. We introduce a new analytic potential of the Milky Way, taking elements from existing models and adjusting parameters to match recent observational constraints.

We find significant errors in the kinematic distance estimate for gas close to the Sun, along sight lines towards the Galactic centre and anti-centre, and significant deviations associated with the Galactic bar. Kinematic distance errors are low within the spiral arms as gas resides close to local potential minima and the resulting line-of-sight velocity is close to what is expected for an axisymmetric potential. Interarm regions exhibit large deviations at any given Galactic radius. This is caused by the gas being sped up or slowed down as it travels into or out of the spiral arm. We are able to define 'zones of avoidance' in the lv-diagram, where the kinematic distance method is particularly unreliable and should only be used with caution. We report a power law relation between the kinematic distance error and the deviation of the project line-of-sight velocity from circular motion.

4.1 Introduction

Accurate distance measurements are essential for many fields of astronomy and astrophysics (e.g. Carroll & Ostlie, 2017). Whereas high-precision astrometric data are readily available within the Milky Way for the stellar component (see, e.g., Gaia data release DR3, Gaia Collaboration et al. 2023), obtaining reliable distance estimates for the gaseous component, i.e. for the various phases of interstellar medium (ISM, see e.g., Tielens, 2005; Draine, 2011) is much more challenging. Estimating distances to molecular clouds is important for understanding their properties, formation and evolution (Molinari et al., 2014) and their ability to form stars (Klessen & Glover, 2016). The same is true for the atomic and ionised components of the ISM.

Accurate 3D maps of the gas distribution in the Solar Neighbourhood have been constructed by combining precise parallax measurements of stars from Gaia and photometric measurements of reddening to the same stars (Lallement et al., 2019; Leike et al., 2020; Zucker et al., 2021). However, this approach is currently feasible only for a limited volume of a few kpc around the Sun. Reliable distances to clouds further away can be obtained from parallax measurements of molecular maser emission from high mass star-forming regions (Reid et al., 2014, 2019), but this approach is time-consuming and cannot be applied to large surveys containing thousands of clouds.

A widely used method to estimate distances to the ISM out to tens of kpc from the Sun is the kinematic distance (KD) method. This method allows one to derive the

distance to a molecular cloud from its line-of-sight (LOS) velocity. Historically, it was developed by van de Hulst et al. (1954) and Oort et al. (1958), who used it to derive the first face-on maps of atomic hydrogen in the Milky Way from 21-cm spectral line observations. The same approach has since been applied several times to produce face-on maps of the neutral and molecular gas in the Milky Way (e.g. Nakanishi & Sofue, 2003, 2006; Levine et al., 2006; Soler et al., 2022) and the associated star-formation rate surface density (Elia et al., 2022).

A key assumption of the KD approach is that the gas is in purely circular motion around the Galactic centre. Significant errors in the KD distance estimations arise if there are deviations from circular motions. Wenger et al. (2018) recently compared kinematic and parallax distances for a sample of 75 Galactic high mass star-forming regions, most of which are at distances $d < 10\,\mathrm{kpc}$, and found that indeed kinematic distances usually overestimate the distance by $\sim 20\%$ and have errors of order 50%.

Errors arising from deviations from circular motions can be broadly divided into two categories: (i) random fluctuations around the average streaming motions that do not change the average velocity (e.g., a turbulent velocity dispersion); (ii) systematic changes in the streaming velocity due to non-axisymmetric features such as spiral arms and the Galactic bar.

Reid (2022) studied the effects of random motions on the KD distances and found that a velocity dispersion of $\sim 7\,\mathrm{km\,s^{-1}}$, representative of turbulent motions in giant molecular clouds, can lead to significant ($> 10\%$) errors in the KD distance for true distances $d \lesssim 5\,\mathrm{kpc}$, and can also lead to systematic biases of $\sim 20\%$ despite the random motions having zero mean around the underlying circular motions. Sofue (2011) quantified the expected distribution of uncertainties from random motions as a function of position in face-on maps of the Galaxy, finding that small Galactic longitudes are more heavily affected (see their Figure 9).

A number of authors have investigated the effects of streaming motions due to spiral arms using simplified models of the Milky Way. Gómez (2006) used 2D hydrodynamical simulations with a simple externally imposed two-armed spiral pattern to compare KD with true distances, and found that errors can be large at the position of the spiral arms. Baba et al. (2009) employed self-consistent N-body + hydrodynamical simulations with a live stellar potential, and found that transient and recurring spiral arms can drive strong non-circular motions, meaning that KD distances can produce errors as large as 4-6 kpc near spiral arms. Also using hydrodynamical simulations, Ramón-Fox & Bonnell (2018) found that streaming motions can produce systematic offsets of $\sim 1\,\mathrm{kpc}$, errors of $\sim 2\,\mathrm{kpc}$, and that the results are sensitive to the assumed spiral arm perturbations. Some works have tried to correct the KD method to account for the sys-

tematic non-circular motions due to spiral arms and bar, but the results are affected by large uncertainties in the gas streaming motions arising from these components (Foster & MacWilliams, 2006; Pohl et al., 2008).

The goal of this chapter is to quantify the KD uncertainties caused by streaming motions due to spiral arms and the bar as a function of position in the Galaxy using a much more accurate Milky Way model than previous work, and therefore construct maps of the expected systematic uncertainties that can provide useful guidance as to when the KD method should be considered reliable and when it should be avoided. To do this, we construct a realistic model of the Galactic gravitational potential that includes state-of-the-art constraints on the Galactic bar, Galactic disk, dark matter halo and spiral arms, and run 2D hydrodynamical simulations using this potential. We then compare actual and kinematic distances in the model, paying particular attention to the inner regions of the Galaxy dominated by the bar and to the regions around the spiral arms.

After a brief discussion of the context of this study in Section 4.1, we introduce our new analytic description of the Milky Way potential and its various components in Section 4.2. We briefly describe our numerical approach and the implementation of the new potential in the Agama frameworks combined with Arepo in Section 4.3. Our main findings are presented in Section 4.4, and their implications and limitations discussed in Section 4.5. Finally, we summarise and conclude in Section 4.6.

4.2 Galactic potential

We introduce a new gravitational potential for our Milky Way-like simulation in order to investigate how non-axisymmetric perturbations affect kinematic distance estimates. The potential comprises of many components, each providing structure in different parts of the Galaxy, as detailed in the following sections.

The corresponding circular-velocity curves are shown in Figure 4.1, and the total midplane density profile of our potential, ρ_{gal}, is shown in Figure 4.2.

4.2.1 Components of the potential

Supermassive black hole Sgr A*

The potential of the central supermassive black hole, Sgr A*, is represented by a Plummer (1911) model:

$$\Phi_{\mathrm{SgrA}^\star} = -\frac{GM_{\mathrm{SgrA}^\star}}{\sqrt{r^2+b^2}}\,, \tag{4.1}$$

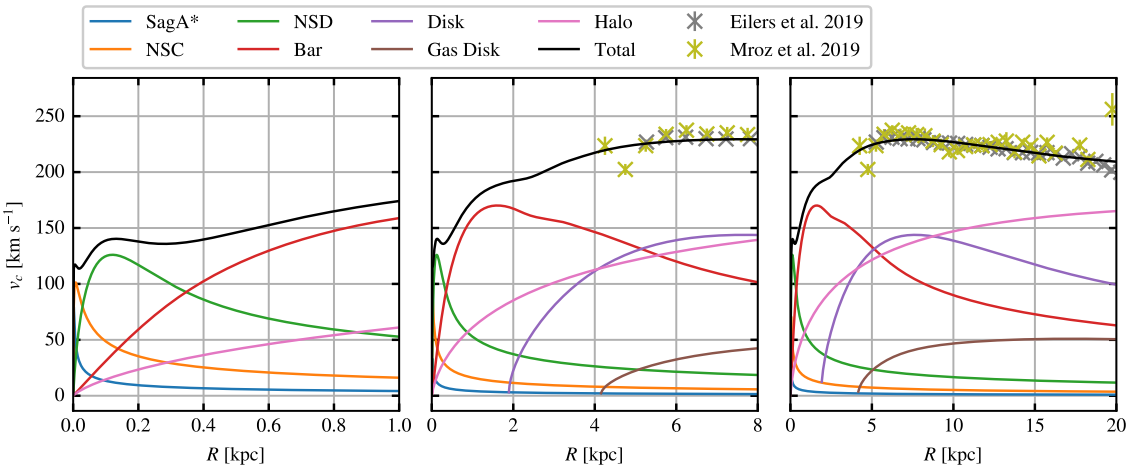

Figure 4.1. Circular-velocity curve produced by our model (black line). The contribution of each component of the potential represented by the coloured lines as detailed in the legend. Observation points from Eilers et al. (2019) and Mróz et al. (2019) are also included (colored markers). Left, middle and right panels feature the profile for a radius between 0 and 1 kpc, 0 and 8 kpc and 0 and 20 kpc respectively. All axis scales are linear.

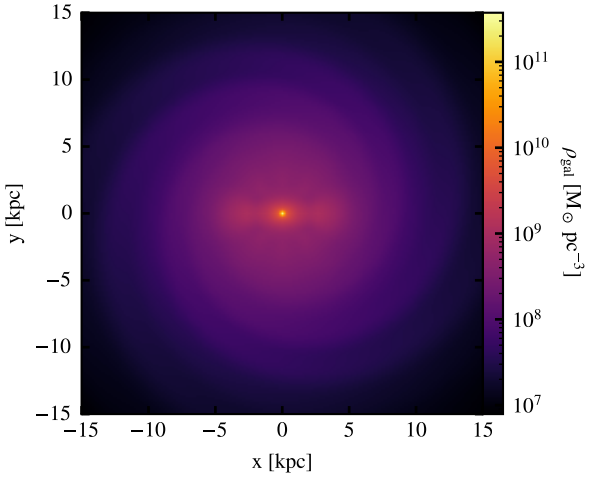

Figure 4.2. Density distribution of the underlying gravitational potential within the midplane ($z = 0$ kpc) of the galaxy.

where G is the gravitational constant, the mass $M_{\mathrm{SgrA}^\star} = 4.154 \times 10^6\,\mathrm{M}_\odot$ is taken from GRAVITY Collaboration et al. (2019), r is the spherical Galactic radius and the scale radius b is set to 0.1 pc to avoid a singularity in the potential.

Nuclear star cluster

The cluster of stars around Sgr A* also contributes to the potential within the core of the Galaxy, dominating in the innermost few pc. In our model, the NSC follows a flattened Dehnen (1993) density profile as given in Chatzopoulos et al. (2015, see their Equation 17):

$$\rho_{\mathrm{NSC}} = \frac{(3-\gamma)M_{\mathrm{NSC}}}{4\pi q}\frac{a_0}{a^\gamma(a+a_0)^{4-\gamma}}\,, \tag{4.2}$$

where

$$a(R,z) = \sqrt{R^2 + \frac{z^2}{q^2}}\,. \tag{4.3}$$

The parameters $\gamma = 0.71$, $q = 0.73$, $a_0 = 5.9$ pc and $M_{\mathrm{NSC}} = 6.1\times10^7\mathrm{M}_\odot$ are taken from their best-fitting model. Here R refers to the Galactic radius in cylindrical coordinates. We note from our circular-velocity curve (Fig. 4.1) we see little contribution to the overall potential from Sgr A* and the NSC. This is due to these components being most dominant in the inner most 100 pc of the galaxy making it difficult to compare against observational rotation curves and terminal velocities. However, we do include these components for the sake of completeness.

Nuclear stellar disk

For the NSD surrounding the nuclear region, we adopt the parameterisation from the Jeans modelling analysis of Sormani et al. (2020) based on data from the APOGEE survey (Majewski et al., 2017; Ahumada et al., 2020) and the 86 GHz SiO maser survey of Messineo et al. (2002, 2004, 2005). The density of this component can be written as:

$$\rho_{\mathrm{NSD}} = \rho_1 \exp\left[-\left(\frac{a}{R_1}\right)^{n_1}\right] + \rho_2 \exp\left[-\left(\frac{a}{R_2}\right)^{n_2}\right] \tag{4.4}$$

where a is as defined in Equation (4.3) but with $q = 0.37$, and where $n_1 = 0.72$, $n_2 = 0.79$, $R_1 = 5.06$ pc, $R_2 = 24.6$ pc, $\rho_1/\rho_2 = 1.311$ and $\rho_2 = 153 \times 10^{10}$ $\mathrm{M}_\odot$ kpc^{-3}, which follows model 3 of Sormani et al. (2020). As shown in Figure 4.1, this component dominates between the inner ∼20 pc and ∼300 pc of the Galaxy. We opt this model over the more recent model of Sormani et al. (2022a) as the density profile of Sormani et al. (2020) is available in a closed, analytical form. This difference only affects the inner most ∼300 pc of the simulation which is only a minor impact in comparison to the larger scale of the whole Galaxy.

Galactic bar

The Galactic bar dominates much of the potential within the inner ∼5 kpc of the Galaxy. The most realistic model for this component is the made-to-measure (m2m) model from Portail et al. (2017). It is constrained using red giant stellar density measurements and kinematics from multiple surveys across the entire bar region. Here we make use of the analytical approximation of this model presented by Sormani et al. (2022b), who provide density functions to describe the X-shaped box/peanut bar and the long bar. We reiterate the functions used and their parameters here to have a complete description of our potential in this chapter:

$$\rho_{\rm bar} = \underbrace{\rho_{\rm bar,1} + \rho_{\rm bar,2}}_{\rm bar} + \underbrace{\rho_{\rm bar,3}}_{\rm long\ bar} \ . \tag{4.5}$$

The first component of Equation (4.5) corresponds to the X-shaped component of the observed boxy-peanut shape of the bar (Wegg & Gerhard, 2013). To describe this, we use a modified form of Equations 9 and 10 of Coleman et al. (2020) and Freudenreich (1998), respectively:

$$\begin{aligned}\rho_{\rm bar,1}(x,y,z) = \rho_1 &{\rm sech}\left(a^m\right) \\ &\times \left[1 + \alpha\left(e^{-a_+^n} + e^{-a_-^n}\right)\right] e^{-\left(\frac{r}{r_{\rm cut}}\right)^2} ,\end{aligned} \tag{4.6}$$

where

$$a = \left\{\left[\left(\frac{|x|}{x_1}\right)^{c_\perp} + \left(\frac{|y|}{y_1}\right)^{c_\perp}\right]^{\frac{c_\parallel}{c_\perp}} + \left(\frac{|z|}{z_1}\right)^{c_\parallel}\right\}^{\frac{1}{c_\parallel}} , \tag{4.7}$$

$$a_\pm = \left[\left(\frac{x \pm cz}{x_c}\right)^2 + \left(\frac{y}{y_c}\right)^2\right]^{\frac{1}{2}} , \tag{4.8}$$

$$r = \left(x^2 + y^2 + z^2\right)^{\frac{1}{2}} . \tag{4.9}$$

Here, $\alpha = 0.626$ defines the strength of the X-shape whilst $c = 1.342$ defines the slope of the X-shape in the $x - z$ plane. The scale lengths $x_1 = 0.49$ kpc, $y_1 = 0.392$ kpc, $z_1 = 0.229$ kpc, $x_c = 0.751$ kpc and $y_c = 0.469$ kpc, shape the bar along with the shaping parameters $c_\perp = 2.232$ and $c_\parallel = 1.991$. The X-shape of the bar trails off with power law exponents with powers $m = 0.873$ and $n = 1.94$ with an additonal cutoff radius at $r_{\rm cut} = 4.37$ kpc. The density profile is normalised to $\rho_1 = 3.16 \times 10^9$ M$_\odot$ kpc^{-3}.

The second and third component of $\rho_{\rm bar}$ describe the ellipsoid shape of the bar, which we split into short (ρ_2) and long (ρ_3) bar components. Both components follow

Table 4.1. Parameters for components 2 and 3 of the bar potential

Parameter	Value	
	Component 2	Component 3
ρ_i [$M_\odot$ kpc^{-3}]	0.5×10^9	174.305×10^{11}
x_i [kpc]	5.364	0.478
y_i [kpc]	0.959	0.297
z_i [kpc]	0.611	0.252
$R_{i,\mathrm{in}}$ [kpc]	0.558	7.607
$R_{i,\mathrm{out}}$ [kpc]	3.19	2.204

a modified version of Equation 9 of Wegg et al. (2015):

$$\rho_{\mathrm{bar,i}}(x,y,z) = \rho_i \, e^{-a_i^{n_i}} \operatorname{sech}^2\left(\frac{z}{z_i}\right) \times e^{-\left(\frac{R}{R_{\mathrm{i,out}}}\right)^{n_{\mathrm{i,out}}}} e^{-\left(\frac{R_{\mathrm{i,in}}}{R}\right)^{n_{\mathrm{i,in}}}}, \tag{4.10}$$

where $i = \{2, 3\}$ and

$$a_i = \left[\left(\frac{|x|}{x_i}\right)^{c_{\perp,i}} + \left(\frac{|y|}{y_i}\right)^{c_{\perp,i}}\right]^{\frac{1}{c_{\perp,i}}}, \tag{4.11}$$

$$R = \left(x^2 + y^z\right)^{\frac{1}{2}}. \tag{4.12}$$

We summarise the parameters used for the components 2 and 3 of the bar in Table 4.1. The total mass contained within the bar is $M_{\mathrm{bar}} = 1.83 \times 10^{10}$ $M_\odot$.

Galactic disk -- axisymmetric components

The disk potential of our model takes the form of two exponential disk components with a hole in the centre, introduced to make room for the bar. We adopt a modified version of Equation 3 of McMillan (2017) using an exponential vertical profile. We obtain

$$\rho_{\mathrm{disk}}(R,z) = \frac{\Sigma_1}{2h_1} \exp\left(-\frac{R}{R_{\mathrm{d},1}} - \frac{R_{\mathrm{cut}}}{R} - \frac{|z|}{h_1}\right) + \frac{\Sigma_2}{2h_2} \exp\left(-\frac{R}{R_{\mathrm{d},2}} - \frac{R_{\mathrm{cut}}}{R} - \frac{|z|}{h_2}\right), \tag{4.13}$$

where $\Sigma_1 = 1.3719 \times 10^3$ $M_\odot$ pc^{-2}, $R_{d,1} = 2$ kpc, $z_1 = 300$ pc, $\Sigma_2 = 9.2391 \times 10^2$ $M_\odot$ pc^{-2}, $R_{d,2} = 2.8$ kpc, $z_2 = 900$ pc, and $R_{\mathrm{cut}} = 2.4$ kpc. The inner cutoff radius R_{cut}, scale lengths R_{d} and surface density normalizations Σ are obtained by fitting our model to the circular-velocity curves of Eilers et al. (2019) and Mróz et al. (2019) as

shown in Figure 4.1, whereas the scale heights h are fixed to the values from McMillan (2017), which are, in turn, obtained from SDSS star counts by Jurić et al. (2008). The parameterisation of the disk keeps the scale height fixed across all Galactic radii for simplicity, despite observations indicating the scale height decreases towards the Galactic centre. For example, $h(R = 4\text{kpc}) \sim 180\text{pc}$ for the thick stellar disk (Wegg et al., 2015).

In order to better represent the vertical acceleration towards the midplane of the Galaxy (for $z < 400$ pc), we also include two gas disks in the potential, which we take from McMillan (2017) without any further adjustments:

$$\begin{aligned}\rho_{\text{gas}}(R,z) = &\frac{\Sigma_1}{4z_1}\exp\left(-\frac{R_{m,1}}{R}-\frac{R}{R_{d,1}}\right)\text{sech}^2(z/2z_1)\\ &+\frac{\Sigma_2}{4z_2}\exp\left(-\frac{R_{m,2}}{R}-\frac{R}{R_{d,2}}\right)\text{sech}^2(z/2z_2)\ ,\end{aligned} \tag{4.14}$$

where $\Sigma_1 = 53.1\ \text{M}_\odot\ \text{pc}^{-2}$, $R_{d,1} = 7$ kpc, $z_1 = 85$ pc, and $R_{m,1} = 4$ kpc represents the thick H I disk, whilst $\Sigma_2 = 2.18 \times 10^3\ \text{M}_\odot\ \text{pc}^{-2}$, $R_{d,2} = 1.5$ kpc, $z_2 = 45$ pc, and $R_{m,2} = 12$ kpc represents the thinner H_2 disk. Note that the gas disk in the hydrodynamical simulations in this chapter is not self-gravitating and does not contribute to the potential; instead, these two gas disks are included as static components of the potential. It should also be noted that the gas disk potential does not contain a spiral perturbation, as we are interested in how the stellar potential affects the gas distribution in the simulations.

Galactic disk -- spiral arms

To generate the spiral arms of the Galaxy, we introduce a perturbation to the stellar disk in the following manner:

$$\rho_{\text{spiral}}(R,z,\phi) = \rho_{\text{disk}}(R,z)\cdot\alpha\frac{R^2}{R_0^2}S(R,\phi). \tag{4.15}$$

Here the perturbation strength increases quadratically with radius in order for the spiral arms to be strong enough in the outer regions of the Galaxy. The strength factor, $\alpha = 0.36$, is set such that the spiral arm strength is 18% of the disk density at solar radius, $R_0 = 8.179$ kpc. This amplitude is almost two times stronger than the 10% suggested by Eilers et al. (2020) for the Milky Way. However, we note from our tests that a density perturbation of 10% is not strong enough to generate spiral arms in our simulations (see Appendix B.1).

For the shaping function, S, we make use of a logarithmic spiral arm potential with the width of the arm having a Gaussian profile. We take a modified form of Equation

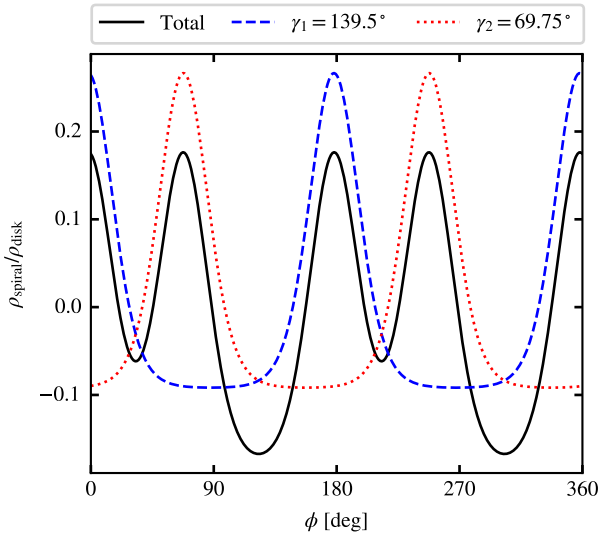

Figure 4.3. The strength of the spiral arms at solar circle, $R = 8.179$ kpc, as a function of azimuth. Shown is the strength of the spiral arms in black, as well as the f_{m_1,γ_1} and f_{m_2,γ_2} components in blue and red respectively.

8 of Junqueira et al. (2013):

$$S(R,\phi) = \sum_{k=1}^{2} \left\{ \exp\left(-\frac{R^2}{\sigma_{\rm sp}^2}\left[1 - f_{m_k,\gamma_k}(R,\phi)\right]\right) - \exp\left(-\frac{R^2}{\sigma_{\rm sp}^2}\right) I_0\left(-\frac{R^2}{\sigma_{\rm sp}^2}\right) \right\}, \tag{4.16}$$

where

$$f_{m,\gamma}(R,\phi) = \cos\left(m(\phi+\gamma) - \frac{m}{\tan(i)} \ln\left(\frac{R}{R_a}\right)\right) , \tag{4.17}$$

and $i = 12.5°$ and $R_a = 9.64$ kpc, $m_1 = m_2 = 2$, $\gamma_1 = 139.5°$ and $\gamma_2 = 69.75°$. $\sigma_{\rm sp} = 5$ kpc is the width parameter of the spiral arm which corresponds to a physical width of 1.082 kpc perpendicular to the spiral arm. The second term in Equation (4.16) is used to normalise the spiral arm potential such that the monopole component is zero. Here, I_0 is the modified Bessel function of the first kind and of zeroth order. This resulting potential is a superposition of two pairs of $m = 2$ spiral arms with equal amplitude (Li et al., 2022). We note that the spiral arm potential does not have an $m = 4$ pattern due to the unequal angular separation between spiral arms. We opt for this kind of pattern as it allows for the angular separation to be adjusted as needed as the spiral arms of the Milky Way are not fixed to 90° in angular separation (Reid et al., 2019). The shape and intensity of the spiral arms at $R = 8.179$ kpc is shown in Figure 4.3.

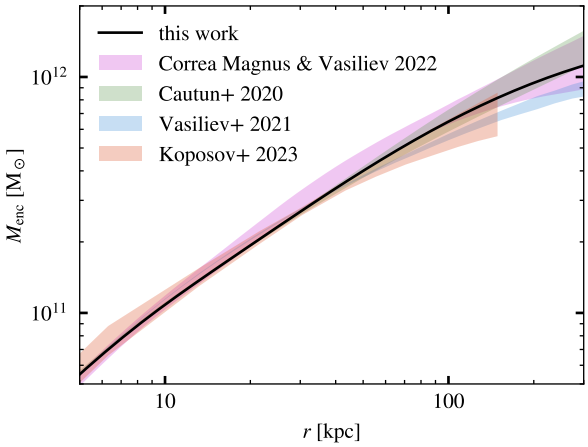

Figure 4.4. Enclosed mass profile of our fiducial potential (black), compared to the constraints from dynamical modelling of satellite galaxies (magenta: Correa Magnus & Vasiliev 2022, green: Cautun et al. 2020) and streams (blue: Vasiliev et al. 2021, red: Koposov et al. 2023).

Dark matter halo

The dark matter halo component follows a spherical Einasto (1969) profile:

$$\rho_{\rm dm}(r) = \rho_0 \exp\left[-\left(\frac{r}{a}\right)^{1/n}\right]. \tag{4.18}$$

The density normalisation, ρ_0, is determined by using the total mass of an Einasto potential:

$$M = 4\pi\,\rho_0\,a^3\,n\,\Gamma(3n)\ , \tag{4.19}$$

where the total mass is $M = 1.1 \times 10^{12}$ $\mathrm{M}_\odot$, the Einasto index is $n = 4.5$ and Γ is the gamma function. The scale radius a is related to the half mass radius r_s by $a \approx r_s\,(3n - 1/3)^{-n}$. In this case, the half mass radius is $r_s = 96\,\mathrm{kpc}$ giving a scale radius of $a = 0.88\,\mathrm{pc}$. These parameters are optimized to simultaneously fit the circular-velocity in the inner region of the Galaxy and its mass distribution at larger distances determined from dynamical modelling of satellite galaxies and stellar streams (Cautun et al., 2020; Correa Magnus & Vasiliev, 2022; Vasiliev et al., 2021; Koposov et al., 2023) (see Figure 4.4).

4.2.2 Comparison with observations

The parameters of the fiducial potential were optimized to satisfy a variety of recent observational constraints, as described below.

Axisymmetric components

We begin with the Galactic circular-velocity curve, as illustrated in Figure 4.1 for different radial bins. The black line represents our total circular-velocity curve from the axisymmetrised potential, $v_c = (R\,\partial\Phi_0/\partial R)^{1/2}$, with the colored lines indicating the contributions from individual components based on the choice of parameters outlined above. Here the axisymmetrised potential is obtained from the monopole, $m = 0$, component of the potential in which has been approximated by a Fourier or multipole expansion (see Sect. 4.3.2). The resulting circular-velocity curve does not contain perturbations from the spiral arms nor contains the higher order terms needed to describe the full potential of the bar.

We make use of recent measurements of circular velocity data from Eilers et al. (2019), obtained from red giant star observed with *APOGEE, WISE* and *Gaia*, and from Mróz et al. (2019), obtained from Cepheid variable stars with *Gaia*. Both are in a reasonable agreement with each other and provide a coverage of Galactocentric radius of $4 \lesssim R \lesssim 25$ kpc. For coverage within the solar circle, $R < R_0$, we make of use of the terminal velocities measurements from H I and CO observations (Clemens, 1985; Fich et al., 1989; Burton & Liszt, 1993; McClure-Griffiths & Dickey, 2007). We compare the peaks of the resulting longitude-velocity (lv) diagrams from our hydrodynamical simulations with the corresponding terminal velocity measurements of the Milky Way, as discussed in detail in Section 4.4. Here we opt to compare terminal velocities in the lv diagram instead of the circular-velocity/rotation curves within the inner most $R < 4$ kpc, as rotation curves obtained from observations in this region will include deviations due to the non-axisymmetric nature of the bar (Chemin et al., 2015). These deviations are not present in our axisymmetrised circular-velocity curve.

We consider the surface density of the disk as a function of Galactocentric radius, as well as the vertical acceleration at two different heights above and below the midplane to verify our potential is consistent with result derived from observations off the midplane. For the surface density of the disk and vertical acceleration at $|z| = 1.1$ kpc we make use of data presented in Bovy & Rix (2013) from SEGUE data of G-type dwarf stars. For vertical accelerations closer to the midplane at $|z| = 400$ pc, we make use of the data presented in Widmark et al. (2022) obtained from modelling the vertical oscillations ("phase spiral") in *Gaia* EDR3. Figure 4.5 shows how our potential compares to the observations in these aspects. We also include the `MWPotential2014` model from Bovy (2015) for comparison.

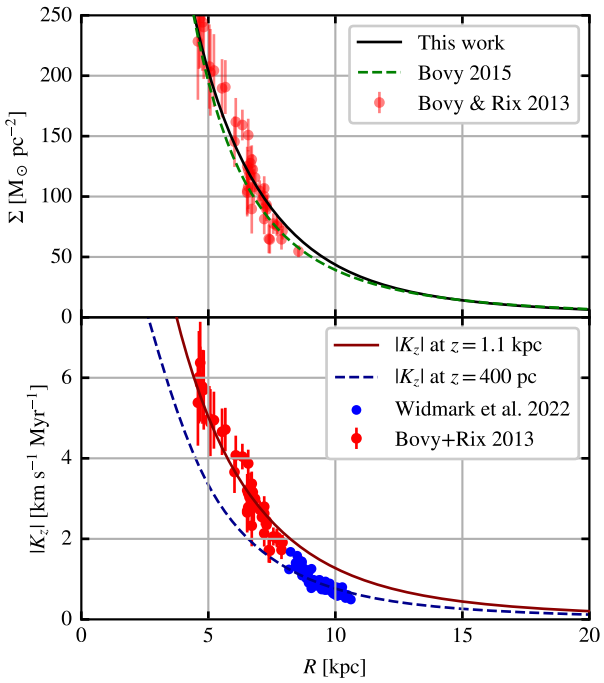

Figure 4.5. The top plot shows the surface density as a function of galactocentric radius as derived from our model (black line) with comparison to that derived from Bovy (2015). The red points are the measured values for the Milky Way from Bovy & Rix (2013). The bottom plot shows the vertical acceleration at $|z| = 400$ pc (dashed blue line) and $|z| = 1.1$ kpc (solid red line). The two colours of data points represents the vertical acceleration at different scale height with the blue points being at $|z| = 400$ pc (Widmark et al., 2022) and the red points at $|z| = 1.1$ kpc (Bovy & Rix, 2013).

Table 4.2. Location of resonances of the non-axisymmetric components of the potential.

Resonance	ILR (kpc)	In 4:1 (kpc)	CR (kpc)	Out 4:1 (kpc)	OLR (kpc)
Bar	1.02	3.45	6.08	8.24	10.14
Spiral arms	2.36	6.50	10.07	13.06	15.89

Notation of resonances: ILR = Inner Lindblad, In 4:1 = inner 4:1, CR = corrotation, Out 4:1 = outer 4:1, OLR = outer Lindblad

Non-axisymmetric components

Our potential has two rotating non-axisymmetric components, the bar and the spiral arms. We chose the pattern speeds of the bar and the spiral arms as $\Omega_{\mathrm{bar}} = -37.5$ km s^{-1} kpc^{-1} (e.g. Sormani et al., 2015b; Sanders et al., 2019; Li et al., 2022; Clarke & Gerhard, 2022) and $\Omega_{\mathrm{spiral}} = -22.5$ km s^{-1} kpc^{-1} (Li et al., 2022), respectively. We checked the consistency of these values by running a small parameter study with our potential to generate longitude-velocity lv diagrams and comparing them to the spiral arm tracks presented in McClure-Griffiths et al. (2004), Reid et al. (2016) and Reid et al. (2019). For the sake of simplicity, we consider both non-axisymmetric components to experience solid body rotation. See Appendix B.2 for the full details of the parameter study. The resonances for the potential can be found in Table 4.2 and are illustrated in the frequency curves of Figure 4.6. We find that for the pattern speeds we use, the outer Lindblad resonance of the bar coincides with corotation of the spiral arms at ~ 10.1 kpc. The outer 4:1 resonance of the bar lies close to solar circle at ~ 8.2 kpc.

4.3 Numerical simulations

Here we briefly describe the numerical methods used to simulate the dynamical evolution of the ISM in our Milky Way analog.

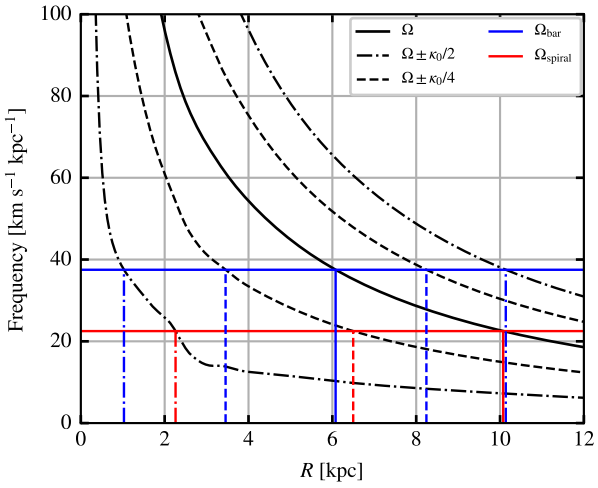

Figure 4.6. Frequency curve as a function of Galactic radius. The solid black line is the rotational frequency curve of the potential, whereas the dashed and dot-dashed lines are rotional frequency plus or minus 0.25 and 0.5 times the epicyclic frequency, $\kappa_0(R) = \sqrt{(2\Omega/R)\mathrm{d}(R^2\Omega)/\mathrm{d}R}$. The horizontal blue and red lines are the pattern speed of the bar and the spiral arms, respectively. The vertical dashed and dot-dashed lines are the corresponding resonances for bar and spiral arms.

4.3.1 Numerical hydrodynamics

We solve the equations of hydrodynamics with the moving-mesh code Arepo (Springel, 2010a). For isothermal gas in two dimensions these are

$$\frac{\partial \Sigma}{\partial t} + \nabla \cdot (\Sigma \mathbf{v}) = 0 \,, \tag{4.20}$$

$$\frac{\partial \Sigma \mathbf{v}}{\partial t} + \nabla \cdot (\Sigma \mathbf{v} \otimes \mathbf{v}) = -\nabla P - \Sigma \nabla \Phi \,, \tag{4.21}$$

where Σ, $\mathbf{v}$, and P are gas surface density, velocity and pressure, respectively. The simulations are two-dimensional. The pressure is related to the density via the equation of state, $P = c_\mathrm{s}^2 \Sigma$, with the sound speed adopted as $c_\mathrm{s} = 10\,\mathrm{km\,s^{-1}}$. The external potential Φ is given by our model for the Galactic potential, as explained in the next section; for ease of interpretation, we do not include the gas self-gravity, star formation or stellar feedback in our models. Note that by choosing a relatively large value for c_s, we are implicitly accounting for some of the turbulent support of the gas disk, something that in reality would be provided by stellar feedback (Mac Low & Klessen, 2004; Krumholz & McKee, 2005b; McKee & Ostriker, 2007; Klessen & Glover, 2016). This assumption is justified in this case as our focus is on how the large scale dynamics impact kinematic distance estimates and not on the impact by turbulent motions.

Arepo constructs a Voronoi tesselation, in which the mesh generating points are

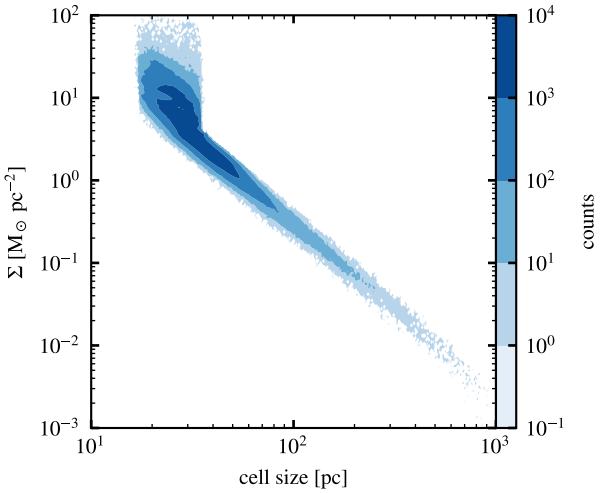

Figure 4.7. The relation between cellsize and density within our simulation. The cellsize in this case is the size of a square with the same area as the cell.

able to flow with the gas in the simulation, resulting in a quasi-Lagrangian approach to modeling the flow properties. We make use of an exact Riemann solver for isothermal flows, and the mesh can refine and derefine with the addition and removal of mesh generating points. This occurs when the mass of a given cell is a factor ∼2 larger or smaller than the cell target mass for the simulation ($M_{\rm target}$ = 2500 M$_\odot$). The cell will either split or merge with another with addition or removal of a mesh generating point. For further details of the code base we use, see e.g. Tress et al. (2020a,b). We achieve a minimum cellsize of ∼ 40 pc. Figure 4.7 illustrates how our cell size varies with density. The vertical spread seen at low cellsizes is a result of the minimum surface area of the cell being reached, which is set to 6 pc^2. This creates a limit on how small our cells can become by not allowing cells smaller than two times the minimum surface area to refine further.

4.3.2 External Galactic potential

Arepo allows one to include an external gravitational potential in the simulation, but the Galactic potential described in Section 4.2 is significantly more complex than the few built-in analytic models. Instead, it is provided by the Agama library for stellar dynamics (Vasiliev, 2019), which, among other features, contains a powerful framework for constructing and evaluating arbitrarily complex potentials (including time-dependent features such as a rotating bar with a varying amplitude and/or pattern speed). We created an interface between the two codes that make it possible to use any potential implemented in Agama as an external potential in Arepo (in addition to self-gravity of

Table 4.3. Expansion used for each component of the potential. When present, spiral arms are represented by a separate `CylSpline` potential, since they rotate with a different pattern speed than the bar.

Component	Expansion type
Sgr A*	`Multipole`
NSC	`Multipole`
NSD	`Multipole`
Bar	`CylSpline` (1)
Stellar disk	`CylSpline` (1)
Gas disk	`CylSpline` (1)
Spiral arms	`CylSpline` (2)
DM halo	`Multipole`

the simulated system, if the latter is turned on). Moreover, a very similar interface is provided for the Gadget-4 code (Springel et al., 2021), which shares a common ancestry with Arepo; both interfaces, as well as the script for generating the Galactic potential from this study, are available in the latest version of Agama.

The Galactic potential consists of two general-purpose expansions: `Multipole` for spheroidal density components, and cylindrical Fourier series (`CylSpline`) for disk-like components. Each of the two expansions is constructed from the sum of several density components, as detailed in Table 4.3; the mathematical details of these potential expansions can be found in the appendix of the Agama documentation (Vasiliev, 2018).

4.3.3 Initial conditions

The initial conditions of our simulations are simple. We set up the surface density of the gas following an exponential profile similar to Equation 4.14:

$$\Sigma(R) = \Sigma_1 \exp\left(-\frac{R_{m,1}}{R} - \frac{R}{R_{d,1}}\right) + \Sigma_2 \exp\left(-\frac{R_{m,2}}{R} - \frac{R}{R_{d,2}}\right), \tag{4.22}$$

where the parameters for this gas disk are the same as those used for the gas disk potential (See Sect. 4.2.1). We extend this gas disk to $R \sim 30$ kpc at which point we reduce the density significantly to prevent artifacts caused by periodic boundary conditions compromising the Galaxy itself. For simplicity, we initialise the simulation with 250000 mesh generating points distributed uniformly across a $(75\ \mathrm{kpc})^2$ box. The mesh is then relaxed with the `meshrelax` method within Arepo to reach our target mass of $2500\ \mathrm{M}_\odot$

in which cells are refined or derefined according to the refinement/derefinement criterion mentioned previously. There is no hydrodynamics present in the meshrelax process and as such the gas is fixed until the process is complete.

The velocity of the gas is initialised to be the circular-velocity of the axisymmetric terms of the potential, $v_c = (R\,\partial\Phi_0/\partial R)^{1/2}$, which follows the same circular-velocity curve as Figure 4.1. The non-axisymmetric components of the bar and spiral arms are introduced linearly and gradually over the course of 150 Myr to avoid transients, as is customary in this type of simulations (e.g. Li et al., 2022), making use of the time-dependent `Evolving` potential framework of Agama.

4.4 Results

4.4.1 The gas response

In order to test kinematic estimates properly, the simulation box needs to be rotated such that the bar is in a similar position with respect to the Sun's position as it is for the Milky Way. For each simulation output, we rotate the system so that the angle between the bar major axis and the Sun-Galactic centre line is 28° (Bland-Hawthorn & Gerhard, 2016). The Sun-Galactic centre distance is assumed to be $R_0 = 8.179$ kpc (GRAVITY Collaboration et al., 2019). For each simulation we generate an lv diagram assuming the Sun moves with a velocity equal to its circular-velocity in the x direction, $v_x = v_c(R_0) = 229$ km s^{-1}, and has no other velocity components. We compare the structures in the resulting lv diagrams with the spiral arm tracks of Reid et al. (2016, 2019) and McClure-Griffiths et al. (2004), as illustrated in Figure 4.8. For the analysis presented in this Section, we select the system at 441 Myr. It is very similar to the observations in the lv diagram, and the simulation at this point has been advanced for long enough that the non-axisymmetric components of the potential have had enough time to interact with the gas. The resulting density maps can be found in Figure 4.9.

From Figure 4.8 we find clear peaks in lv diagram that are associated with the spiral arms generated from the underlying potential. The spiral arms generally trace the spiral arm tracks of McClure-Griffiths et al. (2004), Reid et al. (2016) and Reid et al. (2019) in the regions outwith the galactic centre ($|l| > 50°$). Towards the galactic centre, comparing the spiral arms becomes difficult due to the perturbations generated by the bar. Some features are match, however there are features present in the lv diagram that do not match with any track and vice versa.

Comparing the terminal velocities we find our simulation mostly fall within what is expected for the Milky Way, with the exception of two zones; one at $10° < l < 30°$ and

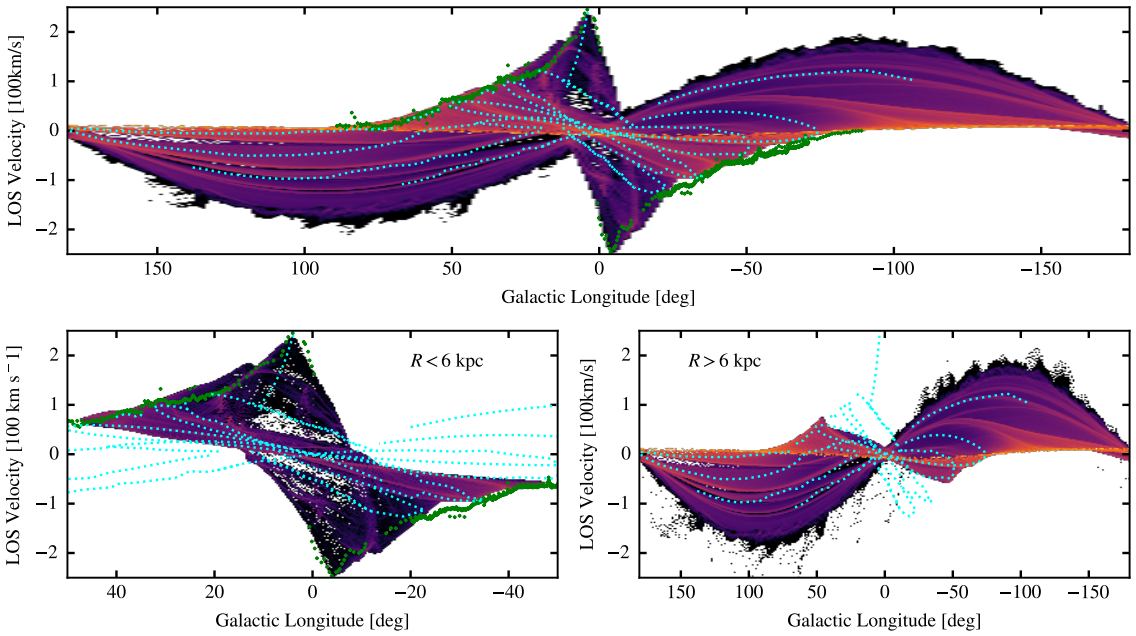

Figure 4.8. Longitude-velocity maps of the simulation observed from the Sun's position (placed at the origin of the overlayed coordinate system in Figure 4.9). The bar major axis is rotated by 28 degrees from the line of sight. Overlayed blue dashed lines are the spiral arm tracks of Reid et al. (2016, 2019) and McClure-Griffiths et al. (2004). The green points are the terminal velocities from H I and CO observations. *Top*: Full diagram. *Bottom*: Zoom in between $l = -60°$ & $+60°$ with the left plot only taking gas into account that lies within $R = 6$ kc from the centre and with the right one only considering gas further out.

the other at $-20° < l < -10°$. The LOS velocities are higher than that of the terminal velocities at these angles. This is a result of the steepness of the circular-velocity curve at around 3 kpc being relatively steep in comparison to similar potentials (See Li et al., 2022). This is a result of an overlap between the bar and stellar disk potentials in at this radii causing a slight overdensity at this point. Tracing these regions high LOS velocity regions to a position, these regions are located in the low density environment around the bar.

As expected, the potential of the bar strongly influences gas dynamics in the central region of the Galaxy. The gas here follows the typical x_1 orbits, a family of orbits elongated parallel to the major axis of the bar (Contopoulos & Grosbol, 1989), until it is shocked at the end of the bar, after which it flows inwards on nearly radial orbits. Eventually, the gas stabilises into x_2 orbits, forming a ring of material at 220 pc from the centre of the Galaxy. This ring is the equivalent of the Central Molecular Zone (CMZ) and is consistent with the larger end of estimates for the Milky Way's CMZ (e.g. Henshaw et al., 2023).

Outside of the bar region ($R > 5$ kpc), the gas forms a clear spiral pattern. It is rather complex and has two main components: a two-arm spiral caused by the rotation of the bar, and the four-arm structure created by the spiral component of the potential described in Section 4.2. These two pattern rotate at different angular speeds, $\Omega_{\rm bar} = -37.5$ km s^{-1} kpc^{-1} and $\Omega_{\rm spiral} = -22.5$ km s^{-1} kpc^{-1} respectively, so they periodically interfere with each other. We plot the polar decomposition of the density map in the bottom plot of Figure 4.9 to better illustrate the spiral patterns. Here, a straight line would be consistent with a logarithmic spiral. We observe two gradients of spiral structure: the underlying spiral arm structure from the potential (blue dotted), and an $m = 2$ spiral being generated by the bar (green dashed) with an estimated pitch angle of 6.5° near the OLR of the bar. We note that the pitch angle value of the bar-generated pattern depends on the sound speed of the gas, as can be understood from the dispersion relation of spiral density waves in the tight-winding limit (e.g. Binney & Tremaine, 2008). Whilst there are linear trends in the plot, there are deviations from the underlying spiral arm structure. These occur at the point where the two components intercept at $R \sim 11$ kpc and at around the spiral arm crossing point, $R_{\rm cross} = 9.64$ kpc, where the deviation is a bridging feature between the spiral arm and the bar induced spiral arm.

We extract the exact structure with the filament finding package FILFINDER (Koch & Rosolowsky, 2015). This package identifies structures from a 2D image using morphological techniques. Not only does the package provide the spines of the extracted structure, it also provides the masks of the extracted regions. We overlay the extracted

spines in light blue in the bottom plot of Figure 4.9 and we use the masks to contrast the density of the simulation in the $x - y$ projection (Figure 4.9, top).

4.4.2 Kinematic distance estimates

The kinematic distance is calculated based on the assumption of purely circular orbits within the Milky Way. First, a rotation curve $v_c(R)$ is assumed. Then the Galactocentric radius of a given object is calculated by:

$$R = R_0 \sin(l) \frac{v_c(R)}{v_0 \sin(l) + v_{\rm los}} \,, \tag{4.23}$$

where l is the Galactic longitude of the object, $v_{\rm los}$ is its line-of-sight velocity, and R_0 and v_0 are the Galactic radius and circular-velocity of the Sun, respectively. For consistency, we use the circular-velocity curve generated by our potential as our rotation curve, as shown in Figure 4.1. Because R appears on both sides of Equation (4.23), it is estimated through an iterative process.

The kinematic distance to the object is then obtained by

$$d_k = R_0 \cos l \pm \sqrt{R^2 - (R_0 \sin l)^2} \,, \tag{4.24}$$

It is possible for the kinematic distance estimate to return an undefined answer as a result of the argument inside the square root being less than zero. This occurs when

$$v_{\rm los}^2 > v_{\rm term}^2 - 2v_0(v_{\rm los} - v_{\rm term}) \sin l \,, \tag{4.25}$$

where $v_{\rm term}$ is the terminal velocity along a given Galactic longitude and is given by: (Burton & Gordon, 1978)

$$|v_{\rm term}| = v_c(R) - v_0 |\sin(l)|. \tag{4.26}$$

In other words, the kinematic distance is indefinite when the observed $v_{\rm los}$ is not possible (e.g. too high) under the assumed rotation curve $v_c(R)$. In this case, the argument of the square root of Equation (4.24) is set to zero, which is equivalent to placing the object at the tangent point for a given l, where $R = R_0 \sin(l)$. This is also equivalent to setting the velocity to the terminal velocity for a given l.

Equation (4.24) can give two answers when observing inside the solar circle, resulting in the well-known kinematic distance ambiguity. For the sake of simplicity, we resolve the ambiguity by selecting the kinematic distance closest to the true distance value. The first plot of Figure 4.10 of shows the kinematic distance map of of our simulation. The kinematic distance map is not a smooth distribution with increasing radius from the Sun. We find deviations from the true values (second part of Figure

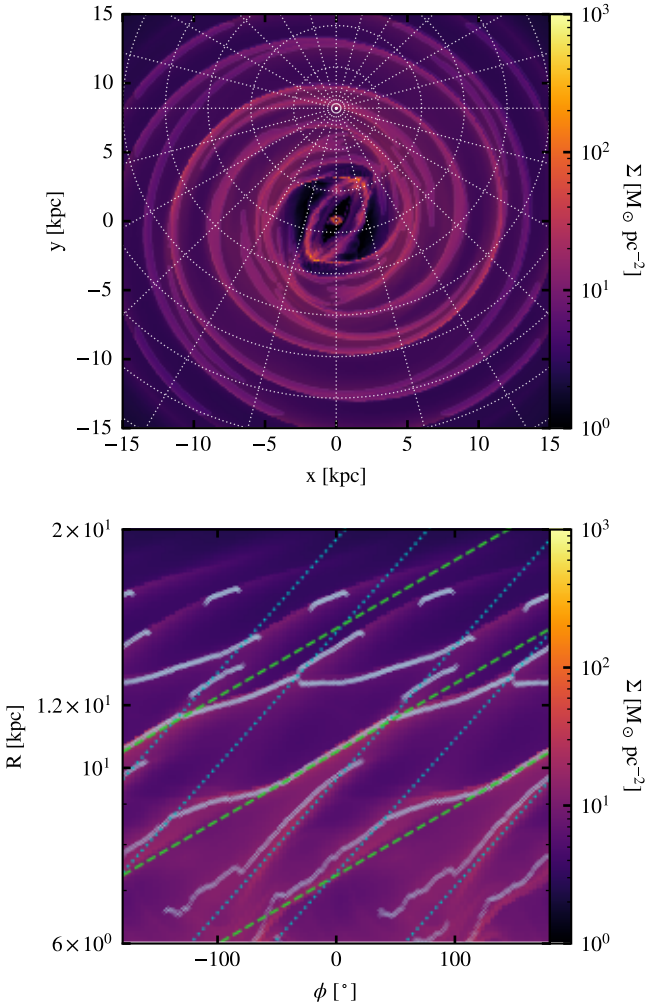

Figure 4.9. The top plot is the $x - y$ density projection of our simulation at $t = 441$ Myr with the mask of overdensities from FILFINDER highlighting the spiral structure. The bottom figure is the polar decomposition of the density map of the top figure focusing on the region with Galactocentric radius $6 < R < 20$ kpc. The blue dotted lines are the positions of the spiral arms according to the second half of Equation (4.17). The green dashed lines are the spiral arms generated by the rotation of the bar, with a pitch angle of 6.5° around the outer Lindblad resonance, $R = 10.14$ kpc. The light blue lines indicate the spiral arm pattern extracted with FILFINDER.

4.10) close to the perturbations caused by the spiral arms and the bar. We also observe quite large deviations close to $l = 0°$ and $l = 180°$. This arises due to trigonometric effects: as l tends towards $0°$ or $180°$, the value for the Galactic radius, R, obtained from Equation 4.23 becomes undefined as both $\sin(l)$ and $v_{\rm los}$ tend to 0. These deviations are highlighted better in the third plot of Figure 4.10, where we map the relative error between the kinematic distance and the true distance. What stands out is the large relative error in the solar neighbourhood close to the spiral arm perturbations. Large errors can also be observed at the end of the bar, where the gas flows on x_1 orbits.

To see if the kinematic distances tend to be over- or underestimated, we look at the probability density distribution of the relative kinematic distance error, $(d_k - d_{\rm true})/d_{\rm true}$, where $d_{\rm true}$ is the true distance to a given object. In Figure 4.11 we plot the distribution for a given annulus around the Sun to illustrate how true distance affects kinematic distance errors. For objects within 500 pc of the Sun, the kinematic distance estimate is highly unreliable and exhibits a bimodal error distribution. This bimodality peaks at $\sim -100\%$ and $\sim +75\%$. Beyond 500 pc from the Sun the distribution of errors becomes more centrally peaked at 0 with increasing radius. Kinematic distance errors less than -1 are a result of the kinematic distance being negative. These unphysical values are normally disregarded, however, we include them here in our analysis for completeness.

When computing kinematic distances, observers typically avoid lines of sight within $\pm 15°$ from the direction towards the Galactic centre and $\pm 20°$ of the anti-centre due to high errors in these line of sights. (e.g. Anderson et al., 2012; Balser et al., 2015; Wenger et al., 2018). As mentioned previously, the trigonometric effects as $l \to 0°$ or $180°$ can drastically impact the kinematic distance estimate. On top of this, the Galactic bar also impacts estimates towards the centre due to the high level of asymmetry in the potential.

To give a more conclusive idea about which lines of sight to avoid, we compute the absolute kinematic distance error and plot the median and absolute median deviation (MAD) as a function of Galactic longitude in Figure 4.12. The results are split into separate annuli around the Sun's position, as with Figure 4.11, showing that the error in the kinematic distance remains high at distances closer to the Sun with some variation with Galactic longitude. We define a line of sight of avoidance for an annulus as the line of sight where more than 20% of cells have an absolute kinematic distance error greater than 27%. Our choice of this value is motivated by the study of Wenger et al. (2018), who quantify the uncertainty in the kinematic distance inferred using the Brand & Blitz (1993) rotation curve (their method A) or the Reid et al. (2014) rotation curve (their method B) due to uncertainties in e.g. the solar Galactocentric radius and orbital

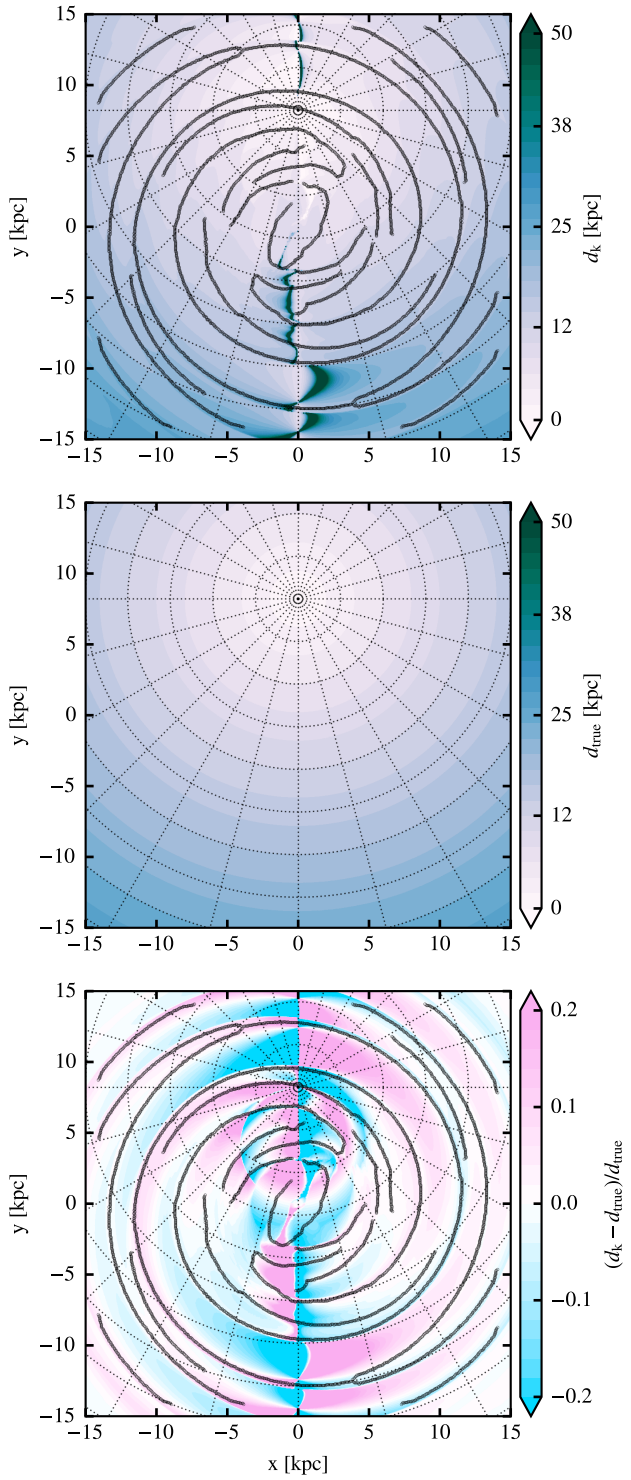

Figure 4.10. Estimated and real distance maps in the simulation. The black lines indicate the spiral arm pattern extracted with FILFINDER. The top plot shows the kinematic distance maps as estimated with Eq. (4.24). The middle plot is the map of the true distances to the gas cells. The relative error between the kinematic and true distance is shown in the bottom plot.

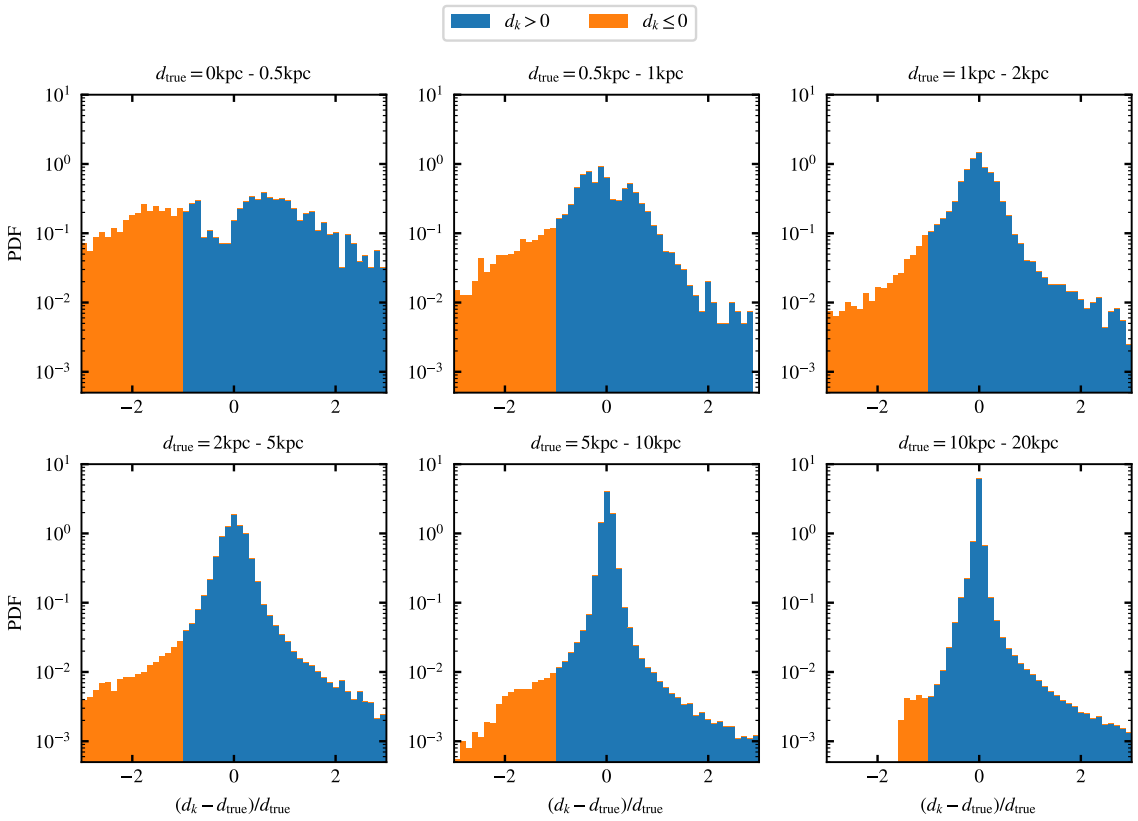

Figure 4.11. Distribution of relative kinematic distance error for different sampling annuli of true distances relative to the Sun's position. Here we represent relative errors that are ≤ -1 in orange, indicating where values are unphysical with zero or negative kinematic distance estimates.

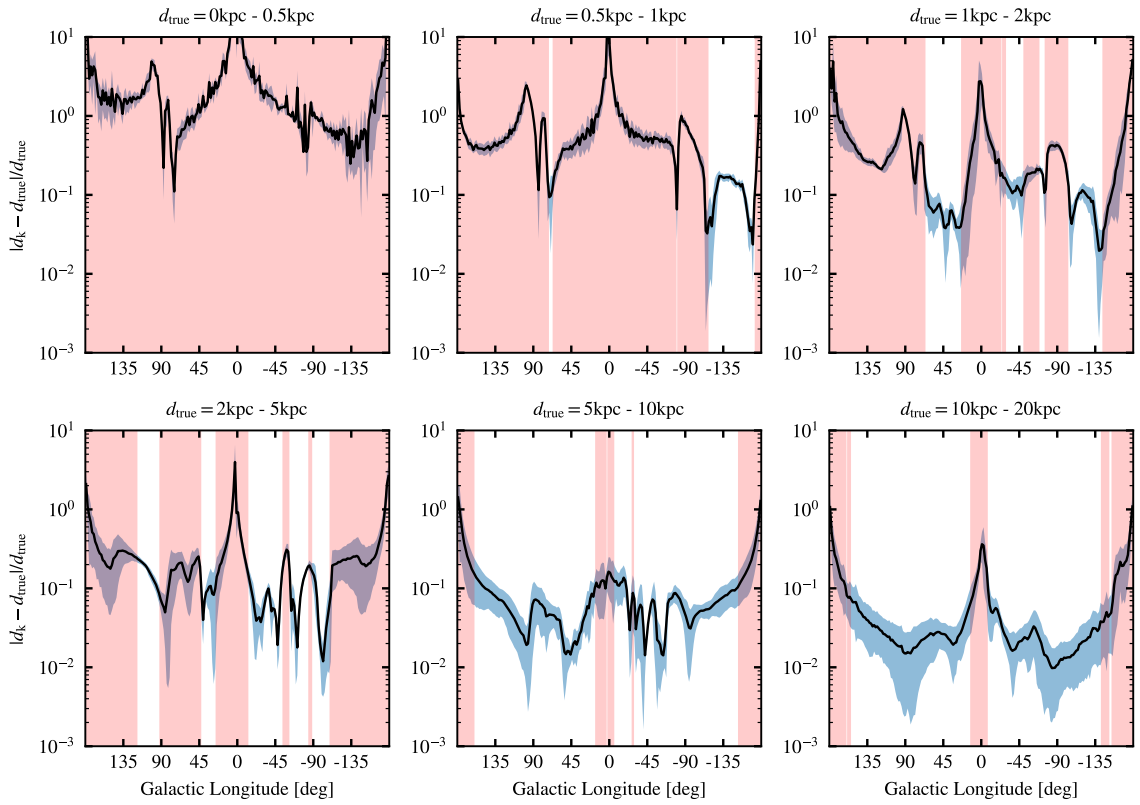

Figure 4.12. The black line represents the median absolute relative kinematic distance error along the line-of-sight of a given Galactic longitude. Each plot represents a sampling annulus centred on the Sun. The blue shaded region is the median absolute deviation (MAD) of the error. The red shaded regions represent the Galactic longitudes where more than 20% of the cells along the line-of-sight have a relative kinematic distance error of 27% or more.

velocity, the measured rotation curve, etc. The average absolute kinematic distance error they find when considering both models is 27%. For lines of sight and locations where the systematic error for most points is less than this value, the kinematic distance method should be reliable. On the other hand, if a large fraction of points have systematic errors that exceed this value, this is a good indication that the kinematic distance method will not provide reliable results.

The lines of sight that should be avoided are shown in red in Figure 4.12. For objects within 500 pc of the Sun, 99.5% of the full range of Galactic longitude should be avoided. This fraction remains above 56% out to 5 kpc, but drops to 14% and 16% for the $5-10$ kpc annulus and the $10-20$ kpc annulus, respectively. This suggests that the kinematic distance estimate is accurate for distances beyond 5 kpc from the Sun under our criterion for line of sight avoidance, but that for closer distances it should be used with great care.

4.4.3 Location of kinematic distance errors

So far we can see that velocity perturbations generated by the non-axisymmetric components of the potential can produce highly inaccurate kinematic distance estimates along most lines of sight for objects close to the Sun. This now poses the question: where can one reliably use kinematic distances?

Back in Figure 4.10 we show the map of kinematic distance errors of our simulation with the density peaks extracted with FILFINDER overlayed onto the maps. The peaks lie close to the regions of low value for the kinematic distance error. However, this only applies to the spiral arm features, i.e. peaks outside of the bar region, from inspection. To further analyse this, we split the Galaxy into two regions: the bar region ($R < 6\,\mathrm{kpc}$) and the disk region ($R \geq 6\,\mathrm{kpc}$).

Bar region

For the bar region, we employ the mask generated by FILFINDER to identify the overdensities from our simulations and applying them to the kinematic distance error map (Figure 4.10), splitting the data into overdense regions and underdense regions. We plot the PDF of each region, respectively, and compare their distributions (Figure 4.13).

From visual inspection, we see that both distributions peak at around 0, with the underdense regions' distribution slightly wider than the overdense regions. Since the distribution is non-Gaussian, we look at the difference between quantiles to understand the width of the distributions. The difference between the upper and lower 20% quantiles is 0.14 for overdense region, whilst it is wider with a value of 0.22 for the underdense region. Similarly, the values are 0.29 and 0.39 for the upper and lower 10% quantiles, and 0.50 and 0.61 for the 5% quantiles respectively. This suggests that outside of the overdense regions there is a higher probability of a large error and, by consequence, an increased probability of obtaining an incorrect distance via the kinematic distance method. Going from our analysis of the error as function Galactic longitude (Figure 4.12), this result is not too much of a surprise given that much of the bar's influence is lies within $l = \pm 30^\circ$ which is typically a line-of-sight of avoidance for all distances away from the Sun.

Disk region

As we have done previously, we split the kinematic distance maps of the disk region into spiral arm regions and interarm regions and plot the corresponding distributions of each. In this case we apply this to everything outside of $R = 6\,\mathrm{kpc}$.

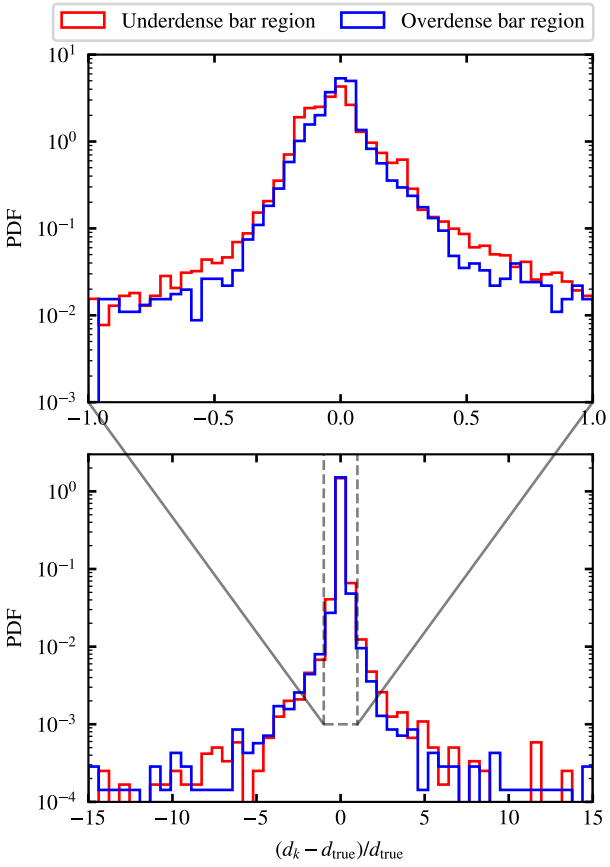

Figure 4.13. Probability distributions of the systematic kinematic distance errors within the overdensities in the bar region (blue) and the underdensities in the bar region (red).

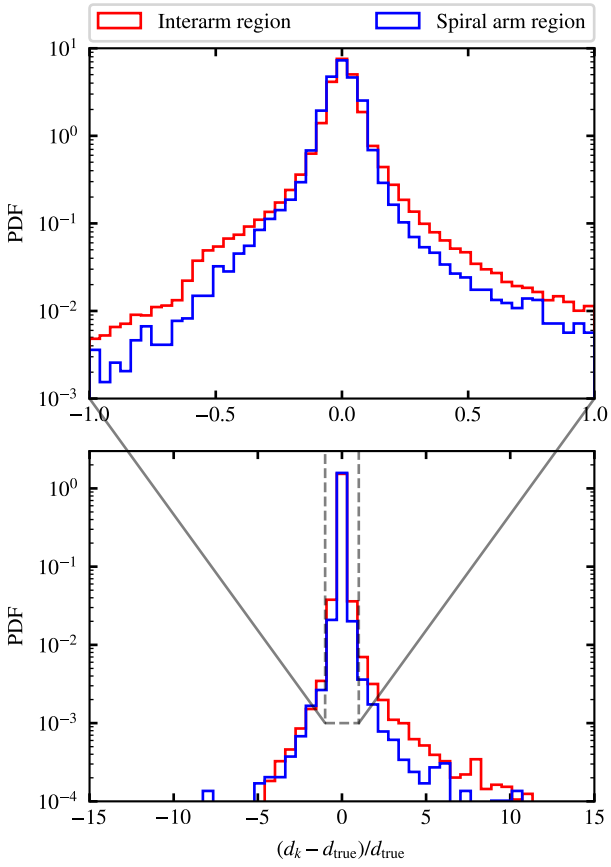

Figure 4.14. Probability distributions of the systematic kinematic distance errors within the spiral arm region (blue) and the interarm regions (red).

Table 4.4. Summarised values of the statistics between the different regions. Quantile difference indicates the difference between upper and lower percent quantile, for example 20% means the difference between the upper and lower 20% quantile.

Region	Median	Quantile difference		
		20%	10%	5%
Overdense bar	0.001	0.14	0.3	0.5
Underdense bar	-0.018	0.22	0.39	0.61
Spiral arms	0.001	0.1	0.17	0.26
Interarm	0.004	0.1	0.2	0.39

From Figure 4.14 we find similarly shaped distributions in the errors for the Galactic disk as we did for the bar region. Once again we have the distribution peaking at 0 for both spiral and interarm regions, with a a wider distribution in the interarm regions. Looking at the ranges between quantiles, the ranges are more similar between the spiral arm and interarm region. The difference between the upper and lower 20% quantiles is 0.1 for both regions. For the difference in the 10% quantiles the ranges are 0.17 and 0.2 for the spiral arm and interarm regions respectively. Similarly it is 0.26 and 0.39 for the 5% qunatile difference. Although the difference in the quantiles are similar between the regions, the interarm regions has a wider distribution. This indicates that the interarm regions of the Galaxy have a higher probability of an incorrect kinematic distance, similar to that for the underdense regions of the bar though with a lower probability of a larger associated error. The narrower distribution of errors of the spiral arm region is a rather reassuring fact, because it implies that the kinematic distance method is more reliable in the regions of the Galaxy where most of the dense gas and subsequent star-forming regions are found. We look into the dynamics causing this result in the subsequent subsection.

It should be noted that in both overdense regions there is not much skewness in the distribution and, as such, there is no clear way to indicate whether if the kinematic distance would be under- or overestimated. We summarise the statistics generated from the systematic kinematic distance error distributions in Table 4.4.

4.4.4 Relation to the velocity deviation

The key parameters that are needed for kinematic distance methods are the LOS velocity of the object and a rotation curve for the Milky Way. As mentioned previously, the Milky Way is not axisymmetric and as such there are deviations away from the rotation curve velocities. Quantifying the correlation between these deviations and the

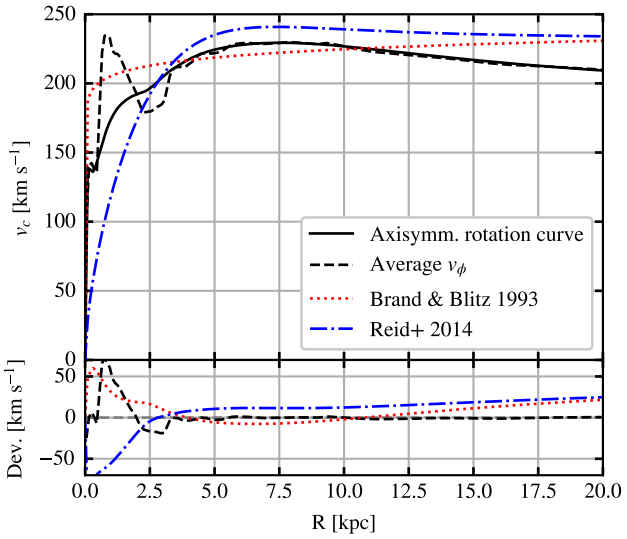

Figure 4.15. Comparison of rotation curve against the average azimuthal velocity (black solid and dashed line respectively). The red and blue lines are the rotation curve from Brand & Blitz (1993) and Reid et al. (2014).

systematic kinematic distance errors can give an insight into how the velocity impacts the kinematic distance estimates.

The deviations from rotation curve can be seen in the radial profile of the azimuthal velocity of the gas. We illustrate this in Figure 4.15 where in the inner most 3 kpc we observed deviations up to 70 km s^{-1}. Between 3 kpc and 10 kpc there are small deviations from the rotation curve, on the order of few km s^{-1}, due to perturbations of the spiral arms in our system. We include the rotation curve from Brand & Blitz (1993) and the universal rotation curve of Persic et al. (1996) with the updated parameter from Reid et al. (2014) as comparison to other rotation curves used in kinematic distance estimates.

We compute the line-of-sight velocity of our simulations and map it to the face down Milky Way view at the top of Figure 4.16. The non-axisymmetric perturbations of the potential are apparent here. Towards the bar region, we observe a sharp transition across the Galactic centre (as expected from the lv diagram of Figure 4.8), with perturbations of the spiral arms appearing as displacements in the contours in comparison to the middle plot of Figure 4.16; the LOS velocity maps for an axisymmetric potential. When we look at what we expect from an axisymmetric potential, the transition towards the Galactic centre is not as strong and the contours of the line-of-sight velocity towards the outer Galaxy are smoother. When we subtract the two maps, we find that the largest deviations occur at the bar region with differences on the order of 100 km s^{-1}. Outside the bar region we find the line-of-sight velocity difference to be

close to zero along the spiral arms of the Galaxy. Gas experiences an acceleration or deceleration as it flows into or out of the spiral arm, respectively as shown in Figure 4.17. This can cause shocks causing the gas to get denser as it leaves the potential minima, as in the case for two of our spiral arms. Additionally, the perturbations caused by the bar can also shock the gas and causes further perturbations. In our case, at around $R = R_0$, both the bar generated spiral and two of the spiral arms overlap creating large peaks in density. However, unlike the other two spiral arms, the peak in density for these occur just before passing the potential minima of the spiral arm potential.

All of this results in the largest deviations from the rotation curve to occur in the interarm regions which in turn causes shifts in the estimated kinematic distances, increasing their systematic error within these regions (see Figure 4.10).

Given how large deviations of the line-of-sight velocity occur in the same regions where the systematic kinematic distance errors are highest, we look at the correlation between the velocity deviation and the distance error. In Figure 4.18 we plot the 2D probability density function of the absolute values of the relative error against the velocity deviation from those expected for a pure axisymmetric potential and find a positive a correlation between the two parameters. This correlation can be described by a power-law with slope $\alpha = 0.92$.

4.5 Discussion

4.5.1 Implications

From our analysis, we find that kinematic distance estimates are most unreliable close to the Sun and along Galactic longitudes towards the Galactic (anti-)center. Additionally, there is a higher deviation within interarm regions than within spiral arms. This implies that clouds within underdense regions of the galaxy are more likely to have an incorrect distance estimate from the kinematic distance method.

An observational study carried out by Wenger et al. (2018) compared the distance estimates obtained by the parallax method to those obtained with the kinematic distance method. By treating the parallax distance as the true distance, they found an average distance deviation of $+20 \pm 40\%$ for their entire sample (see their Table 4). This suggests that the kinematic distances are systematically overestimated within their sample. Comparing to our work, we find that our distance estimates tend to only over- or underestimated by a few percent on average but with a significantly large spread within our systematic errors. Since our simulations do need contain any additional velocity perturbations, such as turbulence, the errors we find are a lower bound estimate.

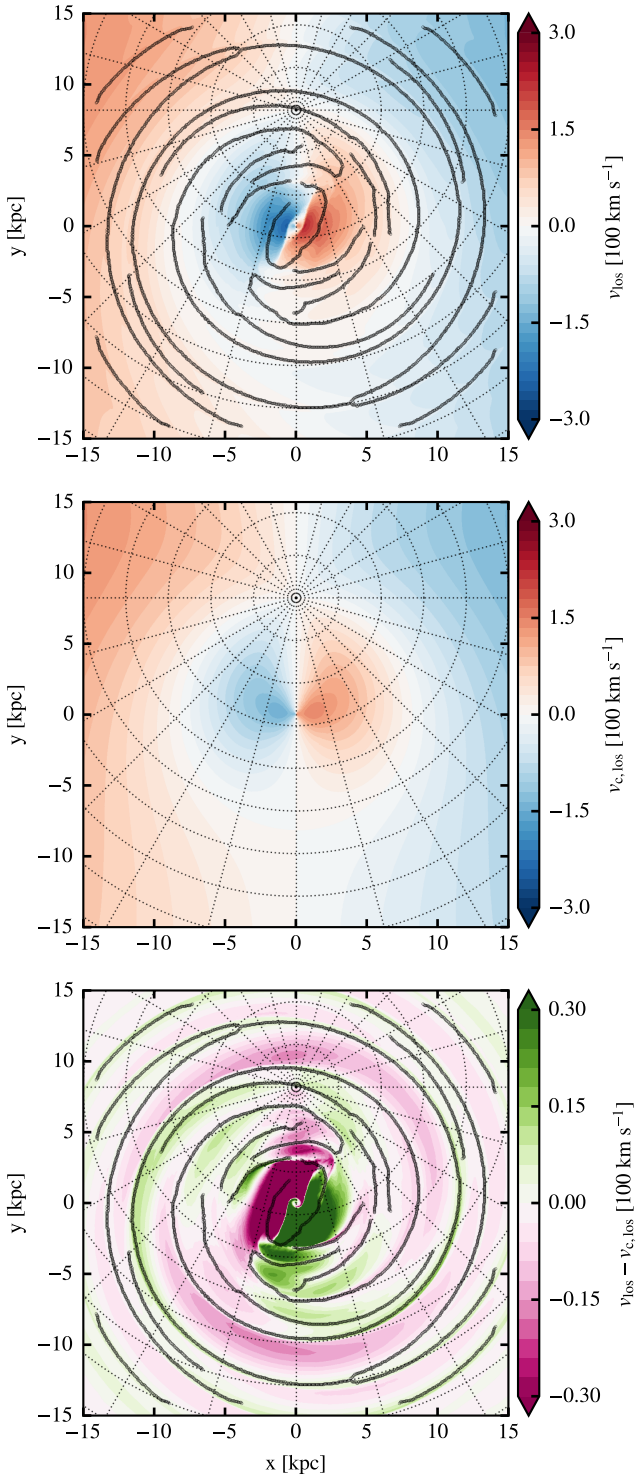

Figure 4.16. The top plot illustrates LOS velocity map of the simulation. Similarly, the middle plot shows the map of the LOS velocity derived from the base axisymmetric potential. The last plot shows the difference between simulation and axisymmetric LOS velocities; top plot minus the middle plot.

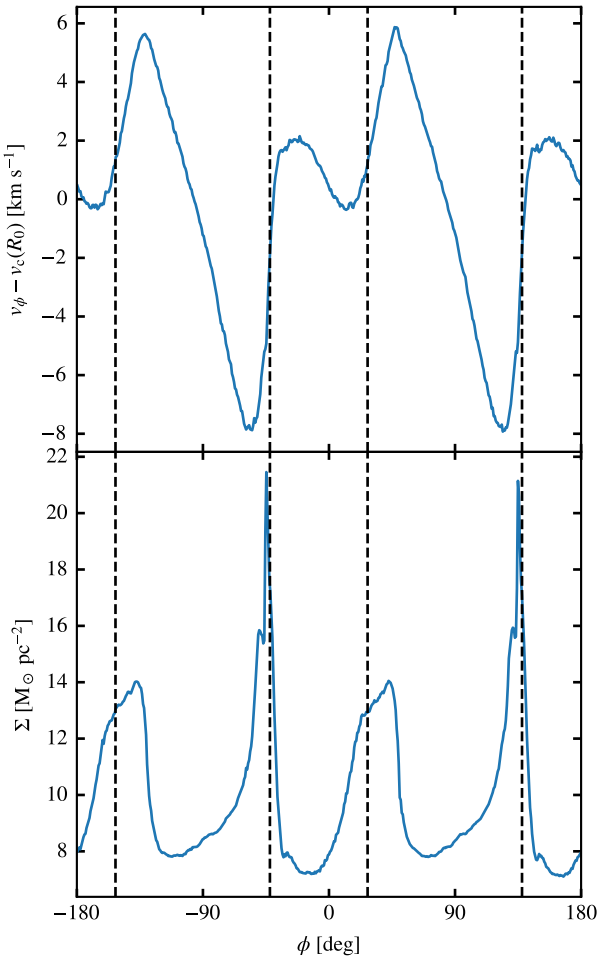

Figure 4.17. The azimuthal profile of the difference between azimuthal and circular velocity (top) and the surface density (bottom) near solar circle, $R = 8.18$ kpc. The vertical dashed lines are the potential minima of the underlying spiral arm potential. Rotation of the system is from right to left.

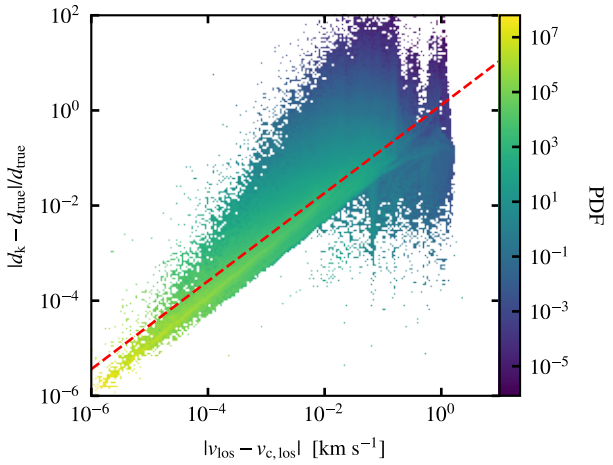

Figure 4.18. 2D probability density function of the relative error in the kinematic distance against the difference between the simulation and axisymmetric LOS velocities. The red dashed line is a power law with slope of 0.92.

Table 4.5. Kinematic distances and errors of five sources.

Source	l (degrees)	$d_p^\dagger$ (kpc)	$d_k^\dagger$ (kpc)	d_k (kpc)	$(d_k^\dagger - d_p^\dagger)/d_p^\dagger$	$(d_k - d_p^\dagger)/d_p^\dagger$
M17	15.03	1.97	2.33	1.10	0.18	-0.44
W49N	44.20	10.93	11.52	11.15	0.05	0.02
NML Cyg	80.80	1.6	1.33	1.32	-0.17	-0.18
AFGL 2789	94.60	3.49	5.48	3.21	0.57	-0.08
G240.31+00.07	-163.84	7.11	5.75	9.17	-0.19	0.29

†Distance from Wenger et al. (2018).

To help give an idea as to what implications this has for the observations, we generate a longitude-distance map of our kinematic distance errors in Figure 4.19. We overplot some of the known sources of Wenger et al. (2018) to give an indication as to where real sources would lie on the map, treating parallax distance estimates as true distances.

When comparing the errors we calculate to those obtained from observations (Choi et al., 2014; Wenger et al., 2018), assuming the parallax distance d_p as the true distance, we find that in some instances the errors are similar, within a factor of two. However, in others they are vastly different. For example, the error associated with AFGL 2789 has an error on the order of -8% in our system but is around $\sim 50\%$ from observations. AFGL 2789 is located within the Perseus spiral arm (Oh et al., 2010) which is consistent with our finding that objects within spiral arms tend to have lower errors. However, the observational result would indicate that the object is located more towards an interarm region.

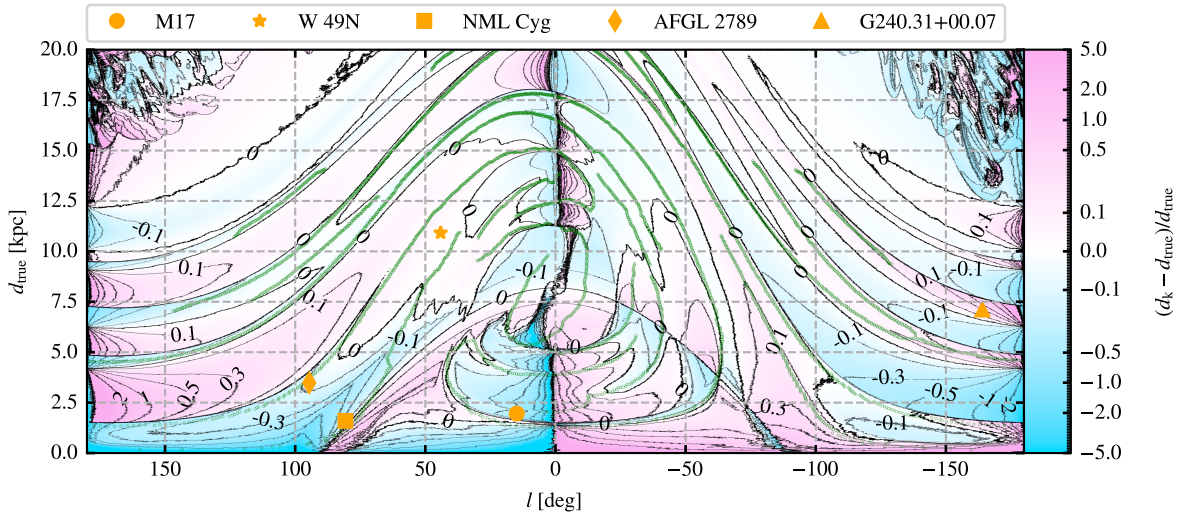

Figure 4.19. Map of the kinematic distance error as a function of Galactic longitude and true distance. The contours are placed at $0, \pm 0.1, \pm 0.3, \pm 0.5, \pm 1, \pm 1.5$ and ± 2. The green lines indicate the spiral arms extracted with FILFINDER. Overplotted in orange are a selection of known sources using parallax distances as true distances (Wenger et al., 2018).

4.5.2 Caveats

There are a few limitations to bear in mind when considering the maps of kinematic distance errors derived from our simulations. First, as mentioned in Sect. 4.3, the simulations performed here are 2D dimensional. This corresponds to the assumption that the gas in our simulation is integrated vertically, along the z-axis. The acceleration of the gas due to the potential is computed as if the gas lies in the midplane of the Galaxy ($z = 0$). This completely neglects the 3D structure of the Galaxy and vertical motions present within the gas. This additional component will impose changes to Equations (4.23) and (4.24) with the introduction of additional $\cos(b)$ terms. With the perturbations induced by the potential, the gas can also experience changes in the z-component of the velocity as it travels in and out of a spiral arm. This will impact the LOS velocity of the gas and the resulting kinematic distance. However, quantifying the size of this effect is beyond the scope of this chapter.

Second, the simulations presented here are idealised with only isothermal hydrodynamics and an external galactic potential. We note that the adopted value of $c_{\mathrm{s}} = 10\,\mathrm{km\,s^{-1}}$ implies that we use an effective sound speed, which includes a strong turbulent component providing additional support of the gas disk (Mac Low & Klessen, 2004; Krumholz & McKee, 2005b; McKee & Ostriker, 2007; Klessen & Glover, 2016). Besides a self-consistent treatment of stellar feedback, more realistic models should include

time-dependent chemistry (e.g. Glover et al., 2010a). Altogether, we would expect the sound speed to vary across the Galaxy, causing the structure of the Galaxy to alter. Indeed, parameter studies with different sound speeds have shown that spiral arms tend to get wider with increasing c_s (Li et al., 2022), whereas the size of the CMZ becomes smaller (Sormani et al., 2015a, 2023).

The spiral arm potential we present in this chapter is not an exact match to the spiral arm pattern of the Milky Way. It is well noted that the spiral arm shape of the Milky Way is not regular, with differences in phase angles between spiral arms and pitch angle changes along the spiral arm (see Reid et al., 2016, 2019). These irregularities are hard to model when constructing the potential so approximations are required. Here, we keep the pitch angle of the spiral arms the same and try to account for the change in phase angle with the two pairs of Gaussian shaped spiral arms (see Sect. 4.2.1). Additionally, perturbations generated by the interaction with orbiting satellite galaxies can impact the velocity space of the Galaxy, creating wave-like oscillations throughout the Galaxy (Khanna et al., 2019). These differences in structure will make some of the kinematic distance estimates in our simulation very different from what they would be for the Milky Way, as illustrated in Section 4.5.1.

Turbulent motions induced by physics such as self-gravity, stellar and supernova feedback would contribute to the velocity dispersion of the system. The effects of self-gravity can add an additional $\sim 2-5$ km s^{-1} to the velocity dispersion for axisymmetric systems but can be as high as ~ 10 km s^{-1} for non-axisymmetric systems such as the one presented in this chapter (Wada et al., 2002). Despite this, supernova feedback is believed to give the largest contributions to the velocity dispersion on large scales, potentially producing a velocity dispersion of as much as ~ 10 km s^{-1} across hundreds of parsecs Lu et al. (2020). This can result in the line-of-sight velocity deviating from the values derived here by a similar amount, causing kinematic distance estimates to deviate further from the true value.

Kinematics distance are normally computed with one of two Galaxy rotation models, the rotation curve of Brand & Blitz (1993) and the universal rotation curve of Persic et al. (1996) with updated parameters from Reid et al. (2014). Both of these rotation curves have been obtained from the gas within the Milky Way; the former making use of HII regions and HI tangent point data, whilst the latter makes use of maser parallaxes. We do see differences between the rotation curves presented in these papers and our values, since our potential is modelled based on the rotation curves from stellar data, as shown in Figure 4.15 (Mróz et al., 2019; Eilers et al., 2019). There is a difference on the order of up to ~ 10 km s^{-1} between the rotation curve within the disk of the Galaxy, and larger deviations within the inner most 3 kpc. An investigation into how

these differences in the standard rotation curves can impact kinematic distance is beyond the scope of this thesis, but does warrant future investigation.

4.6 Conclusions

In this chapter, we have presented a realistic analytic potential for the Milky Way. It contains density profiles for all major mass component of the Galaxy. These are the supermassive black hole in the very center, the nuclear stellar cluster and nuclear stellar disk, the Galactic bar, the Galactic disk, which we split into axisymmetric components for field stars and gas and a spiral arm component for the field stars only, and finally an extended dark matter halo that dominates the potential at large distances. These are introduced and fitted to the observational constraints, such as the rotation curve and the terminal velocities, in Section 4.2.

We also described how the new analytic potential is implemented in the moving-mesh code Arepo within the Agama framework of potential libraries, as outlined in detail in Section 4.3. We made use of 2D hydrodynamic simulations to investigate how robustly the axisymmetric assumption holds for kinematic distance estimates. For this, we place an observer at $R_0 = 8.178$ kpc with the bar angled at 28°, generate kinematic distance estimates to each of the gas cells present within our simulations and compute the systematic errors for each, $(d_k - d_{\rm true})/d_{\rm true}$. As discussed in Section 4.4 we found that the errors are high close to the Sun, with values reaching >50% on average for any sources with 1 kpc. Along with proximity, we found that errors also reach these values when viewing towards the Galactic centre and anti-centre, $l = 0°$ and $l = 180°$, respectively.

When considering both Galactic longitude and distance, there are certain lines-of-sight that result in higher errors in addition to those previously mentioned for specific distance ranges. We identify these regions as zones of avoidance for the application of the kinematic distance method. We also compare our results with the distance estimates of some well-studied molecular clouds and find in general good agreement (Section 4.5).

In summary, the extraction of the velocity perturbations in our simulation has allowed us to determine what impact the potential has on systematic errors in the kinematic distance estimate. We find that within the spiral arms of the Galaxy, the kinematic distance errors are low as the gas lies within the local potential minima. Consequently, the line-of-sight velocity of the gas is close to what is expected for the axisymmetric version of our potential. We expect clouds within the spiral arms of the Milky Way to have low systematic kinematic distance errors. Conversely, the interarm regions present the largest deviation in both the kinematic distance and the line-of-sight velocity for

a given Galactic radius. This is caused by the gas being sped up or slowed down as it travels into or out of the spiral arm. Additionally, we discovered a power law relation between the systematic kinematic distance error and the difference between the line-of-sight velocity and the projected circular-velocity.

We conclude that the assumption of axisymmetry for the kinematic distance method can result in large systematic deviations depending on where a source is situated within the Milky Way. These deviations can alter derived values that depend on distance and, as such, the corresponding systematic errors should be accounted for in these derived values.

The interface between Agama and Arepo/Gadget-4 codes, along with the scripts for constructing the potential from Section 4.2 and for running N-body simulations with these codes in the external potential, are included in the Agama repository[1].

[1] https://github.com/GalacticDynamics-Oxford/Agama

Chapter 5

Conclusion and future plans

"Words become a song and once again run through the world for your sake. Entrust your intentions to that voice and, right now, thoughts and feelings will resound."

—Ryo, *ODDS&ENDS*

Throughout this thesis we have explored the topic of dynamics within the interstellar medium. Here, we have made use of hydryodynamical simulations throughout the thesis to test how motions can affect quantities of the ISM.

In chapter 1 we provided an overview of the ISM, detailing the thermal phases present and thermo-chemistry involved in H_2 formation. Following that we discuss the formation, destruction and properties of giant molecular clouds, and providing details on the subsequent star formation after the collapse of GMCs. In that chapter we zoom out to the Milky Way and galaxies as whole with an overview of galactic dynamics. We discuss the gravitational forces at play, how the potential is constrained from observations, and the analytic models used by dynamicists when modelling galaxies.

We introduce the numerical techniques that were used as a part of this thesis in chapter 2. The first part of this chapter was dedicated to numerical hydrodynamics. We provided a brief overview of the physics involved in hydrodynamics as well as the common approaches to solving the hydrodynamic equations, both in Eularian and Lagrangian reference frames. In that section we introduce the cosmological MHD code Arepo, a quasi-Lagrangian moving-mesh code that we make use of for our cloud and galaxy simulations.

Also in chapter 2, we look into how gravity is accounted for in simulations, exploring the numerical methods used to compute gravitational forces within simulations, including direct N-body, tree-code, particle mesh and potential expansions. The gravi-

tational dynamics library AGAMA was introduced in this section, detailing how potentials are computed from density distributions. The interface between AGAMA and AREPO was discussed in that section.

Chapter 3 introduced the topic of cloud-cloud collisions. We perform a series of MHD simulations of colliding GMCs, performing a parameter space study in the process. A range of velocities, magnetic field inclinations with respect to the collision axis, and effective resolution are explored. We find that overall, collisions increase the SFR by factor of $\sim 2-3$ in comparison to our stationary simulation. We observe an earlier onset of star formation within these clouds in our simulations with higher collisional velocity, when the initial magnetic field orientation is parallel to the direction of the collision, and when the resolution of the simulation is lowered. The difference between the earliest to latest onset of star formation is on the order of a few freefall times of a dense clump, $\Delta t = 0.7$ Myr.

When looking at the mean virial parameter for dense gas within our simulation, we find that the virial parameter increases with collisional velocity which is consistent with the increase of turbulent motions within the gas as well as tangling of the magnetic field within the simulation. The variation in magnetic field inclination has little effect on the virial parameter. When we investigate the alignment between magnetic and velocity fields, we find the fields align in the lower density medium $n \sim 10^3 - 10^4$ cm^{-3} and become increasingly perpendicular with higher densities. This is consistent with the idea of gravitational collapse compressing magnetic field lines. Lastly we compare our SFRs to those of similar simulations in the literature, with a slight focus on the order of magnitude increase observed by Wu et al. (2017). We find that star formation protocols that account for the boundness of gas, like in our simulations, are in agreement with the factor of $\sim 2-3$ SFR increase.

In chapter 4 we look at the Milky Way's ISM at the scale of the Galaxy itself and test the valditiy of kinematic distance estimates. We construct a new analytic potential for the Milky Way, inclusive of non-axisymmetric components of the Galactic bar and spiral arms. The potential is generated from a mix of existing models and parameterising density distributions to quantities derived from observations (such as rotation curves and mass profiles). We initialise the potential with the framework present in AGAMA. We perform a simple 2D isothermal hydrodynamical simulation of the Galactic disk with only the potential of the Galaxy being the additional physics present in the simulation.

From our simulations we obtain structure in lv-diagrams comparable to the spiral arm imprint on the observed lv-diagrams. By placing an observer at solar circle, $R_0 = 8.179$ kpc, we compute the kinematic distance to each gas cell within our simulation.

The kinematic distance approach works on the crucial assumption that gas within the Milky Way moves on circular orbits. However, with the introduction of a triaxial bar and bisymmetric spiral arms, we find that the kinematic distances become unreliable in some part of the Galaxy. We define galactic longitudes l where the kinematic distance is unreliable for a given distance range (referred to as a zone of avoidance). These typically are towards the Galactic centre and anti-centre due to trigonometric effects, however additional zones appear the closer a gas cell is to the Sun's position. For an object less than 1 kpc away, the kinematic distance estimate is highly unreliable. The structure of the ISM also has an impact which correlates with the accuracy of kinematic distance estimates. Gas lying within overdensities generated by the bar and spiral arms often have more accurate kinematic distances in comparison to underdense regions (like the interarm region). We also find a correlation between the kinematic distance error and the deviation of the projected line-of-sight velocity from circular motion, following a power law with power $\alpha = 0.92$. Finally we compare our results to some observed sources present in (Wenger et al., 2018), identifying how the kinematic distance errors differ between using our potential and the Milky Way itself.

Looking forward, the simulations explored in this thesis provide a starting point for future work to be carried out, if not already so. As mentioned in chapter 3, the densities reached by cloud-cloud collisions can allow for high-mass stars to for; a technically challenging process due to the large luminosities present with their formation (Takahira et al., 2014; Balfour et al., 2015; Motte et al., 2018). Due to the scales involved in our simulations, we are unable to resolve the formation of individual stars, however the clumps present can provide the initial conditions for simulations at smaller scales. By extracting and averaging densities, velocity and magnetic fields radially, a simple set of initial conditions can be provided for such follow up simulations (Oliva et al. in prep.).

The potential developed in chapter 4 can be used as an external potential for much more complicated simulations, including physics such as self-gravity, stellar and supernova feedback, magnetic fields and cosmic rays. Under the ECOGAL collaboration the potential developed is currently being used to explore such simulations. One of the papers will explore if the external potential has any consequence on the structure of the ISM when in the presence of self-gravity (Göller et al. in prep.), whilst the another explores the how cosmic rays are distributed in the Galaxy under the influence of the potential (Kjellgren et al. in prep.) We hope that the potential developed will continue to be used, and the kinematic distance error maps developed chapter 4 will allow for observers to account for systematic errors when using the kinematic distance method.

Appendix A

Additional information for Chapter 3

A.1 Chemical network

The reactions included in our chemical network are summarized in Tables A.1 and A.2. Our network is based on the one presented by Gong et al. (2017; hereafter, G17), but also includes several reactions not included in their network, denoted in the tables as "Not in G17". In addition, for some reactions we have adopted a different rate coefficient from the one listed in G17; these are also indicated in the Table, with the note "Different rate". Reactions with no attached note are treated exactly the same as in G17. Below, we discuss the rationale for the differences between our network and the original G17 network. For the most part, these differences are to make the network more robust when applied to physical conditions outside of the range considered by G17 and have little impact on its behaviour in the typical photodissociation region (PDR) conditions that were the main focus of their study.

Table A.1. List of collisional chemical reactions included in our chemical network

No.	Reaction	Notes	Refs.
1	$H + e^- \rightarrow H^+ + e^- + e^-$		Janev et al. (1987)
2	$H^+ + e \rightarrow H + \gamma$		Ferland et al. (1992)
3	$He^+ + H_2 \rightarrow H_2^+ + He$		Barlow (1984)
4	$He^+ + H_2 \rightarrow H^+ + H + He$		Barlow (1984)
5	$H_2 + e^- \rightarrow H + H + e^-$	Not in G17	Trevisan & Tennyson (2002)
6	$H_2 + H \rightarrow H + H + H$	Different rate	Mac Low & Shull (1986), Lepp & Shull (1983), Martin et al. (1996)

Continued on next page

Table A.1 – continued from previous page

No.	Reaction	Notes	Ref.
7	$H_2 + H_2 \rightarrow H + H + H_2$	Different rate	Martin et al. (1998), Jacobs et al. (1967)
8	$H_2^+ + H_2 \rightarrow H_3^+ + H$	Different rate	Linder et al. (1995)
9	$H_2^+ + H \rightarrow H_2 + H^+$		Karpas et al. (1979)
10	$H_3^+ + e^- \rightarrow H + H + H$		McCall et al. (2004)
11	$H_3^+ + e^- \rightarrow H_2 + H$		McCall et al. (2004)
12	$He + e^- \rightarrow He^+ + e^- + e^-$	Not in G17	Janev et al. (1987)
13	$He^+ + e^- \rightarrow He + \gamma$	Different rate	Hummer & Storey (1998), Badnell (2006)
14	$C^+ + H_2 \rightarrow CH_x + H$		Wakelam et al. (2010), Gong et al. (2017)
15	$C^+ + H_2 + e^- \rightarrow C + H + H$		Wakelam et al. (2010), Gong et al. (2017)
16	$C + H_2 \rightarrow CH_x + \gamma$	Not in G17	Prasad & Huntress (1980)
17	$C + H_3^+ \rightarrow CH_x + H_2$		Vissapragada et al. (2016)
18	$C^+ + e^- \rightarrow C + \gamma$	Different rate	Badnell (2006), Badnell et al. (2003)
19	$C + e^- \rightarrow C^+ + e^- + e^-$	Not in G17	Voronov (1997)
20	$O^+ + H \rightarrow O + H^+$		Stancil et al. (1999)
21	$O + H^+ \rightarrow O^+ + H$		Stancil et al. (1999)
22	$O^+ + H_2 \rightarrow OH_x + H$		Gong et al. (2017)
23	$O^+ + H_2 + e \rightarrow O + H + H$		Gong et al. (2017)
24	$O + H_3^+ \rightarrow OH_x + H_2$		Stancil et al. (1999)
25	$O + H_3^+ + e^- \rightarrow H_2 + O + H$		Stancil et al. (1999)
26	$C^+ + OH_x \rightarrow HCO^+$		Gong et al. (2017)
27	$C + OH_x \rightarrow CO + H$		Zanchet et al. (2009)
28	$CH_x + He^+ \rightarrow C^+ + He + H$	Not in G17	Prasad & Huntress (1980), Tsang & Hampson (1986)
29	$CH_x + H \rightarrow H_2 + C$		Wakelam et al. (2010)
30	$CH_x + O \rightarrow CO + H$		Wakelam et al. (2010)
31	$OH_x + H \rightarrow O + H_2$	Not in G17	Tsang & Hampson (1986), Tsang & Hampson (1986)
32	$OH_x + O \rightarrow O + O + H$		Carty et al. (2006)
33	$OH_x + He^+ \rightarrow O^+ + He + H$		Wakelam et al. (2010)

Continued on next page

Table A.1 – continued from previous page

No.	Reaction	Notes	Ref.
34	$CO + H_3^+ \rightarrow HCO^+ + H_2$		Kim et al. (1975)
35	$CO + He^+ \rightarrow C^+ + O + He$	Different rate	Petuchowski et al. (1989)
36	$CO + H \rightarrow C + OH_x$	Not in G17	Mitchell (1984)
37	$HCO^+ + e^- \rightarrow OH_x + C$	Not in G17	Geppert et al. (2005)
38	$HCO^+ + e^- \rightarrow CO + H$		Geppert et al. (2005)
39	$Si^+ + e^- \rightarrow Si + \gamma$	Different rate	Nahar (2000)
40	$Si + e^- \rightarrow Si^+ + e^- + e^-$	Not in G17	Voronov (1997)

Table A.2. List of grain surface, cosmic ray and photochemical reactions included in our chemical network

No.	Reaction	Notes	Refs.
41	$H + H + gr \rightarrow H_2 + gr$	Different rate	Hollenbach & McKee (1979)
42	$H^+ + e^- + gr \rightarrow H + gr$	Different rate	Weingartner & Draine (2001)
43	$C^+ + e^- + gr \rightarrow C + gr$	Different rate	Weingartner & Draine (2001)
44	$He^+ + e^- + gr \rightarrow He + gr$	Different rate	Weingartner & Draine (2001)
45	$Si^+ + e^- + gr \rightarrow Si + gr$	Different rate	Weingartner & Draine (2001)
46	$H + cr \rightarrow H^+ + e^-$		Glassgold & Langer (1974)
47	$H_2 + cr \rightarrow H_2^+ + e^-$		Glassgold & Langer (1974)
48	$H_2 + cr \rightarrow H + H^+ + e^-$	Not in G17	McElroy et al. (2013)
49	$H_2 + cr \rightarrow H + H$	Not in G17	McElroy et al. (2013)
50	$He + cr \rightarrow He^+ + e^-$		McElroy et al. (2013)
51	$C + cr \rightarrow C^+ + e^-$		McElroy et al. (2013)
52	$CO + cr + H \rightarrow HCO^+ + e^-$		Gong et al. (2017)
53	$C + \gamma_{cr} \rightarrow C^+ + e^-$		Heays et al. (2017)
54	$CO + \gamma_{cr} \rightarrow C^+ + e^-$		Heays et al. (2017)
55	$Si + \gamma_{cr} \rightarrow Si^+ + e^-$		Heays et al. (2017)
56	$C + \gamma \rightarrow C^+ + e^-$		Heays et al. (2017)
57	$CH_x + \gamma \rightarrow C + H$		Gong et al. (2017),Heays et al. (2017)
58	$CO + \gamma \rightarrow C + O$		Heays et al. (2017)
59	$OH_x + \gamma \rightarrow O + H$		Gong et al. (2017),Heays et al. (2017)
60	$Si + \gamma \rightarrow Si^+ + e^-$		van Dishoeck (1988)

Continued on next page

Table A.2 – continued from previous page

No.	Reaction	Notes	Ref.
61	$H_2 + \gamma \rightarrow H + H$		Draine & Bertoldi (1996)

The primary cosmic ray ionization rate of atomic hydrogen is a free parameter in our chemical model and the value we select for this in our simulations is discussed in the main text. The total (primary plus secondary) rate for H (reaction 46), as well as the total cosmic ray ionization rates of H_2, He, C, CO and Si (reactions 47–55) are scaled relative to this value using scaling factors derived from the cited references.

Reactions in our network that are not in G17

Reactions 5, 12, 19 & 40

These reactions – the collisional dissociation of H_2 by electrons and the collisional ionisation of He, C and Si – were neglected by G17 because they are unimportant at typical PDR temperatures. However, they can become important in hot shocked gas with $T \gg 10^4$ K and we include them to ensure that the chemical network behaves reasonably at these high temperatures.

Reaction 16

The formation of CH_x – a pseudo-molecule that represents light hydrocarbons such as CH, CH_2, CH^+ etc. – by radiative association of atomic carbon and H_2 is neglected by G17 because it is a slow process and in typical Milky Way conditions is unimportant compared to CH_x formation via the reaction of C and H_3^+ (reaction 17). However, the abundance of H_3^+, and hence the rate of reaction 17, depends sensitively on the cosmic ray ionisation rate, and so reaction 16 can become important in conditions where this is much smaller than the typical Milky Way value.

Reaction 28

In neutral gas, this reaction is unimportant compared to reaction 29. It is included here to ensure that an appropriate loss route exists for CH_x in very highly ionized gas. For the rate coefficient, we use the value given by McElroy et al. (2013) for the reaction

$$CH + He^+ \rightarrow C^+ + He + H,$$

which comes originally from Prasad & Huntress (1980).

Reaction 31

This reaction is unimportant compared to reaction 32 at temperatures lower than 500 K, but quickly becomes dominant at higher temperatures, given a sufficient supply of hydrogen atoms. It is therefore not important in typical PDR conditions but can become important in shocks. For the rate coefficient, we adopt the value given by McElroy et al. (2013) for the reaction

$$\mathrm{OH} + \mathrm{H} \rightarrow \mathrm{O} + \mathrm{H_2},$$

which is based on Tsang & Hampson (1986).

Reaction 36

This reaction has a substantial activation energy ($E/k \sim 78000$ K) and is therefore unimportant in typical PDR conditions. However, it can become important in hot, shocked gas. In particular, we have found that if strong shocks occur in gas with high A_V, CO can persist in the gas up to artificially high temperatures of $> 10^4$ K if this reaction is not included.

Reaction 37

As G17 note in their appendix A, the destruction of $\mathrm{HCO^+}$ is dominated by the reaction $\mathrm{HCO^+ + e^- \rightarrow CO + H}$ (reaction 38 above). However, although CO and H are the most likely products of the dissociative recombination of $\mathrm{HCO^+}$, roughly 8% of the time this process instead yields C and OH (Geppert et al., 2005). We include this outcome here for completeness.

Reactions 48 & 49

Although interactions between high energy cosmic rays and $\mathrm{H_2}$ molecules primarily produce $\mathrm{H_2^+}$ ions (reaction 47), a small fraction of the time the outcome can instead be a hydrogen atom, a proton and an electron (reaction 48) or two hydrogen atoms (reaction 49). These outcomes were neglected by G17 but we include them here for completeness.

Reactions with different rate coefficients

Reactions 6 & 7

We use the same low density limits for the rates of these reactions as in G17, and the same expression for the H_2 critical density. However, we use slightly different expressions for the high density limits: G17 follow Lepp & Shull (1983) and Shapiro & Kang (1987) for reactions 6 and 7, respectively, whereas we use the expression given by Martin et al. (1996) for the high density limit of reaction 6 and adopt a value 8 times smaller than this for reaction 7, following Jacobs et al. (1967). At densities below the H_2 critical density ($n \sim 10^4\,\mathrm{cm}^{-3}$), we therefore recover the same behaviour as in G17, and we also find good agreement between the different treatments in hot ($T > 6000$ K), high density gas. The only significant difference comes in cool dense gas, where the Lepp & Shull (1983) expression over-estimates the H_2 collisional dissociation rate. However, given the small size of this rate at these temperatures, this difference is likely only of minor importance.

Reaction 8

We adopt the rate coefficient for this reaction given in Stancil et al. (1998), which is their fit to cross-section data from Linder et al. (1995). G17 also cite Linder et al. (1995) as the source of their rate coefficient, but their expression is ∼27% larger than the one given in Stancil et al. (1998). The source of this discrepancy is unclear. However, in practice it is unlikely to be important as this reaction is never the rate-limiting step for the formation of H_3^+.

Reaction 13

G17 assume case B for the radiative recombination of He^+ and use a reaction rate coefficient from Glover et al. (2010b) that is a fit to the values tabulated by Hummer & Storey (1998). Our treatment differs from this in two respects. First, in addition to radiative recombination, we also account for dielectronic recombination of He^+, using a rate coefficient from Badnell (2006). Second, although we assume the on-the-spot approximation applies, we do not assume pure case B recombination for He^+, which would be valid only in a gas consisting of pure helium. Instead, we follow Osterbrock (1989) and account for the fact that some of the photons produced during the recombination of He^+ are absorbed by atomic hydrogen rather than He. (A more detailed discussion of how this is done can be found in Glover & Jappsen 2007).

Reaction 18

As in G17, we adopt a rate coefficient for C^+ recombination that is the sum of two contributions: one corresponding to radiative recombination, taken from Badnell (2006), and one corresponding to dielectronic recombination, taken from Badnell et al. (2003). In the expression that they use for the dielectronic recombination rate, G17 retain only the first three terms, which is sufficient at low temperatures but which leads to inaccuracies at high temperatures ($T \gg 10^4$ K). In our implementation of this rate, we instead retain all of the terms from the expression given by Badnell et al. (2003).

Reaction 35

G17 adopt a temperature-independent rate for this reaction from Anicich & Huntress (1986), whereas we adopt the temperature-dependent value proposed by Petuchowski et al. (1989). In practice, there is very little difference between these two values at typical PDR temperatures.

Reaction 39

G17 adopt a rate coefficient for this reaction that they credit to McElroy et al. (2013) but that derives originally from Pequignot & Aldrovandi (1986). However, this fit is formally valid only in the temperature range $10 < T < 1000$ K. Moreover, it only accounts for the contribution from radiative recombination, and not the dielectronic recombination term that dominates at high temperatures. We adopt instead a rate from Nahar (2000) that accounts for both processes.

Reaction 41

G17 adopt a constant value of $3 \times 10^{-17}\,\mathrm{cm^3\,s^{-1}}$ for the rate coefficient for this reaction. We instead adopt the rate coefficient given in Hollenbach & McKee (1979), which depends on the temperatures of both the gas and the dust grains.

Reaction 42--45

We follow G17 in that we use the reaction rate coefficients given in Weingartner & Draine (2001) for the recombination of H^+, C^+, He^+ and Si^+ ions on grain surfaces (reactions 42–45), multiplied by a factor of 0.6 to better match the results of Wolfire et al. (2008). These rate coefficients depend primarily on the parameter

$$\psi = \frac{G\sqrt{T}}{n_\mathrm{e}}, \tag{A.1}$$

where G is the local value of the interstellar radiation field in Habing (1968) units and n_e is the electron number density. One important way in which our treatment differs from G17 is in our treatment of these rate coefficients for low values of ψ. The expressions given in Weingartner & Draine (2001) are stated to be valid only for $\psi > 100\ \mathrm{K}^{1/2}\ \mathrm{cm}^3$ and applying them unaltered when the value of ψ is smaller than this yields recombination rates that are significant over-estimates of the true values. To avoid this, we simply assume that the rates in gas with $\psi < 100\ \mathrm{K}^{1/2}\ \mathrm{cm}^3$ are the same as those in gas with $\psi = 100\ \mathrm{K}^{1/2}\ \mathrm{cm}^3$ (c.f. figure 3 in Weingartner & Draine 2001).

The other main difference between our treatment and that in G17 is that we multiply the grain surface recombination rates by an additional factor of $\exp(-T/34000)$. This is to ensure that the recombination rates fall rapidly to zero in very hot gas, in conditions where we expect that in reality the dust would be quickly destroyed by sputtering. This modification would not be necessary if we were using a more sophisticated treatment of dust evolution that accounted for this effect (see e.g. McKinnon et al., 2017), but this is a topic for future work.

A.2 Post-collision magnetic field

Here we illustrate how the magnetic field is warped in the process of the collision of the clouds. Figures A.1 & A.2 show images of the magnitude and z-component of the magnetic field, respectively, which have been convolved with the x-y components of magnetic field via line integral convolution (LIC) (Cabral & Leedom, 1993). This is done to give indication of the direction of the magnetic field in the x-y plane.

We noted in Section 3.3.1 that an early onset of star formation is observed for a magnetic field inclination of $\theta = 0$, i.e. a field that is initially parallel to the collision axis. In this case, the magnetic field is not compressed during the collision and hence does not hinder the collision process. This can be seen clearly in the central panels of Figures A.1 & A.2, where the pattern of the map generated by the LIC lies predominantly parallel to the x-axis. Only at the site of the collision is the magnetic field distorted, owing to the local collapse of the gas.

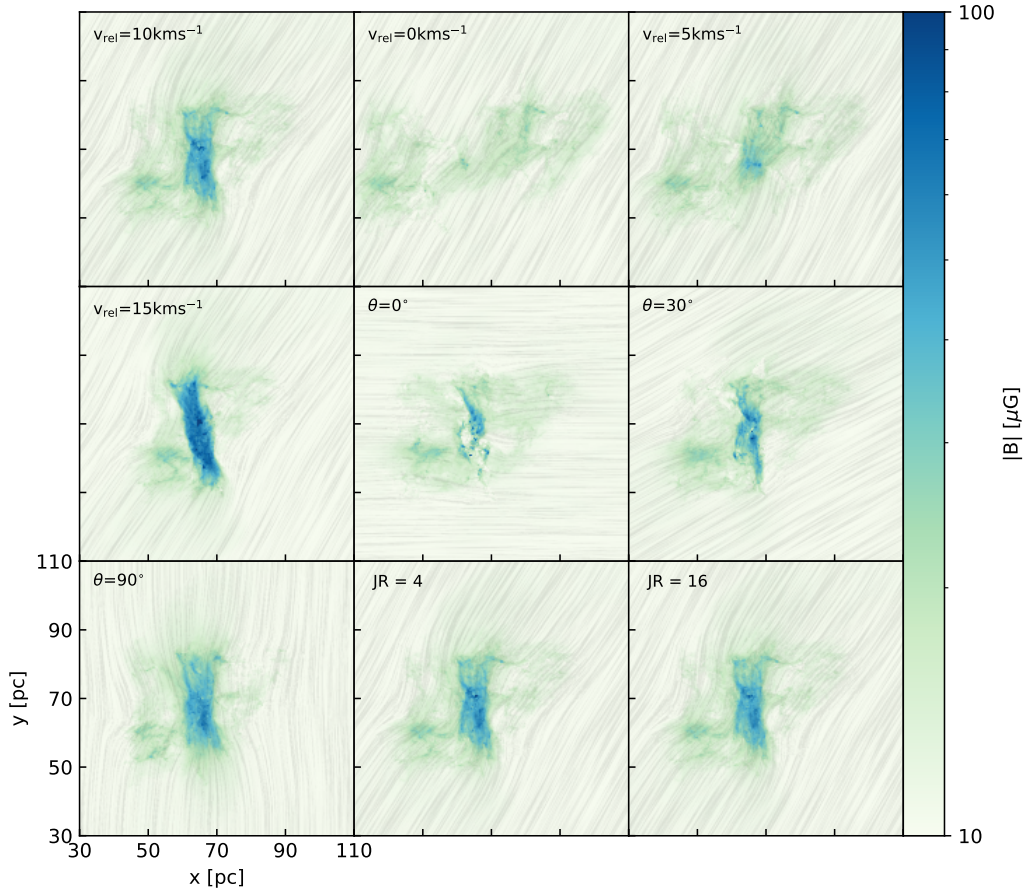

Figure A.1. Maps of the magnetic field strength of the simulations carried out at $t = 2.40$ Myr. Line integral convolution (LIC) is used on the map to indicate the direction of the magnetic field in the x-y plane.

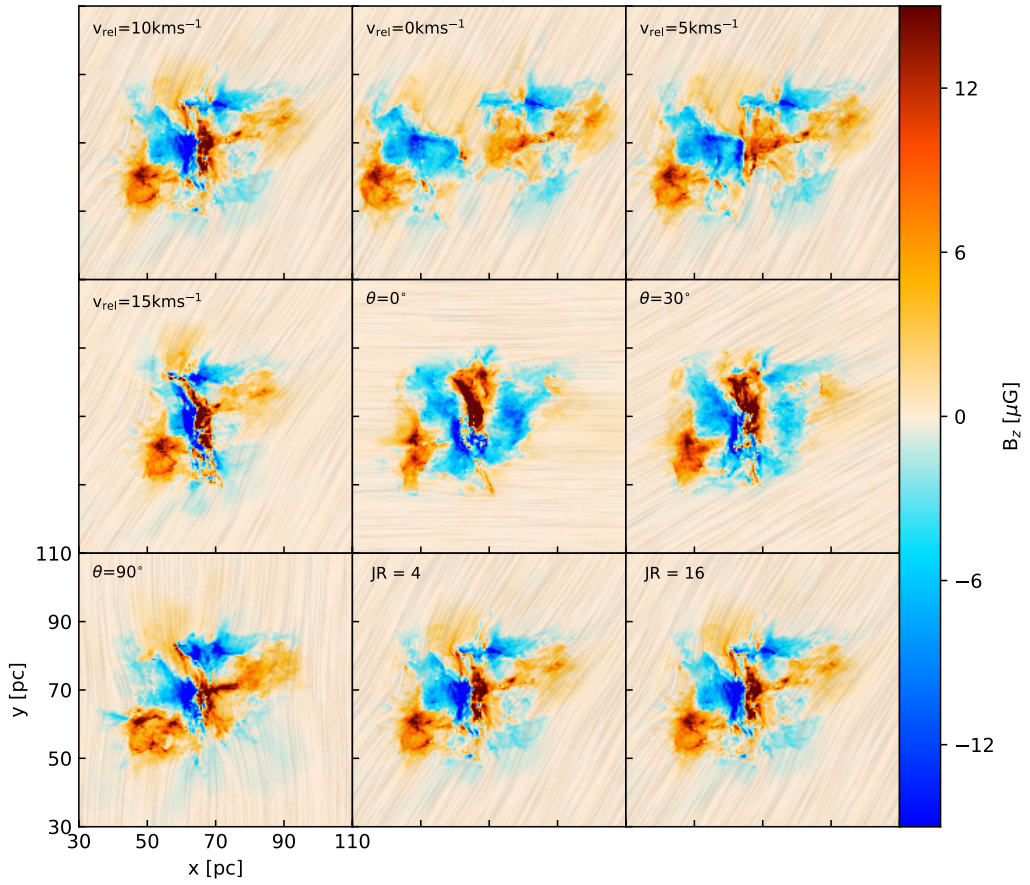

Figure A.2. Same as figure A.1 but for the z component of the magnetic field

Appendix B

Additional information for Chapter 4

B.1 Spiral arm strength

We perform some additional simulations to determine the ideal our spiral arm strength factor α in Equation 4.15. We test three different strengths for our spiral arm tests, $\alpha = 0.204, 0.408, 0.612$ which correspond to a peak density contrast of 10%, 20% and 30% respectively. We present the resulting simulations in Figure B.1.

The 10% density contrast, consistent with Eilers et al. (2020), gives arise to fainter spiral arms with the spiral arms generated by the rotation of the spiral arm dominating much of the structure outside of the bar. With increasing spiral arm strength, the spiral arms in the simulation become stronger but also narrower due to the shape of the underlying spiral arm potential.

In order to avoid the spiral arms becoming too narrow we opt to use a value of $\alpha = 0.36$ which gives a spiral arm strength of $\sim 17\%$ of the stellar disk density at solar circle $R = 8.179$ kpc.

B.2 Parameter study

We perform a simple parameter study with the potential to understand how varying certain parameters impacts the lv diagram. This involves multiple simulations with the changed parameters. The parameters we consider are number of spiral arms (n), pitch angle of the spiral arms (i), spiral arm pattern speed ($\Omega_{\rm spiral}$) and bar pattern speed ($\Omega_{\rm bar}$). The values considered are indicated in Table B.1. We consider two sets of parameter studies, one for each spiral arm number, in which we vary one of the other parameters and keep all other fixed to the fiducial values. Our fiducial parameters are based on the same parameters in Li et al. (2022). This allows us to investigate how each

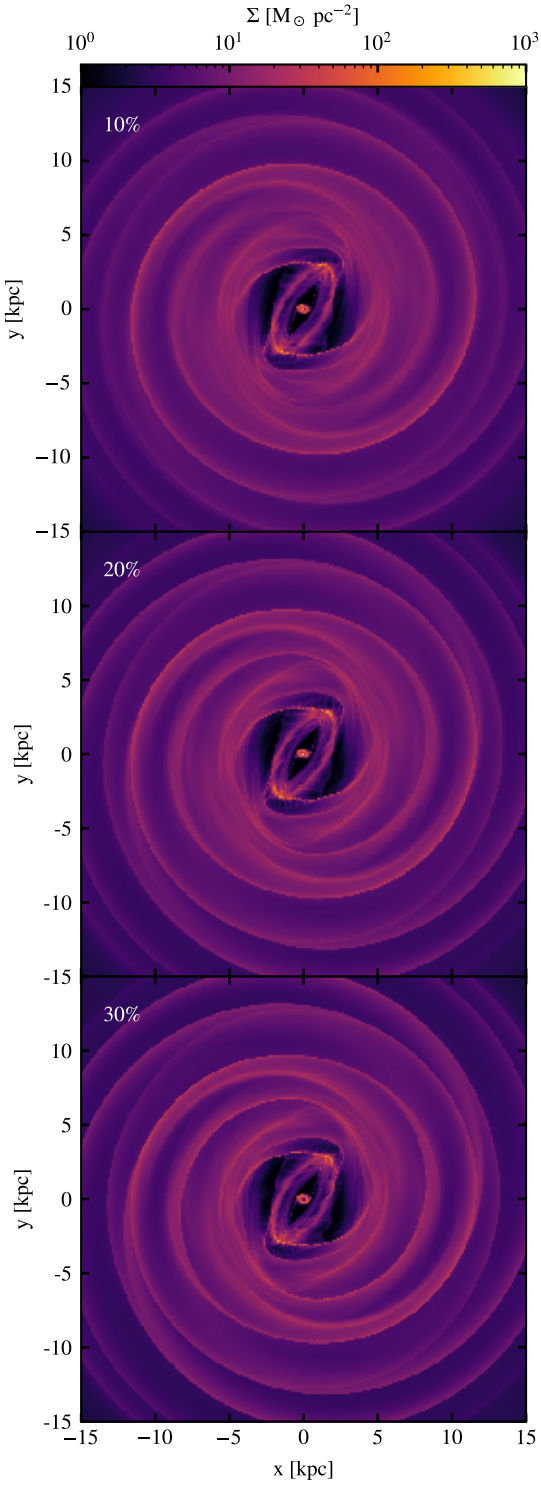

Figure B.1. The density maps of simulations of differing spiral arm strength at $t = 441$ Myr. The strength of the spiral arm pertibation increase from 10% to 30% stellar disk density at $R = 8.179$ kpc from top to bottom.

individual parameter alters the lv diagram and later to vary the parameters to obtain an appropriate approximate match between the observed spiral arms and those in our simulations in lv space.

We present the lv diagrams of our parameter study in Figures B.2 & B.3. The first thing that stands out between the figures is the number of filamentary structures in the lv diagram away from the centre of the galaxy, most notably the feature that goes between two spiral arms in the region of $\sim -50°$ to $\sim -130°$ that is present in the $n = 4$ set but not in the $n = 2$ set. At positive galactic longitudes, we find the expected additional spiral arms with the $n = 4$ set. We find that two of the arms in this region of the lv diagram lie very close to each other for the $n = 4$, appearing to have split from a spiral arm in the same region in lv space in the $n = 2$ set.

From the first column of both figures we see that pitch angle has little impact on the shape of the spiral arms in lv space outside the central region. However, within the central 60°, differences can be seen between lv diagrams. Here some features move towards the Galactic centre in lv space with increasing pitch angle though not all features, with those associated with the bar's rotation remaining fixed in position.

The spiral arm pattern speed has a larger impact as the corresponding resonances for the spiral arms end up changing with pattern speed. This in turn causes the spiral arms to become more apparent with increasing pattern speed beyond the central region of the lv diagram. Additionally, the features associated with the spiral arms tend towards 0 km s^{-1} in lv space. Within the inner most 60° of the Galaxy, the structure here also moves similarly to how it does with pitch angle, moving towards the galactic with increasing pattern speed, however the features here that move are different to those with increasing pitch angle suggesting these are resonance features from the spiral arms.

Similar to the spiral arm pattern speed, changes to bar pattern speed gives arise to different positions for the resonances of the bar, with them moving inward towards $R = 0$ kpc with increasing pattern speed (see Fig. 4.6). In the lv diagram we see an effect similar to that of the spiral arm pattern speed. Here we see the spiral arms generated by the bar moving towards 0 km s^{-1} in lv space, however the broadening of the features does not happen in this case.

It should be noted for all lv diagrams presented in this section have been selected to have approximately the same phase angle between the bar and spiral arms. This means that whilst each snapshot will has similar phase angle between bar and spiral arms, they will be at different stages in evolution. We select snapshots as close as possible in time late into the systems' evolution ($t > 381$ Myr), however there is a range of 147 Myr within the snapshots selected.

In all cases, the resulting lv diagrams are similar enough that altering one parameter

Table B.1. Parameter values considered

Parameter	Values	Unit
n	2, 4	
i	10, 12.5*, 15, 17.5	[°]
Ω_{spiral}	-17.5, -20, -22.5*, -25	[km s^{-1} kpc^{-1}]
Ω_{bar}	-36.25, -37.5*, -38.75, -40	[km s^{-1} kpc^{-1}]

* Fiducial values.

within the constraints of our parameter range does not induce large deviations. However, an exact match to the spiral arm models of McClure-Griffiths et al. (2004), Reid et al. (2014) and Reid et al. (2019) requires more sophisticated modeling that is beyond the scope of this paper.

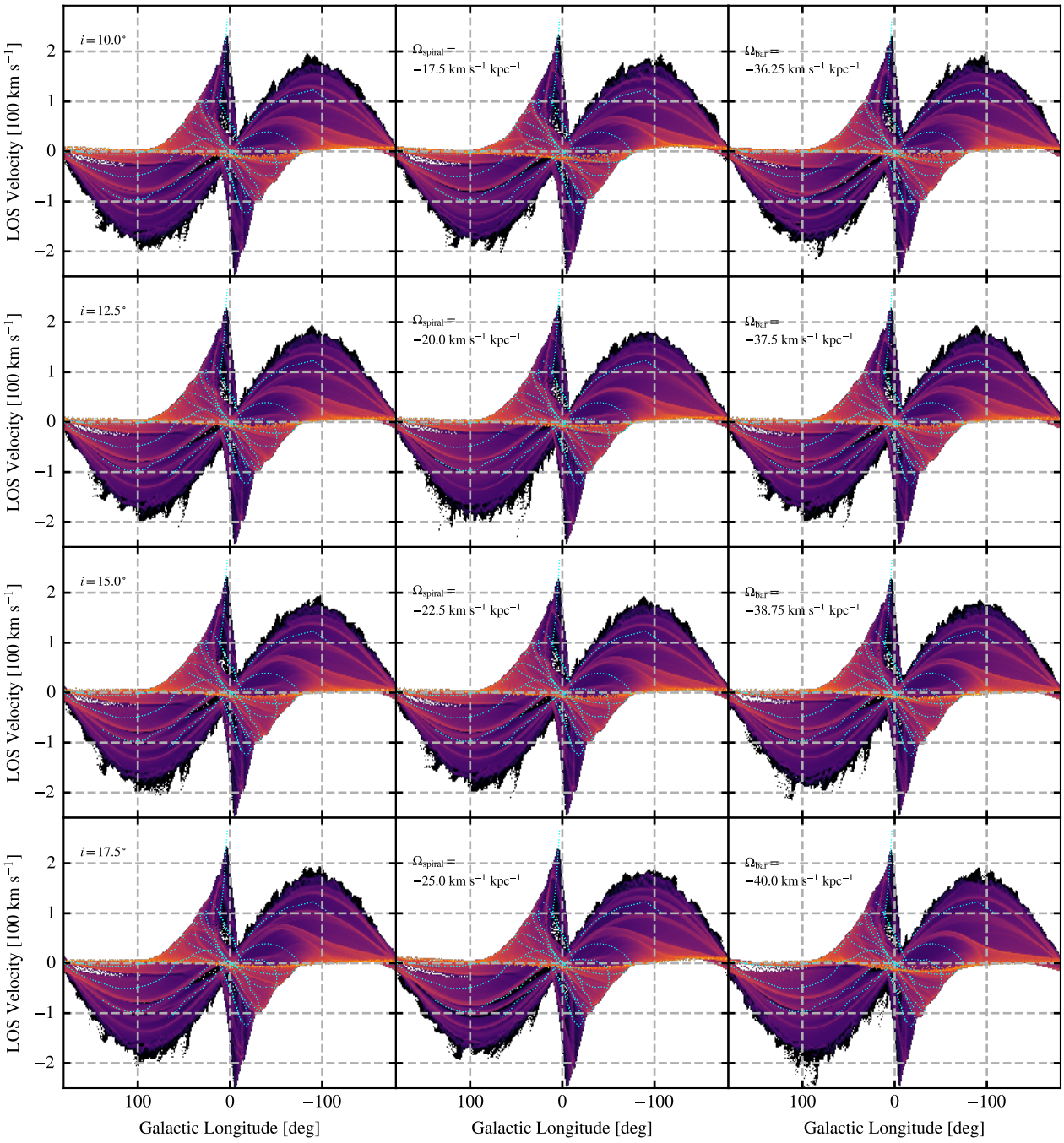

Figure B.2. Longitude velocity diagrams of our parameter study with $n = 2$ spiral arms with similar phase angle between the spiral arm potential and the bar. Left column is where we vary the pitch angle. The middle and right columns are the variation in spiral arm pattern speed and bar pattern speed respectively.

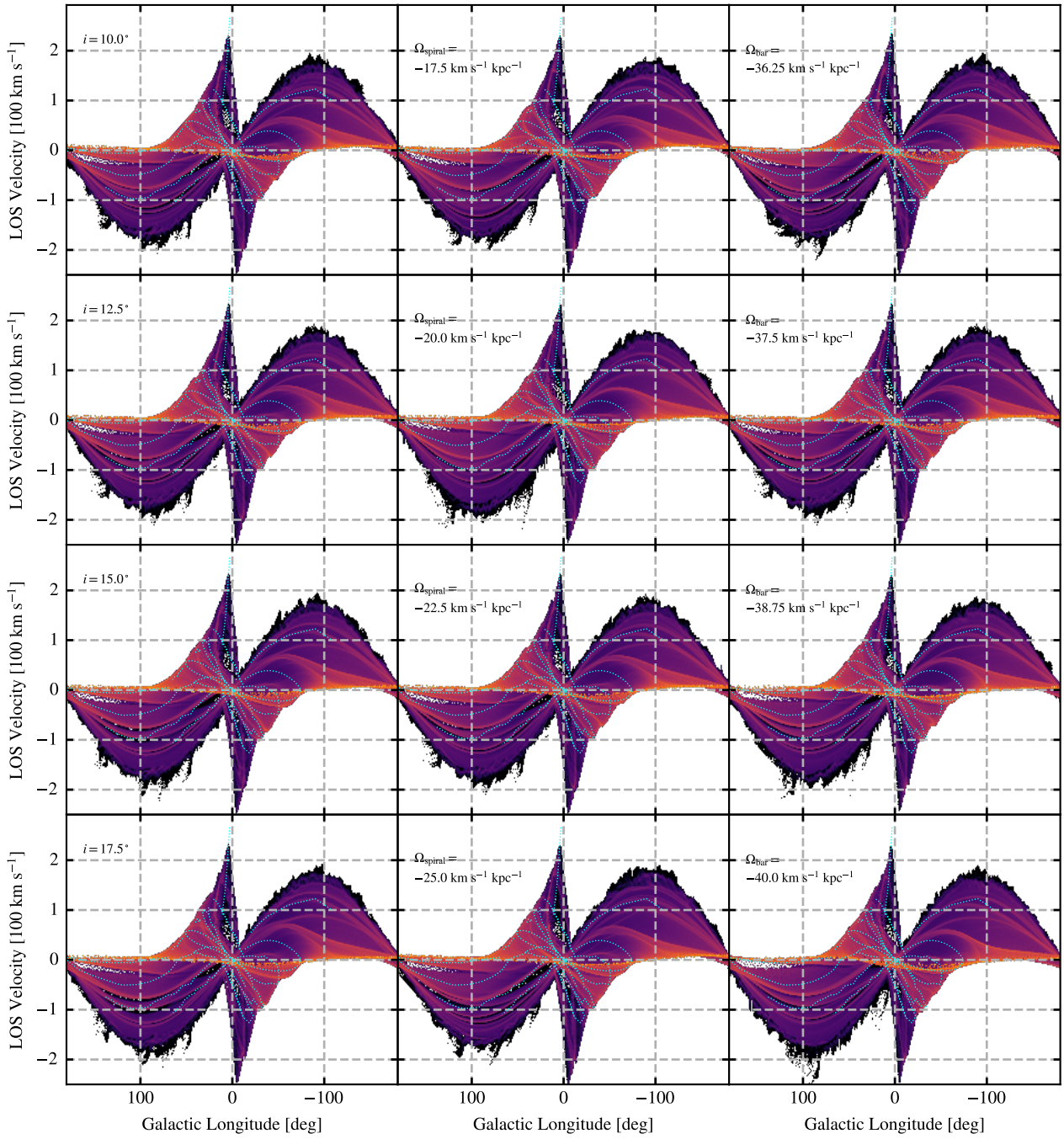

Figure B.3. Same as Figure B.2 but with the $n = 4$ spiral arms subset.

Bibliography

Aguerri J. A. L., Méndez-Abreu J., Corsini E. M., 2009, A&A, 495, 491

Ahumada R., et al., 2020, ApJS, 249, 3

Anderson L. D., Bania T. M., Balser D. S., Rood R. T., 2012, ApJ, 754, 62

André P., et al., 2010, A&A, 518, L102

Anicich V. G., Huntress W. T. J., 1986, ApJS, 62, 553

Astropy Collaboration et al., 2013, A&A, 558, A33

Astropy Collaboration et al., 2018, AJ, 156, 123

Athanassoula E., 2005, MNRAS, 358, 1477

Athanassoula E., Morin S., Wozniak H., Puy D., Pierce M. J., Lombard J., Bosma A., 1990, MNRAS, 245, 130

Baba J., Asaki Y., Makino J., Miyoshi M., Saitoh T. R., Wada K., 2009, ApJ, 706, 471

Badnell N. R., 2006, ApJS, 167, 334

Badnell N. R., et al., 2003, A&A, 406, 1151

Balfour S. K., Whitworth A. P., Hubber D. A., Jaffa S. E., 2015, MNRAS, 453, 2471

Balser D. S., Wenger T. V., Anderson L. D., Bania T. M., 2015, ApJ, 806, 199

Barlow S. E., 1984, PhD thesis, UNIVERSITY OF COLORADO AT BOULDER.

Barnes J., Hut P., 1986, Nature, 324, 446

Bate M. R., Bonnell I. A., Price N. M., 1995, MNRAS, 277, 362

Begeman K. G., Broeils A. H., Sanders R. H., 1991, MNRAS, 249, 523

Bertelli Motta C., Clark P. C., Glover S. C. O., Klessen R. S., Pasquali A., 2016, MNRAS, 462, 4171

Bertoldi F., McKee C. F., 1992, ApJ, 395, 140

Bhattacharjee P., Chaudhury S., Kundu S., 2014, ApJ, 785, 63

Bigiel F., Leroy A., Walter F., Brinks E., de Blok W. J. G., Madore B., Thornley M. D., 2008, AJ, 136, 2846

Binney J., Tremaine S., 2008, Galactic Dynamics: Second Edition

Binney J., Gerhard O. E., Stark A. A., Bally J., Uchida K. I., 1991, MNRAS, 252, 210

Bland-Hawthorn J., Gerhard O., 2016, ARA&A, 54, 529

Blitz L., 1993, in Levy E. H., Lunine J. I., eds, Protostars and Planets III. p. 125

Blitz L., Fich M., Stark A. A., 1982, ApJS, 49, 183

Bodenheimer P. H., 2011, Principles of Star Formation, doi:10.1007/978-3-642-15063-0.

Bolatto A. D., Wolfire M., Leroy A. K., 2013, ARA&A, 51, 207

Boldyrev S., 2006, Phys. Rev. Lett., 96, 115002

Bosma A., 1978, PhD thesis, University of Groningen, Netherlands

Bovy J., 2015, ApJS, 216, 29

Bovy J., Rix H.-W., 2013, ApJ, 779, 115

Brand J., Blitz L., 1993, A&A, 275, 67

Bruderer S., 2019, PyPDR: Python Photo Dissociation Regions (ascl:1905.027)

Burton W. B., Gordon M. A., 1978, A&A, 63, 7

Burton W. B., Liszt H. S., 1993, A&A, 274, 765

Buta R. J., Knapen J. H., Elmegreen B. G., Salo H., Laurikainen E., Elmegreen D. M., Puerari I., Block D. L., 2009, AJ, 137, 4487

Cabral B., Leedom L. C., 1993, in Proceedings of the 20th Annual Conference on Computer Graphics and Interactive Techniques. SIGGRAPH '93. Association for Computing Machinery, New York, NY, USA, pp 263–270, doi:10.1145/166117.166151, https://doi.org/10.1145/166117.166151

Carroll B. W., Ostlie D. A., 2017, An introduction to modern astrophysics, Second Edition. Cambridge University Press

Carty D., Goddard A., Köhler S. P. K., Sims I. R., Smith I. W. M., 2006, Journal of Physical Chemistry A, 110, 3101

Cautun M., et al., 2020, MNRAS, 494, 4291

Chatzopoulos S., Fritz T. K., Gerhard O., Gillessen S., Wegg C., Genzel R., Pfuhl O., 2015, MNRAS, 447, 948

Chemin L., de Blok W. J. G., Mamon G. A., 2011, AJ, 142, 109

Chemin L., Renaud F., Soubiran C., 2015, A&A, 578, A14

Chevance M., et al., 2020, MNRAS, 493, 2872

Chevance M., et al., 2022, MNRAS, 509, 272

Chira R. A., Beuther H., Linz H., Schuller F., Walmsley C. M., Menten K. M., Bronfman L., 2013, A&A, 552, A40

Choi Y. K., Hachisuka K., Reid M. J., Xu Y., Brunthaler A., Menten K. M., Dame T. M., 2014, ApJ, 790, 99

Chomiuk L., Povich M. S., 2011, AJ, 142, 197

Chung A., Bureau M., 2004, AJ, 127, 3192

Clark P. C., Glover S. C. O., Klessen R. S., 2012, MNRAS, 420, 745

Clark P. C., Glover S. C. O., Ragan S. E., Duarte-Cabral A., 2019, MNRAS, 486, 4622

Clarke J. P., Gerhard O., 2022, MNRAS, 512, 2171

Clemens D. P., 1985, ApJ, 295, 422

Coleman B., Paterson D., Gordon C., Macias O., Ploeg H., 2020, MNRAS, 495, 3350

Combes F., Sanders R. H., 1981, A&A, 96, 164

Contopoulos G., Grosbol P., 1989, A&ARv, 1, 261

Correa Magnus L., Vasiliev E., 2022, MNRAS, 511, 2610

Cox D. P., Gómez G. C., 2002, ApJS, 142, 261

Crutcher R. M., Wandelt B., Heiles C., Falgarone E., Troland T. H., 2010, ApJ, 725, 466

Dame T. M., et al., 1987, ApJ, 322, 706

Dame T. M., Hartmann D., Thaddeus P., 2001, ApJ, 547, 792

De Rijcke S., Voulis I., 2016, MNRAS, 456, 2024

Dedner A., Kemm F., Kröner D., Munz C.-D., Schnitzer T., Wesenberg M., 2002, Journal of Computational Physics, 175, 645

Dehnen W., 1993, MNRAS, 265, 250

Dehnen W., Binney J., 1998, MNRAS, 294, 429

Demers S., Battinelli P., 2007, A&A, 473, 143

Dobbs C. L., Wurster J., 2021, MNRAS, 502, 2285

Dobbs C. L., Theis C., Pringle J. E., Bate M. R., 2010, MNRAS, 403, 625

Dobbs C. L., Burkert A., Pringle J. E., 2011, MNRAS, 413, 2935

Dobbs C. L., et al., 2014, in Beuther H., Klessen R. S., Dullemond C. P., Henning T., eds, Protostars and Planets VI. pp 3–26 (arXiv:1312.3223), doi:10.2458/azu_uapress_9780816531240-ch001

Dobbs C. L., Pringle J. E., Duarte-Cabral A., 2015, MNRAS, 446, 3608

Dobbs C. L., Liow K. Y., Rieder S., 2020, MNRAS, 496, L1

Draine B. T., 1978, ApJS, 36, 595

Draine B. T., 2011, Physics of the Interstellar and Intergalactic Medium. Princeton University Press

Draine B. T., Bertoldi F., 1996, ApJ, 468, 269

Eilers A.-C., Hogg D. W., Rix H.-W., Ness M. K., 2019, ApJ, 871, 120

Eilers A.-C., Hogg D. W., Rix H.-W., Frankel N., Hunt J. A. S., Fouvry J.-B., Buck T., 2020, ApJ, 900, 186

Einasto J., 1969, Astronomische Nachrichten, 291, 97

Elia D., et al., 2022, ApJ, 941, 162

Elmegreen B. G., 2007, ApJ, 668, 1064

Emsellem E., et al., 2022, A&A, 659, A191

Federrath C., 2015, MNRAS, 450, 4035

Federrath C., Banerjee R., Clark P. C., Klessen R. S., 2010, ApJ, 713, 269

Ferland G. J., Peterson B. M., Horne K., Welsh W. F., Nahar S. N., 1992, ApJ, 387, 95

Ferland G. J., Korista K. T., Verner D. A., Ferguson J. W., Kingdon J. B., Verner E. M., 1998, PASP, 110, 761

Fich M., Blitz L., Stark A. A., 1989, ApJ, 342, 272

Field G. B., 1965, ApJ, 142, 531

Flower D. R., Le Bourlot J., Pineau des Forêts G., Cabrit S., 2003, MNRAS, 341, 70

Foster T., MacWilliams J., 2006, ApJ, 644, 214

Freeman K. C., 1970, ApJ, 160, 811

Freudenreich H. T., 1998, ApJ, 492, 495

Fujita S., et al., 2021, PASJ, 73, S201

Fukui Y., et al., 1999, PASJ, 51, 745

Fukui Y., Tsuge K., Sano H., Bekki K., Yozin C., Tachihara K., Inoue T., 2017, PASJ, 69, L5

Fukui Y., et al., 2019, ApJ, 886, 14

Fukui Y., Habe A., Inoue T., Enokiya R., Tachihara K., 2021, PASJ, 73, S1

GRAVITY Collaboration et al., 2019, A&A, 625, L10

Gaia Collaboration et al., 2023, A&A, 674, A1

Gao L., Navarro J. F., Cole S., Frenk C. S., White S. D. M., Springel V., Jenkins A., Neto A. F., 2008, MNRAS, 387, 536

Geppert W. D., et al., 2005, in Journal of Physics Conference Series. pp 26–31, doi:10.1088/1742-6596/4/1/004

Gilmore G., Reid N., 1983, MNRAS, 202, 1025

Gingold R. A., Monaghan J. J., 1977, MNRAS, 181, 375

Girichidis P., et al., 2020, Space Sci. Rev., 216, 68

Glassgold A. E., Langer W. D., 1974, ApJ, 193, 73

Glover S. C. O., 2003, ApJ, 584, 331

Glover S. C. O., Clark P. C., 2012, MNRAS, 421, 116

Glover S. C. O., Jappsen A. K., 2007, ApJ, 666, 1

Glover S. C. O., Mac Low M.-M., 2007a, ApJS, 169, 239

Glover S. C. O., Mac Low M.-M., 2007b, ApJ, 659, 1317

Glover S. C. O., Smith R. J., 2016, MNRAS, 462, 3011

Glover S. C. O., Federrath C., Mac Low M. M., Klessen R. S., 2010a, MNRAS, 404, 2

Glover S. C. O., Federrath C., Mac Low M. M., Klessen R. S., 2010b, MNRAS, 404, 2

Goldreich P., Lynden-Bell D., 1965, MNRAS, 130, 125

Gómez G. C., 2006, AJ, 132, 2376

Gong M., Ostriker E. C., Wolfire M. G., 2017, ApJ, 843, 38

Gould R. J., Salpeter E. E., 1963, ApJ, 138, 393

Green G. M., Schlafly E., Zucker C., Speagle J. S., Finkbeiner D., 2019, ApJ, 887, 93

Grisdale K., Agertz O., Romeo A. B., Renaud F., Read J. I., 2017, MNRAS, 466, 1093

Habe A., Ohta K., 1992, PASJ, 44, 203

Habing H. J., 1968, Bull. Astron. Inst. Netherlands, 19, 421

Haid S., Walch S., Seifried D., Wünsch R., Dinnbier F., Naab T., 2018, MNRAS, 478, 4799

Hanawa T., et al., 1993, ApJ, 404, L83

Harris C. R., et al., 2020, Nature, 585, 357

Hartmann L., Ballesteros-Paredes J., Heitsch F., 2012, MNRAS, 420, 1457

Haworth T. J., Shima K., Tasker E. J., Fukui Y., Torii K., Dale J. E., Takahira K., Habe A., 2015, MNRAS, 454, 1634

Heays A. N., Bosman A. D., van Dishoeck E. F., 2017, A&A, 602, A105

Heitsch F., Slyz A. D., Devriendt J. E. G., Hartmann L. W., Burkert A., 2006, ApJ, 648, 1052

Henon M., 1997, Generating Families in the Restricted Three-Body Problem

Henshaw J. D., Barnes A. T., Battersby C., Ginsburg A., Sormani M. C., Walker D. L., 2023, in Inutsuka S., Aikawa Y., Muto T., Tomida K., Tamura M., eds, Astronomical Society of the Pacific Conference Series Vol. 534, Protostars and Planets VII. p. 83 (arXiv:2203.11223), doi:10.48550/arXiv.2203.11223

Hernquist L., 1990, ApJ, 356, 359

Heyer M. H., Brunt C. M., 2004, ApJ, 615, L45

Heyer M., Dame T. M., 2015, ARA&A, 53, 583

Hillenbrand L. A., Hartmann L. W., 1998, ApJ, 492, 540

Hollenbach D., McKee C. F., 1979, ApJS, 41, 555

Hollenbach D., Salpeter E. E., 1971, ApJ, 163, 155

Holley-Bockelmann K., Weinberg M., Katz N., 2005, MNRAS, 363, 991

Hopkins P. F., 2015, MNRAS, 450, 53

Hoyle F., 1953, ApJ, 118, 513

Hu C.-Y., Sternberg A., van Dishoeck E. F., 2021, ApJ, 920, 44

Hu Y., Federrath C., Xu S., Mathew S. S., 2022, arXiv e-prints, p. arXiv:2203.01508

Hummer D. G., Storey P. J., 1998, MNRAS, 297, 1073

Hunter J. D., 2007, Computing in Science & Engineering, 9, 90

Hunter G. H., Clark P. C., Glover S. C. O., Klessen R. S., 2023, MNRAS, 519, 4152

Hunter G. H., et al., 2024, arXiv e-prints, p. arXiv:2403.18000

Inoue T., Inutsuka S.-i., 2012, ApJ, 759, 35

Jacobs T. A., Giedt R. R., Cohen N., 1967, J. Chem. Phys., 47, 54

Jaffe W., 1983, MNRAS, 202, 995

Janev R. K., Langer W. D., Evans K., 1987, Elementary processes in Hydrogen-Helium plasmas - Cross sections and reaction rate coefficients. Springer

Jeans J. H., 1902, Philosophical Transactions of the Royal Society of London Series A, 199, 1

Jeffreson S. M. R., Kruijssen J. M. D., 2018, MNRAS, 476, 3688

Jones G. H., Clark P. C., Glover S. C. O., Hacar A., 2023, MNRAS, 520, 1005

Junqueira T. C., Lépine J. R. D., Braga C. A. S., Barros D. A., 2013, A&A, 550, A91

Jurić M., et al., 2008, ApJ, 673, 864

Kainulainen J., Stutz A. M., Stanke T., Abreu-Vicente J., Beuther H., Henning T., Johnston K. G., Megeath S. T., 2017, A&A, 600, A141

Kalberla P. M. W., Dedes L., 2008, A&A, 487, 951

Karpas Z., Anicich V., Huntress W. T., 1979, J. Chem. Phys., 70, 2877

Kauffmann J., Pillai T., Goldsmith P. F., 2013, ApJ, 779, 185

Khanna S., et al., 2019, MNRAS, 489, 4962

Kim J. K., Theard L. P., Huntress W. T. J., 1975, Chemical Physics Letters, 32, 610

Kippenhahn R., Weigert A., Weiss A., 2012, Stellar Structure and Evolution, doi:10.1007/978-3-642-30304-3.

Klessen R. S., 2000, ApJ, 535, 869

Klessen R. S., Glover S. C. O., 2016, in Revaz Y., Jablonka P., Teyssier R., Mayer L., eds, Saas-Fee Advanced Course Vol. 43, Saas-Fee Advanced Course. p. 85 (arXiv:1412.5182), doi:10.1007/978-3-662-47890-5_2

Koch E. W., Rosolowsky E. W., 2015, MNRAS, 452, 3435

Kohno M., Sofue Y., 2024, MNRAS, 527, 9290

Kolmogorov A., 1941, Akademiia Nauk SSSR Doklady, 30, 301

Koposov S. E., et al., 2023, MNRAS, 521, 4936

Krause M. G. H., et al., 2020, Space Sci. Rev., 216, 64

Kruijssen J. M. D., et al., 2019, Nature, 569, 519

Krumholz M. R., McKee C. F., 2005a, ApJ, 630, 250

Krumholz M. R., McKee C. F., 2005b, ApJ, 630, 250

Krumholz M. R., Tan J. C., 2007, ApJ, 654, 304

Krumholz M. R., McKee C. F., Bland-Hawthorn J., 2019, ARA&A, 57, 227

Kuijken K., Dubinski J., 1995, MNRAS, 277, 1341

Lada C. J., Lombardi M., Alves J. F., 2010, ApJ, 724, 687

Lallement R., Babusiaux C., Vergely J. L., Katz D., Arenou F., Valette B., Hottier C., Capitanio L., 2019, A&A, 625, A135

Lang P., et al., 2020, ApJ, 897, 122

Larson R. B., 1979, MNRAS, 186, 479

Larson R. B., 1981, MNRAS, 194, 809

Latter W. B., Black J. H., 1991, ApJ, 372, 161

Leike R. H., Glatzle M., Enßlin T. A., 2020, A&A, 639, A138

Lepp S., Shull J. M., 1983, ApJ, 270, 578

Leroy A. K., Walter F., Brinks E., Bigiel F., de Blok W. J. G., Madore B., Thornley M. D., 2008, AJ, 136, 2782

Leroy A. K., et al., 2012, AJ, 144, 3

Leroy A. K., et al., 2017, ApJ, 846, 71

Leroy A. K., et al., 2021, arXiv e-prints, p. arXiv:2104.07739

Levine E. S., Blitz L., Heiles C., 2006, Science, 312, 1773

Li Z., Shen J., Gerhard O., Clarke J. P., 2022, ApJ, 925, 71

Liang H., Luo N., Shen T., Sun X., Fan X., Cao Y., 2019, Journal of Materials Research and Technology, 9

Lin C. C., Shu F. H., 1964, ApJ, 140, 646

Linder F., Janev R. K., Botero J., 1995, in Janev R. K., ed., Atomic and Molecular Processes in Fusion Edge Plasmas. p. 397

Liow K. Y., Dobbs C. L., 2020, MNRAS, 499, 1099

Lombardi M., Bouy H., Alves J., Lada C. J., 2014, A&A, 566, A45

López P. D., Scannapieco C., Cora S. A., Gargiulo I. D., 2024, MNRAS, 529, 979

Loveday J., 1996, MNRAS, 278, 1025

Lu Z.-J., Pelkonen V.-M., Padoan P., Pan L., Haugbølle T., Nordlund Å., 2020, ApJ, 904, 58

Lucy L. B., 1977, AJ, 82, 1013

Lynden-Bell D., 1979, MNRAS, 187, 101

Mac Low M.-M., Klessen R. S., 2004, Reviews of Modern Physics, 76, 125

Mac Low M. M., Shull J. M., 1986, ApJ, 302, 585

Majewski S. R., et al., 2017, AJ, 154, 94

Martin P. G., Schwarz D. H., Mandy M. E., 1996, ApJ, 461, 265

Martin P. G., Keogh W. J., Mandy M. E., 1998, ApJ, 499, 793

Matthaeus W. H., Pouquet A., Mininni P. D., Dmitruk P., Breech B., 2008, Phys. Rev. Lett., 100, 085003

McCall B. J., et al., 2004, Phys. Rev. A, 70, 052716

McClure-Griffiths N. M., Dickey J. M., 2007, ApJ, 671, 427

McClure-Griffiths N. M., Dickey J. M., Gaensler B. M., Green A. J., 2004, ApJ, 607, L127

McElroy D., Walsh C., Markwick A. J., Cordiner M. A., Smith K., Millar T. J., 2013, A&A, 550, A36

McKee C. F., Ostriker J. P., 1977, ApJ, 218, 148

McKee C. F., Ostriker E. C., 2007, ARA&A, 45, 565

McKee C. F., Williams J. P., 1997, ApJ, 476, 144

McKinnon R., Torrey P., Vogelsberger M., Hayward C. C., Marinacci F., 2017, MNRAS, 468, 1505

McMillan P. J., 2017, MNRAS, 465, 76

Menon T. K., 1958, ApJ, 127, 28

Merrifield M. R., Kuijken K., 1999, A&A, 345, L47

Messineo M., Habing H. J., Sjouwerman L. O., Omont A., Menten K. M., 2002, A&A, 393, 115

Messineo M., Habing H. J., Menten K. M., Omont A., Sjouwerman L. O., 2004, A&A, 418, 103

Messineo M., Habing H. J., Menten K. M., Omont A., Sjouwerman L. O., Bertoldi F., 2005, A&A, 435, 575

Micic M., Glover S. C. O., Federrath C., Klessen R. S., 2012, MNRAS, 421, 2531

Mitchell G. F., 1984, ApJS, 54, 81

Molinari S., et al., 2014, in Beuther H., Klessen R. S., Dullemond C. P., Henning T., eds, Protostars and Planets VI. pp 125–148 (arXiv:1402.6196), doi:10.2458/azu_uapress_9780816531240-ch006

Monaci M., Magnani L., Shore S. N., Olofsson H., Joy M. R., 2023, A&A, 676, A138

Motte F., Bontemps S., Louvet F., 2018, ARA&A, 56, 41

Mróz P., et al., 2019, ApJ, 870, L10

Murray N., 2011, ApJ, 729, 133

Nahar S. N., 2000, ApJS, 126, 537

Nakanishi H., Sofue Y., 2003, PASJ, 55, 191

Nakanishi H., Sofue Y., 2006, PASJ, 58, 847

Navarro J. F., Frenk C. S., White S. D. M., 1995, MNRAS, 275, 720

Navarro J. F., et al., 2004, MNRAS, 349, 1039

Neelamkodan N., Tokuda K., Barman S., Kondo H., Sano H., Onishi T., 2021, ApJ, 908, L43

Nelson R. P., Langer W. D., 1999, ApJ, 524, 923

Neumann J., et al., 2020, A&A, 637, A56

Nitschai M. S., Eilers A.-C., Neumayer N., Cappellari M., Rix H.-W., 2021, ApJ, 916, 112

Oh C. S., Kobayashi H., Honma M., Hirota T., Sato K., Ueno Y., 2010, PASJ, 62, 101

Oka T., Hasegawa T., Sato F., Tsuboi M., Miyazaki A., Sugimoto M., 2001, ApJ, 562, 348

Oort J. H., 1954, Bull. Astron. Inst. Netherlands, 12, 177

Oort J. H., Kerr F. J., Westerhout G., 1958, MNRAS, 118, 379

Osterbrock D. E., 1989, Astrophysics of gaseous nebulae and active galactic nuclei. University Science Books

Ostriker J. P., Peebles P. J. E., 1973, ApJ, 186, 467

Ostriker J. P., Peebles P. J. E., Yahil A., 1974, ApJ, 193, L1

Padoan P., Pan L., Haugbølle T., Nordlund Å., 2016, ApJ, 822, 11

Pais M., Pfrommer C., Ehlert K., Pakmor R., 2018, MNRAS, 478, 5278

Pakmor R., Springel V., 2013, MNRAS, 432, 176

Pakmor R., Bauer A., Springel V., 2011, MNRAS, 418, 1392

Pakmor R., Kromer M., Taubenberger S., Springel V., 2013, ApJ, 770, L8

Palla F., Stahler S. W., 1999, ApJ, 525, 772

Pequignot D., Aldrovandi S. M. V., 1986, A&A, 161, 169

Persic M., Salucci P., Stel F., 1996, MNRAS, 281, 27

Petuchowski S. J., Dwek E., Allen J. E. J., Nuth J. A. I., 1989, ApJ, 342, 406

Pillepich A., et al., 2018, MNRAS, 473, 4077

Plummer H. C., 1911, MNRAS, 71, 460

Pohl M., Englmaier P., Bissantz N., 2008, ApJ, 677, 283

Polyachenko E. V., Shukhman I. G., 2015, MNRAS, 451, 601

Polyachenko E. V., Shukhman I. G., 2020, MNRAS, 498, 3368

Portail M., Gerhard O., Wegg C., Ness M., 2017, MNRAS, 465, 1621

Powell K. G., Roe P. L., Linde T. J., Gombosi T. I., De Zeeuw D. L., 1999, J. Comp. Phys., 154, 284

Prasad S. S., Huntress W. T. J., 1980, ApJS, 43, 1

Prole L. R., Clark P. C., Klessen R. S., Glover S. C. O., 2022, MNRAS, 510, 4019

Rahner D., Pellegrini E. W., Glover S. C. O., Klessen R. S., 2017, MNRAS, 470, 4453

Rahner D., Pellegrini E. W., Glover S. C. O., Klessen R. S., 2019, MNRAS, 483, 2547

Ramón-Fox F. G., Bonnell I. A., 2018, MNRAS, 474, 2028

Reid M. J., 2022, AJ, 164, 133

Reid M. J., et al., 2014, ApJ, 783, 130

Reid M. J., Dame T. M., Menten K. M., Brunthaler A., 2016, ApJ, 823, 77

Reid M. J., et al., 2019, ApJ, 885, 131

Roberts M. S., Whitehurst R. N., 1975, ApJ, 201, 327

Roman-Duval J., Jackson J. M., Heyer M., Rathborne J., Simon R., 2010, ApJ, 723, 492

Rosas-Guevara Y., et al., 2020, MNRAS, 491, 2547

Rubin V. C., Ford W. K. J., Thonnard N., 1980, ApJ, 238, 471

Sakai S., et al., 2000, ApJ, 529, 698

Sanders J. L., Smith L., Evans N. W., 2019, MNRAS, 488, 4552

Schneider N., et al., 2011, A&A, 529, A1

Schneider N., et al., 2013, ApJ, 766, L17

Schulz N. S., 2012, The Formation and Early Evolution of Stars, doi:10.1007/978-3-642-23926-7.

Scoville N. Z., Sanders D. B., Clemens D. P., 1986, ApJ, 310, L77

Sellwood J. A., 2011, MNRAS, 410, 1637

Sellwood J. A., Evans N. W., 2001, ApJ, 546, 176

Sembach K. R., Howk J. C., Ryans R. S. I., Keenan F. P., 2000, ApJ, 528, 310

Sérsic J. L., 1963, Boletin de la Asociacion Argentina de Astronomia La Plata Argentina, 6, 41

Shapiro P. R., Kang H., 1987, ApJ, 318, 32

Shore S. N., 1981, ApJ, 249, 93

Skarbinski M. S., Jeffreson S. M. R., Goodman A. A., 2022, arXiv e-prints, p. arXiv:2212.01396

Smith R. J., Glover S. C. O., Clark P. C., Klessen R. S., Springel V., 2014, MNRAS, 441, 1628

Smith B. D., et al., 2017, MNRAS, 466, 2217

Sofue Y., 2011, PASJ, 63, 813

Sofue Y., Honma M., Omodaka T., 2009, PASJ, 61, 227

Soler J. D., Hennebelle P., 2017, A&A, 607, A2

Soler J. D., et al., 2022, A&A, 662, A96

Sormani M. C., Binney J., Magorrian J., 2015a, MNRAS, 449, 2421

Sormani M. C., Binney J., Magorrian J., 2015b, MNRAS, 454, 1818

Sormani M. C., et al., 2019, MNRAS, 488, 4663

Sormani M. C., Magorrian J., Nogueras-Lara F., Neumayer N., Schönrich R., Klessen R. S., Mastrobuono-Battisti A., 2020, MNRAS, 499, 7

Sormani M. C., et al., 2022a, MNRAS, 512, 1857

Sormani M. C., Gerhard O., Portail M., Vasiliev E., Clarke J., 2022b, MNRAS, 514, L1

Sormani M. C., Sobacchi E., Sanders J. L., 2023, arXiv e-prints, p. arXiv:2309.14093

Springel V., 2005a, MNRAS, 364, 1105

Springel V., 2005b, MNRAS, 364, 1105

Springel V., 2010a, MNRAS, 401, 791

Springel V., 2010b, MNRAS, 401, 791

Springel V., et al., 2018, MNRAS, 475, 676

Springel V., Pakmor R., Zier O., Reinecke M., 2021, MNRAS, 506, 2871

Stancil P. C., Lepp S., Dalgarno A., 1998, ApJ, 509, 1

Stancil P. C., Schultz D. R., Kimura M., Gu J. P., Hirsch G., Buenker R. J., 1999, A&AS, 140, 225

Stecher T. P., Williams D. A., 1967, ApJ, 149, L29

Stone J. M., Tomida K., White C. J., Felker K. G., 2020, ApJS, 249, 4

Stutzki J., Bensch F., Heithausen A., Ossenkopf V., Zielinsky M., 1998, A&A, 336, 697

Szebehely V., 1967, Theory of orbits. The restricted problem of three bodies

Takahira K., Tasker E. J., Habe A., 2014, ApJ, 792, 63

Tan J. C., Beltrán M. T., Caselli P., Fontani F., Fuente A., Krumholz M. R., McKee C. F., Stolte A., 2014, in Beuther H., Klessen R. S., Dullemond C. P., Henning T., eds, Protostars and Planets VI. p. 149 (arXiv:1402.0919), doi:10.2458/azu_uapress_9780816531240-ch007

Tanvir T. S., Dale J. E., 2020, MNRAS, 494, 246

Tasker E. J., Tan J. C., 2009, ApJ, 700, 358

Teyssier R., 2002, A&A, 385, 337

Tielens A. G. G. M., 2005, The Physics and Chemistry of the Interstellar Medium. Cambridge University Press

Tielens A. G. G. M., Hollenbach D., 1985, ApJ, 291, 722

Tokuda K., et al., 2019, ApJ, 886, 15

Toomre A., 1981, in Fall S. M., Lynden-Bell D., eds, Structure and Evolution of Normal Galaxies. pp 111–136

Toomre A., 1990, in Wielen R., ed., , Dynamics and Interactions of Galaxies. pp 292–303

Tress R. G., Smith R. J., Sormani M. C., Glover S. C. O., Klessen R. S., Mac Low M.-M., Clark P. C., 2020a, MNRAS, 492, 2973

Tress R. G., Sormani M. C., Glover S. C. O., Klessen R. S., Battersby C. D., Clark P. C., Hatchfield H. P., Smith R. J., 2020b, MNRAS, 499, 4455

Tress R. G., Sormani M. C., Smith R. J., Glover S. C. O., Klessen R. S., Mac Low M.-M., Clark P., Duarte-Cabral A., 2021, MNRAS, 505, 5438

Trevisan C. S., Tennyson J., 2002, Plasma Physics and Controlled Fusion, 44, 1263

Tsang W., Hampson R. F., 1986, Journal of Physical and Chemical Reference Data, 15, 1087

Tucker K. D., Kutner M. L., Thaddeus P., 1973, ApJ, 186, L13

Tully R. B., Fisher J. R., 1977, A&A, 54, 661

Valtonen M., Karttunen H., 2006, The Three-Body Problem

Vasiliev E., 2018, arXiv e-prints, p. arXiv:1802.08255

Vasiliev E., 2019, MNRAS, 482, 1525

Vasiliev E., Belokurov V., Erkal D., 2021, MNRAS, 501, 2279

Vázquez-Semadeni E., Palau A., Ballesteros-Paredes J., Gómez G. C., Zamora-Avilés M., 2019, MNRAS, 490, 3061

Vissapragada S., Buzard C. F., Miller K. A., O'Connor A. P., de Ruette N., Urbain X., Savin D. W., 2016, ApJ, 832, 31

Vogelsberger M., et al., 2014, MNRAS, 444, 1518

Voronov G. S., 1997, Atomic Data and Nuclear Data Tables, 65, 1

Wada K., Meurer G., Norman C. A., 2002, ApJ, 577, 197

Wadsley J. W., Stadel J., Quinn T., 2004, New Astron., 9, 137

Wadsley J. W., Keller B. W., Quinn T. R., 2017, MNRAS, 471, 2357

Wakelam V., et al., 2010, Space Sci. Rev., 156, 13

Walter F., Brinks E., de Blok W. J. G., Bigiel F., Kennicutt Robert C. J., Thornley M. D., Leroy A., 2008, AJ, 136, 2563

Wang J., Hammer F., Yang Y., 2022, MNRAS, 510, 2242

Wareing C. J., Pittard J. M., Falle S. A. E. G., 2017, MNRAS, 470, 2283

Wegg C., Gerhard O., 2013, MNRAS, 435, 1874

Wegg C., Gerhard O., Portail M., 2015, MNRAS, 450, 4050

Weinberger R., Springel V., Pakmor R., 2020, ApJS, 248, 32

Weingartner J. C., Draine B. T., 2001, ApJ, 563, 842

Wenger T. V., Balser D. S., Anderson L. D., Bania T. M., 2018, ApJ, 856, 52

Whitworth D. J., Smith R. J., Klessen R. S., Mac Low M.-M., Glover S. C. O., Tress R., Pakmor R., Soler J. D., 2023, MNRAS, 520, 89

Widmark A., Laporte C. F. P., Monari G., 2022, A&A, 663, A15

Williams T. G., et al., 2021, AJ, 161, 185

Wolfire M. G., McKee C. F., Hollenbach D., Tielens A. G. G. M., 2003, ApJ, 587, 278

Wolfire M. G., Tielens A. G. G. M., Hollenbach D., Kaufman M. J., 2008, ApJ, 680, 384

Wolfire M. G., Hollenbach D., McKee C. F., 2010, ApJ, 716, 1191

Wollenberg K. M. J., Glover S. C. O., Clark P. C., Klessen R. S., 2020, MNRAS, 494, 1871

Wu B., Van Loo S., Tan J. C., Bruderer S., 2015, ApJ, 811, 56

Wu B., Tan J. C., Christie D., Nakamura F., Van Loo S., Collins D., 2017, ApJ, 841, 88

Zabel N., et al., 2020, MNRAS, 496, 2155

Zanchet A., Bussery-Honvault B., Jorfi M., Honvault P., 2009, Physical Chemistry Chemical Physics (Incorporating Faraday Transactions), 11, 6182

Zucker C., et al., 2021, ApJ, 919, 35

de Blok W. J. G., Walter F., Brinks E., Trachternach C., Oh S. H., Kennicutt R. C. J., 2008, AJ, 136, 2648

de Vaucouleurs G., 1948, Annales d'Astrophysique, 11, 247

de Vaucouleurs G., 1959, Handbuch der Physik, 53, 275

van Dishoeck E. F., 1988, in Millar T. J., Williams D. A., eds, , Vol. 146, Rate Coefficients in Astrochemistry. Kluwer, p. 49, doi:10.1007/978-94-009-3007-0_4

van Dishoeck E. F., Black J. H., 1988, ApJ, 334, 771

van de Hulst H. C., Muller C. A., Oort J. H., 1954, Bull. Astron. Inst. Netherlands, 12, 117

Acknowledgements

First I would like to extend my greatest thanks and gratitude to my supervisors Simon Glover, Ralf Klessen and Mattia Sormani (unofficially). Their continued insight, guidance and patience has allowed me to explore my love for astronomy further and allow me to bloom into the scientist I am. It has been an honour to work within the group these almost 4 years. I would also like to extend my thanks to the collaborators within the ECOGAL collaboration for providing input towards the large scale ISM. Additionally, I would personally like to thank Eugene Vasiliev for providing the technical support for Agama and implementing changes and ideas we had.

These last almost 4 years would have been impossible if it was not for my amazing friends, colleagues and family: to Liz and Tom for keeping me company when I first arrived in Heidelberg and being long term drinking buddies. To Eric, Evert and the members of my IMPRS generation for lifelong memories and enjoyment even during the height of lockdown. To my office mates Junia, Loke and Jia Weh for making the working atmosphere a joyous one full of random noises and dances, even if it meant Loke falling to the floor on a couple of occasions. To David, Joe and Noé for providing moral support during my lowest times and reassuring me that achieving my PhD is possible. To my roommates old and new for withstanding my scientific rants for hours at a time. I want to give special thanks my current boyfriend, Sebastian, who has been my source of comfort towards the end of my PhD.

Lastly I want to thank my mother Leanne and my auntie Cher. You have provided me with so much during my life that thanks alone is not simply enough. Whether it is the place to stay whenever I visit, the late night phone calls when life got tough, or even the random messages detailing something funny has happened, you have been true pillars of support for me. Thank you.

I am grateful for the financial support provided by the Deutsche Forschungsgemeinschaft (DFG, German Research Foundation) – Project-ID 138713538 – SFB 881 ("The Milky Way System", subproject B08), by the European Research Council in the ERC Synergy Grant 'ECOGAL – Understanding our Galactic ecosystem: From the disc of the Milky Way to the formation sites of stars and planets' (project ID 855130),

and from the bridge funding provided by HGSFP to allow for the completion of this thesis. This thesis makes use of computing resources provided by the State of Baden-Württemberg through bwHPC and DFG through grant INST 35/1134-1 FUGG, and from the data storage facility Scientific Data Storage Heidelberg (SDS@hd) supported through grant INST 35/1314-1 FUGG. Additionally this thesis benefited from the scientific support and HPC resources provided by the Erlangen National High Performance Computing Center (NHR@FAU) of the Friedrich-Alexander-Universität ErlangenNürnberg (FAU) under the NHR project a104bc. NHR funding is provided by federal and Bavarian state authorities. NHR@FAU hardware is partially funded by the German Research Foundation (DFG) – 440719683. I also thank for computing time provided by the Leibniz Computing Centre (LRZ) for project pr74nu.